

Thermodynamics in Trapped Ion Quantum Processors

Dissertation

Zur Erlangung des akademischen Grades

Doktor der Naturwissenschaften

am Fachbereich Physik, Mathematik und Informatik

der Johannes Gutenberg-Universität in Mainz

vorgelegt von

Daniël Riemer Maria Pijn

geboren in Amsterdam



Mainz, July 2022

Betreuende Personen: Prof. Dr. Ferdinand Schmidt-Kaler
Prof. Dr. Peter van Loock

Datum der mündlichen Prüfung: 28. November 2022

Abstract

As noisy intermediate-scale quantum (NISQ) processors are becoming more widely available, techniques are being developed for scalable benchmarking of such systems. Thermodynamics-based methods form a very suitable complementary toolset as they naturally scale for larger numbers of particles. The established concept of passivity has thus far not been used to set bounds on the evolution of microscopic systems initialized in thermal states. In this work, I employ two passivity-related frameworks to sense the coupling to an otherwise undetected environment, which is coined a heat leak. For the application of both frameworks, global passivity and passivity deformation, two system qubits are undergoing unitary evolution. The optional coupling to a third environmental qubit is detected as non-unitary evolution of the system qubits.

Important for the experimental realization of these thermodynamic algorithms is fast initialization of qubits in thermal (incoherent) states, which I added to the toolbox of the trapped ion platform. The employed quantum processor is based in a segmented linear ion trap, making use of high-fidelity laser-driven operations, and featuring $<100\text{ }\mu\text{s}$ preparation times for multi-qubit coherent and incoherent states. As part of this work, I characterized and optimized the main entanglement-seeding operation - the light-shift gate - for robustness, resulting in a 12-hour average cycle benchmarking success rate of $99.48(5)\%$, enabling high-fidelity long-term measurements. Of high importance for such improvement is the addition of an active magnetic field stabilization, achieving fluctuations below 100 nT , and allowing for phase-stable measurements longer than 15 ms.

Taking advantage of the improved operation of the trapped ion quantum processor, I have realized both passivity-based algorithms. It is shown that global passivity can verify the presence of a heat leak where a test using a microscopic version of the Clausius equation fails. Passivity deformation allows for even more sensitive detection of heat leaks, and identifies a heat leak with an error margin of 5.3 standard deviations, in a scenario where both the detection based on the Clausius equation and that based on global passivity fail. My work paves the way for experimental use of passivity-based methods to characterize quantum computers in the NISQ era.

Zusammenfassung

Quantencomputer (QC) im noisy intermediate scale (NISQ) werden zunehmend verfügbar und ein geeignetes Benchmarking dieser Systeme ist dringend erforderlich. Ich untersuche Verfahren, die auf thermodynamischen Grundbegriffen basieren und damit vorteilhaft auch für eine hohe Anzahl von qubits skalieren. Dazu wurde das theoretisch bereits etablierte Konzept der Passivität verwendet, um die Quantendynamik mikroskopischer thermischer Systeme einzuschränken. Als Wärmeleck wird jede Kopplung an die unbeobachtete Umgebung bezeichnet. Ich teste zwei Test-Algorithmen, einerseits auf globaler Passivität und andererseits auf Passivitätsdeformation beruhend: Die System-Qubits im QC durchlaufen eine unitäre Entwicklung. Die optionale Kopplung an ein Umgebungs-Qubit wird als nicht-unitäre Entwicklung der System-Qubits zweifelsfrei erkannt.

Der verwendete QC basiert auf konfigurierbaren Ionenkristallen in einer segmentierten Falle, lasergesteuerten Gitter Operationen hoher Fideltät und $<100 \mu\text{s}$ Initialisierungszeiten. Wichtig für die experimentelle Realisierung thermodynamischer Algorithmen ist eine Qubit Initialisierung in thermischen Zuständen, die ich dem Werkzeugkoffer der Ionen-NISQ Plattform hinzugefügt habe. Des Weiteren habe ich das zwei-Qubit Gitter charakterisiert, auf Robustheit optimiert und eine durchschnittliche 12-Stunden Cycle-Benchmarking Erfolgsrate von 99.48(5)% gemessen. Damit sind stabile Langzeitmessungen möglich. Von großer Bedeutung für diese Verbesserung ist die aktive Magnetfeldstabilisierung, welche externe Feldschwankungen auf $<100 \text{ nT}$ reduziert und damit phasenstabile Messsequenzen mit $>15 \text{ ms}$ ermöglicht.

Mit dem so verbesserten Ionen QC habe ich beide passivitäts-basierten Algorithmen realisiert. Es konnte gezeigt werden, dass globale Passivität das Vorhandensein eines Wärmelecks nachweisen kann, selbst wenn ein Test mit einer mikroskopischen Version der Clausius-Gleichung fehlschlägt. Der auf Passivitätsdeformation basierende Test ermöglicht eine Erkennung von Wärmelecks mit einer Konfidenz von 5.3 Standardabweichungen, in einem Szenario in dem sowohl die Erkennung auf der Grundlage der Clausius-Gleichung als auch der globale Passivitätstest fehlschlägt. Meine Arbeit ebnnet den Weg für den experimentellen Einsatz von passivitätsbasierten Methoden zur Charakterisierung von QC der NISQ-Ära.

Contents

1	Interplay between Physics and Computation	1
2	Elements of a Trapped Ion Quantum Computer	7
2.1	Coherent and incoherent laser-driven operations	7
2.2	Multi-qubit entanglement generation - theory and experiment	20
2.3	Tomography and benchmarking - theory and experiment	31
3	Experimental Setup	39
3.1	Multi-layered segmented linear Paul trap	39
3.2	Vacuum chamber and passively shielded quantizing magnetic field	46
3.3	Active magnetic field stabilization	51
3.4	Laser light sources for ion loading and qubit operations	56
3.5	Experimental control infrastructure	60
4	Theory of Passivity-Based Inequalities	65
4.1	Evolution of a composite system in a thermal state	66
4.2	Global passivity	67
4.3	Passivity deformation	71
5	Experimental Realization of Global Passivity	73
5.1	Framework application to a collection of three qubits	73
5.2	Quantum circuit formulation and implementation	74
5.3	Thermalization and customized entangling gate calibration	77
5.4	Readout and evaluation	82
6	Implementation of Passivity Deformation	85
6.1	Framework application	85
6.2	Quantum circuit formulation and implementation	86
6.3	SWAP gate calibration	88
6.4	Measurement and evaluation	89
7	Outlook - Periodicity Algorithms and a Quantum Heat Engine	91

Contents

A Raman laser intensity stabilization and beam distribution	97
A.1 Intensity stabilization	97
A.2 Beam distribution	99
B 729 high finesse locking setup	103
Bibliography	105
List of Publications	115

Chapter 1

Interplay between Physics and Computation

From quantum physics to quantum technologies

The first quantum revolution [Gri13] nearly a century ago, brought about tremendous understanding of the microscopic world, and with that, a technological revolution [Kra99]. The laws of physics were understood to such a degree that it allowed us to manipulate matter and light at the quantum mechanical level. This brought us many inventions, and opened up fields such as semiconductor and laser technology [Kra99, Sch16a]. However, while these devices rely on the effects of quantum mechanics, they do not make use of the extra properties that quantum mechanics has to offer, namely entanglement, superposition, and interference [SK00].

In the second half of the 20th century, pioneers started thinking about how to use these properties to gain an edge over conventional devices. Already in 1960, Feynman realized that we could theoretically store an infinite amount of information in a finite space by using the Hilbert space of quantum states [Fey60]. Several years later, Manin and Feynman argued that a quantum mechanical computer was necessary to efficiently simulate quantum physics [Man80, Fey82, Fey86, Man99], again due to the exponentially scaling Hilbert space. David Deutsch proposed that there is a whole class of problems that can only be efficiently computed on a universal quantum computer [Deu85, Deu89], and he gave one example algorithm that determines if a function is balanced [Deu92]. In 1994, Peter Shor developed the first groundbreaking algorithm [Sho94, Sho00]. His algorithm could efficiently factorize prime numbers, thereby breaking widely used public key cryptography systems. Two years later, Lov Grover presented an unordered search algorithm with a quadratic speedup compared to the best known algorithms for classical computers [Gro96]. In the meantime, Artur Ekert was one of the first to suggest how to actually build such a machine [Eke94].

This was readily picked up by Cirac and Zoller, who proposed the first concrete implementation in a system of trapped ions [Cir95].

The potential of quantum information had been shown, and technology had matured to the point where we could manipulate and analyze individual quantum systems. This gave rise to the fields of quantum computation, simulation, communication, sensing, and metrology, together known as quantum technologies [Sch16a, Ací18]. The continuing development of these fields is known as the second quantum revolution [Dow03, Jae18, Rov21].

From the proposed algorithms, Shor’s factorization and Grover’s search algorithm initially seemed to be the most revolutionary. While a relevant application of these algorithms is still far out of reach with currently available quantum computers [Eke96, Sko21], more recently proposed techniques like quantum annealing [VA18] and variational quantum eigensolving [Til] are already converging towards useful real-world applications [Mon16, Che20, Gil22].

Quantum computation can be considered the most challenging quantum technology. Initially, the community was split, if it would be possible at all [Har96]. Even now, despite the tremendous technological progress throughout the last decades, building and operating a useful quantum computer remains a formidable challenge [Gil22]. In the case of digital¹ quantum computation, either the evolution of a Hamiltonian or an algorithm of interest is discretized into N steps. Each step is modeled by a sequence of quantum gates, operating on a number of qubits. In-between these steps, the qubits can be probed, and corrected for errors due to noise or imperfect gates [Nie10]. A quantum computer is required to have a native set of operations that together form a universal quantum gate set, such that any algorithm can be translated into a set of these operations [DiV00]. A sequence of gates on a number of qubits is depicted by a quantum circuit, of which an example for parity readout is shown in Figure 1.1. For the purpose of this introduction, it shows how the simple operation of a four qubit parity readout involves many gates and two extra ‘ancilla’ qubits. Each gate comes with a certain probability for error. This circuit is a subroutine of a larger framework [Nig14] where redundancy, a concept from classical information processing, is used to protect the encoded information. However, that only works if the error rate per gate stays below the level where it can be efficiently corrected [Sho95, Ste96, Rau07, Aha08, Nig14].

¹ Quantum computation can also be analog (non-gate-based), for example in the case of quantum annealing.

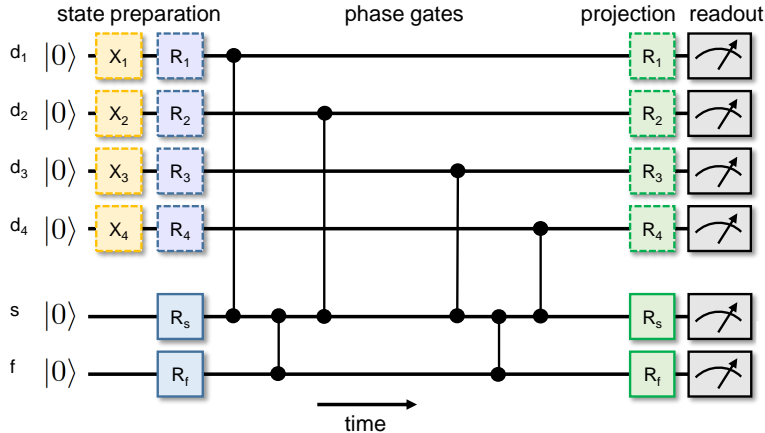


Figure 1.1: Quantum circuit for fault-tolerant parity readout of four data qubits. The data qubits (d_i) are initialized in $|0\rangle$. Single qubit gates prepare a certain state, after which two-qubit phase gates couple the data qubits to the syndrome (s) and flag (f) ancilla qubits. The ancilla qubits are there to readout the parity of the data qubits. In this example, each qubit is then projected to a certain basis by a single qubit gate, and measured. This scheme for parity readout is robust under a single bit or phase flip error [Hil22b].

Another main feature of quantum computation, which makes it simultaneously useful and very challenging, is the large Hilbert space that is spanned by the number of possible states. For a system of N qubits, the number of basis states scales as 2^N . The system can be in any superposition of these states, resulting in a 2^N -dimensional Hilbert space.

$$|\psi\rangle = \alpha_0 \underbrace{|000\dots000\rangle}_N + \alpha_1 |000\dots001\rangle + \dots + \alpha_{2^N-1} |111\dots111\rangle \quad (1.1)$$

with $\alpha_i \in \mathbb{C}$, and $\sum_{i=0}^{2^N-1} |\alpha_i|^2 = 1$. While algorithms make clever use of this Hilbert space, the exponential scaling of the number of coefficients α_i quickly makes simulation on a classical computer infeasible [Fey82]. Therefore, computational results cannot easily be verified. To ensure proper operation, and to identify sources of errors, the performance of quantum gates should be benchmarked. Using existing methods will present a challenge as the number of qubits is scaled up [Res, Gre]. This thesis explores current and potential future methods for benchmarking quantum gates.

Developments that led to this thesis

My goal was to characterize and improve the fidelity and robustness of two-qubit entangling gates (Section 2.2). In parallel, I investigated the use of randomized benchmarking for calibration and characterization (Section 2.3). These techniques are very suitable for current state of the art quantum computers, but do not scale very well for large numbers of qubits, due to the size of the Hilbert space that is involved in the required measurements. Even for less than 10 qubits, it becomes fully impossible to realize. However, for the new generation of quantum computers, we are aiming for 50-100 qubits.

Thus, we are thrilled to apply thermodynamic concepts to quantum computing, to complement the existing set of benchmarking methods. The strategy of thermodynamics is to characterize the system and its dynamics from macroscopic variables. Conceptually, this means that we do not have to keep track of every molecule to understand the temperature or a physical transition. How far can this concept be carried over to quantum engines, which are represented here by quantum computers with trapped ions? That is to be discussed in the following.

Thermodynamics and quantum computers

Thermodynamics was conceived in the mid-17th century as a practical theory for describing heat flows and efficiencies of heat engines. More recently, the aim has been to adapt and extend classical thermodynamics to describe microscopic systems, predominantly theoretically [Gev96, All04, Spe07, Cam11, Kos14, Gou15, Bin18, Uzd18a, Los19, Lan21], but also experimentally [Roß16, Cot17, Kla19, Lin19, Mas19, Buf20, van20, Sol21]. In particular, the second law and one of its mathematical equivalents, the Clausius inequality [Cla65, Uzd18a, Str21], have been extended to apply to a system and environment which are initially correlated. The frameworks of global passivity and passivity deformation have been developed to set tight bounds on the unitary evolution of a system that is initially in a thermal state [Uzd18b, Uzd21].

In the context of this work, these frameworks were used to derive inequalities that govern the unitary evolution of a set of qubits. Any error sources that violate the unitarity of a quantum circuit (e.g. photon scattering), can show up as so-called ‘heat leaks’, by violating these inequalities. In the setting of a quantum circuit, one may describe this mechanism as a coupling to additional qubit(s), which do not have to be observed (see Fig. 1.2). This way, we can detect certain error sources, independent

of the algorithm used, and by only measuring the qubits that are part of the unitary evolution. For larger numbers of qubits, the number of measurements required for this method scales much more favorably than for example quantum process tomography [Moh08] or quantum state tomography [Vog89, ROO04, Lvo09]. Also, this method is insensitive to coherent errors that arise due to miscalibration of gate operations. Therefore, the detection of heat leaks may serve to complement the commonly used tomography methods.

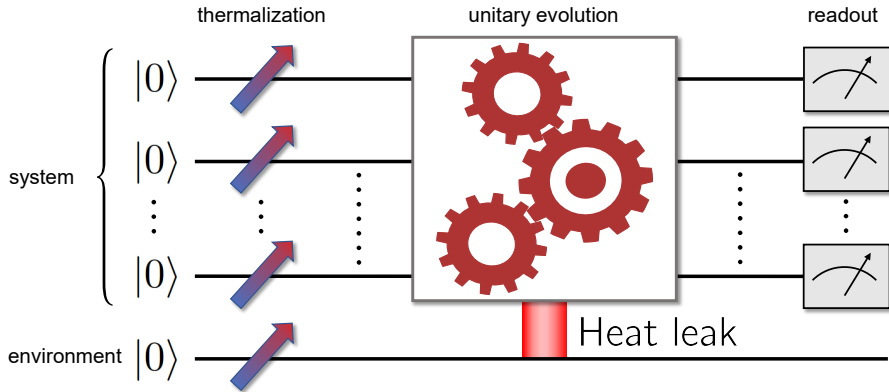


Figure 1.2: A number of system qubits and one environment qubit are initialized to thermal states. The system qubits undergo a unitary “black box” evolution and are measured. In the case of a heat leak, the system is coupled to an undetected environment qubit. This can show up as a violation of the second law of thermodynamics, or as a violation of one of the passivity inequalities derived in Chapter 4.

Compass

The elements that make up our quantum computer are explained in Chapter 2. Special emphasis is laid on the ability for fast preparation of incoherent (thermal) states. Sections 2.2 & 2.3 discuss the mechanism, robustness, and characterization of two-qubit entangling gates using randomized benchmarking. We will use these two-qubit gates later on to couple the system and environment. Chapter 3 discusses the experimental setup used for this work, with an emphasis on the recently added active magnetic field stabilization system necessary for robust gate operation. The theoretical framework for global passivity and passivity deformation, and the relation to the Clausius inequality is explained in Chapter 4. Then, I will apply these new concepts to a set of two system qubits and one environment qubit: Chapter 5 deals with specific calibrations and the demonstration of a heat leak within the global passivity framework. In Chapter 6, using another three qubit experiment, I will show how the passivity deformation framework is even more sensitive to heat leaks. The results of these last two chapters were also published in [Pij22]. Finally, in Chapter 7, I will discuss the generalization and further application of these thermodynamic concepts to quantum computers.

Chapter 2

Elements of a Trapped Ion Quantum Computer

In this chapter we discuss the elements needed to operate the $^{40}\text{Ca}^+$ spin qubit used for this work. In Section 2.1, starting with a motivation for laser-driven operations, we consider the relevant transitions for $^{40}\text{Ca}^+$. The confinement of ions in a segmented linear Paul trap, and the emergence of collective vibrational modes for a two-ion crystal are addressed, which are essential for creating entanglement. Initial state preparation after subsequent Doppler and pulsed resolved sideband cooling is discussed, with an emphasis on the ability to create and manipulate coherent and incoherent states alike. The shelving mechanism that allows for state-selective fluorescence readout is briefly addressed. In Section 2.2, the mechanism for creating entanglement is described, as well as the daily calibration procedure and the error-mitigating measures. Finally, in Section 2.3, the performance of the quantum processor used for this work is benchmarked using state tomography and randomized benchmarking. Cycle benchmarking, a variant of randomized benchmarking, is discussed as a tool for parameter optimization, and used to probe the long-term stability of entangling operations.

2.1 Coherent and incoherent laser-driven operations

Even though some transitions are in the radio frequency (rf) range, we use lasers for all interactions with electronic states of the $^{40}\text{Ca}^+$ ion (see Fig. 2.1). Advantages are precise addressing, due to optical wavelengths and easy manipulation of laser beams with optics, interaction speed, due to a high Lamb-Dicke parameter¹, switching

¹ The Lamb-Dicke parameter is defined as the ratio of the spread of the wavefunction to the radiation wavelength $\eta = k_z z_0$ [Lei03a]. A high Lamb-Dicke parameter implies high electric

speed by using acousto-optic modulators, and availability of highly developed and stable commercial diode laser systems for the entire relevant spectrum. An additional advantage of using optical control fields is their small wavelength, allowing to impart momentum to trapped ions. This allows for strong spin-motion coupling, which will be useful for the two-qubit entangling gates.

The $^{40}\text{Ca}^+$ spin qubit

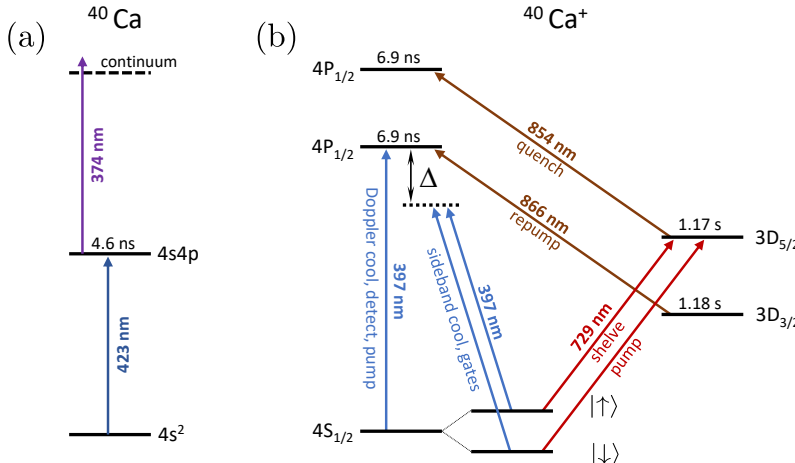


Figure 2.1: (a) Two-step ionization of ^{40}Ca . The 423 nm laser is wavemeter-stabilized to ~ 10 MHz, while the second step only needs to be below 390 nm. (b) Relevant energy levels in $^{40}\text{Ca}^+$. The qubit states are encoded in the spin of the $4S_{1/2}$ ground state. Doppler cooling and fluorescence detection is performed on the $4S_{1/2} \leftrightarrow 4P_{1/2}$ transition, and qubit operations are realized as stimulated Raman transitions via the $4P_{1/2}$ state. The $3D_{5/2}$ state is used for optical pumping, and for selective ‘electron shelving’ prior to detection (see text). The lifetime of each state before decay to the $4S_{1/2}$ ground state is indicated. In 6% of cases, the $4P_{1/2}$ state decays to the $3D_{3/2}$ state, and is pumped back by an 866 nm laser [Emm75, Jin93, Kre05, Het15].

Calcium ions are widely used because of their hydrogen-like electronic structure, where all relevant transitions are close to the visible spectrum. Commercial diode lasers and fiber optical elements are easily available, and resonance fluorescence can be detected with high efficiency.

field gradients, leading to fast light-shift gates [Bal14]. Obtaining high gradients with microwave radiation requires the ions to be < 50 μm from the antenna, which introduces other problems [War13].

Calcium enters the trap area as neutral atoms. We ionize the atoms in two steps, where a 423 nm laser drives the transition between the $4s^2$ and $4s4p$ state, and a 374 nm laser excites the outermost electron from the $4p$ state to the continuum. Since the first laser has to be resonant with the $4s^2 \leftrightarrow 4s4p$ transition, this technique is isotope-selective. For the second step, any laser with a wavelength below 390 nm is sufficient.

For Doppler cooling and fluorescence detection, we continuously drive the $4S_{1/2} \leftrightarrow 4P_{1/2}$ transition. The $4P_{1/2}$ state has a lifetime of 6.9 ns [Het15], after which there is a $\sim 94\%$ probability to decay back to the $4S_{1/2}$ state. A photon is emitted and detected on a photomultiplier tube. In the remaining 6% of cases, the ion falls back to the $3D_{3/2}$ state. This state has a lifetime of 1.18 s [Kre05], which removes the ion from the cooling/detection cycle for the remainder of the measurement. Therefore, an 866 nm laser is used during detection and Doppler cooling, to repump back to the $4P_{1/2}$ state.

The qubit states are encoded in the $4S_{1/2}$ ground state Zeeman sublevels

$$\begin{aligned} |0\rangle &\equiv |\uparrow\rangle \equiv |4S_{1/2}, m_J = +1/2\rangle \\ |1\rangle &\equiv |\downarrow\rangle \equiv |4S_{1/2}, m_J = -1/2\rangle \end{aligned} \quad (2.1)$$

The degeneracy of these levels is lifted by a magnetic field of ~ 0.37 mT, resulting in a frequency splitting of $\sim 2\pi \times 10.5$ MHz. This is very convenient since the splitting is large enough to separate qubit states and sidebands, but the 22 MHz natural linewidth of the $4S_{1/2} \leftrightarrow 4P_{1/2}$ transition is only slightly increased, such that Doppler cooling and detection are hardly affected. Another advantage of using the $4S_{1/2}$ ground state is that the qubit states have a virtually infinite T_1 lifetime. Therefore, very long coherence times, only depending on magnetic field noise and heating rates, can be achieved.

For transitions between the qubit states we employ two beams coming from a single 397 nm laser. The beams are detuned from the $4S_{1/2} \leftrightarrow 4P_{1/2}$ transition by $\Delta \approx -2\pi \times 1$ THz, and together drive stimulated Raman transitions [RAM28]. By changing the frequency of one of the two beams, we can drive carrier transitions, for single qubit gates, or sideband transitions, for sideband cooling and two-qubit gates.

Finally, we use a 729 nm laser to drive quadrupole transitions between the qubit states and the $3D_{5/2}$ manifold, for state initialization, and for mapping $|\uparrow\rangle$ to the $3D_{5/2}$ state before detection. This ‘electron shelving’ operation converts $|\uparrow\rangle / |\downarrow\rangle$ to dark/bright and thereby enables state selective readout. With a lifetime of 1.17 s [Kre05], the ion will stay in the $3D_{5/2}$ state, unless quenched to the $4P_{3/2}$ state by an 854 nm laser. From there the ion quickly decays to the ground state and returns to

the cooling/detection cycle.

For state initialization, the 729 nm laser can be combined with or replaced by a σ^+ polarized 397 nm laser, as will be explained in a later section.

Ion trapping and ion crystals

According to Earnshaw's theorem, there is no free-space point of stable equilibrium for a point charge in an electrostatic field [Wei76]. This is a direct consequence of the Laplace equation, or equivalently Gauss's law in free-space, which states that the divergence of any electric force field must be zero:

$$\Delta V = -\nabla \cdot \vec{E} = 0 \quad (2.2)$$

Therefore, ions can only be trapped using a combination of magnetic and electric fields, as in a *Penning trap* [Deh68], or by employing oscillating inhomogeneous electric fields, which is the underlying principle of the *radio frequency* or *Paul trap* [Pau53]. How an oscillating electric field gives rise to a confining *ponderomotive potential*, can be understood from the following picture: a charged particle in an oscillating electric field will experience a potential that is 180° out of phase with its motion, i.e. the particle is always closer to the electrode when the polarity is such that it acts repulsive. However, as the field magnitude is larger close to the electrode, a net repulsive force arises averaged over many oscillation periods. Similarly, in a two-dimensional oscillating quadrupole field, an effective rotating saddle potential is created, with a small persisting force towards the potential minimum. In a segmented linear Paul trap [Sch06], which is used for all experiments in this work, the *radial confinement* is provided by this mechanism. An oscillating quadrupole field is created between a pair of rf electrodes and a pair of dc electrodes at negative voltage, as illustrated in Fig. 2.2. The *axial confinement* along the trap axis is provided by individually controlled pairs of dc electrodes. Since the rf electrodes are interconnected, the axial confinement can be freely adjusted using the dc voltages, allowing for multiple configurable and scalable strings of ions. For a static potential, the adjacent dc electrodes are typically supplied with -6 V, and the surrounding dc electrodes are grounded. More technical and operational details are described in Chapter 3.

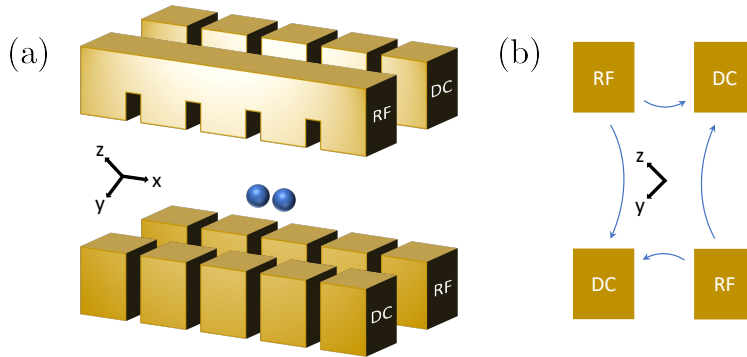


Figure 2.2: (a) Schematic of a segmented linear Paul trap. Radio frequency (RF) electrodes generate an oscillating quadrupole field in the y - z plane, which is combined with a static potential in the x direction generated by DC electrodes. The RF electrodes are interconnected to provide an x -axis symmetry. Ion crystals can be trapped between each pair of DC electrodes and shuttled along the x - or *trap axial direction* to obtain a scalable register of ion strings. (b) Intersection in the y - z or *radial* plane, with indicated rf quadrupole field lines. The effective potential gives rise to secular modes along the y - and z -direction, defined as *radial 1* and *radial 2*, respectively. Due to the interconnected (equipotential) RF electrodes in the x -direction, the rotational symmetry is broken. The dc-potential is confining in the y -direction and anti-confining in the z -direction. Together with a -6 V potential from the dc electrodes, this geometry leads to higher secular frequencies for radial 2 [Ber12a, p. 20].

To better understand the dynamics of ions and ion crystals, a more quantitative treatment is required. The main aspects are mentioned here, while the details can be found in [Lei03a]. The total potential for a single charged particle in a dc and rf electric field, in direction $q \in \{x, y, z\}$, is given by

$$\Phi(q, t) = \alpha_q^{(\text{rf})} q^2 U_{\text{rf}} \cos(\Omega_{\text{rf}} t) + \alpha_q^{(\text{dc})} q^2 U_{\text{dc}}, \quad (2.3)$$

with potential curvatures $\alpha_q^{(\text{rf})}$ and $\alpha_q^{(\text{dc})}$ in the corresponding directions, Ω_{rf} for the angular drive frequency, and $U_{\text{dc}, \text{rf}}$ for the corresponding dc and rf electrode voltages. By requiring that the dc and rf potentials individually satisfy the Laplace equation $\Delta V = 0$, we can derive the equations of motion, also known as Mathieu differential equations. For a particle with mass m and charge e , we find

$$\frac{d^2 q}{d\tau^2} + (a_q - 2b_q \cos(2\tau))q = 0 \quad (2.4)$$

with

$$\tau = \frac{\Omega_{\text{rf}} t}{2} \quad a_q = \frac{4|e|\alpha_q^{(\text{dc})} U_{\text{dc}}}{m\Omega_{\text{rf}}^2} \quad b_q = \frac{2|e|\alpha_q^{(\text{rf})} U_{\text{rf}}}{m\Omega_{\text{rf}}^2}. \quad (2.5)$$

For $a_q < b_q^2 \ll 1$, a stable solution for the particle position can be found:

$$q(t) \approx q_0 \cos\left(\frac{\gamma_q \Omega_{\text{rf}}}{2} t\right) \left(1 + \frac{b_q}{2} \cos(\Omega_{\text{rf}} t)\right), \quad (2.6)$$

with $\gamma_q = \sqrt{a_q + b_q^2}/2$. This solution expresses the earlier described fast oscillation at frequency Ω_{rf} , known as *micromotion*, and a slower oscillation due to the effective ponderomotive potential at frequencies

$$\omega_q = \frac{\gamma_q \Omega_{\text{rf}}}{2}, \quad (2.7)$$

known as *secular harmonic motion*.

When a number of ions are trapped in the same potential and sufficiently cooled, an ion string can be formed along the weakest trap axis, which is in this work the x -direction. The equilibrium positions and dynamics of the ions are determined by the balance between the trapping potential and the Coulomb interaction. The total

electrostatic energy for a set of N ions is given by

$$V = \frac{1}{2}m \sum_{n=1}^N (\omega_x^2 x_n^2 + \omega_y^2 y_n^2 + \omega_z^2 z_n^2) + \frac{e^2}{4\pi\epsilon_0} \sum_{n,m,n \neq m}^N \frac{1}{\sqrt{(\vec{r}_n - \vec{r}_m)^2}}, \quad (2.8)$$

with $\vec{r}_n = (x_n, y_n, z_n)^T$. The equilibrium positions of the ions can be determined by finding the minima of the potential energy

$$\left[\frac{\partial V}{\partial x_n} \right]_{x_n=x_n^{(0)}} = 0. \quad (2.9)$$

This equation can be solved analytically for $N \leq 3$ and numerically for larger ion numbers [Jam98]. By expanding Eq. 2.8 to second order in the equilibrium positions, a $3N \times 3N$ Hessian matrix is found. The dynamics of a linear string of N harmonically confined ions can be described by $3 \times N$ independent harmonic oscillators, known as *collective vibrational modes* or *normal modes*. The frequencies of these modes can be found from the eigenvalues of the Hessian matrix. For a two-ion crystal we can distinguish in-phase center of mass (com) modes, and out-of-phase stretch and rocking modes [Pos10]. Table 2.1 lists these modes along with typical experimental values.

Axis	Mode	Frequency	Typical value / 2π (MHz)
x	axial com	ω_x	1.49
x	axial stretch	$\sqrt{3}\omega_x$	2.58
y	radial 1 com	ω_y	3.81
y	radial 1 rocking	$\sqrt{\omega_y^2 - \omega_x^2}$	3.51
z	radial 2 com	ω_z	4.58
z	radial 2 rocking	$\sqrt{\omega_z^2 - \omega_x^2}$	4.33

Table 2.1: Collective vibrational modes for a two-ion crystal. The center of mass mode frequencies ω_x, y, z are given by Eq. 2.7, and the axes are defined in Fig. 2.2. The typical rf drive frequency is $\Omega_{rf} = 2\pi \times 33.48$ MHz. A detailed derivation of the frequencies can be found in [Pos10].

General initial state preparation

Doppler cooling

After ionization, the ions will crystallize in the center of the Paul trap if they are sufficiently cold. A 397 nm laser is aligned at a 45° angle to each of the trap axes, to provide Doppler cooling [Ste86] in each direction. The laser is significantly red detuned

from the $4S_{1/2} \leftrightarrow 4P_{1/2}$ transition by about $-2\pi \times 340$ MHz, and therefore only cools the hottest ions. When the ions are crystallized we switch to another, less intense 397 nm laser, detuned by about half the natural linewidth of the cooling transition. For a thorough analysis of Doppler cooling in $^{40}\text{Ca}^+$, see [Har13].

For continuously monitoring the ions between measurement sequences we use a 397 nm laser close to resonance, with an intensity that saturates the $4S_{1/2} \leftrightarrow 4P_{1/2}$ transition. When ions are lost or decrystallize, we switch back to the highly detuned laser for 2 ms of recrystallization, or start an automated retrapping sequence. Note that the 866 nm repump laser is tuned from blue detuning towards resonance. This is done to avoid any of the nearby dark resonances on the red side of the transition frequency, which create a direct coupling between the $4S_{1/2}$ and $3D_{3/2}$ states [Ari76, Har13]. Additionally, while using the high-intensity high-detuned recrystallization laser, a Stark shift-induced splitting of the $4P_{1/2}$ manifold should be taken into account.

Pulsed resolved sideband cooling

Before every experimental run, we perform 2 ms of low-intensity Doppler cooling, to start in a well-defined cold state. Then, if it is needed for the particular experiment, we perform resolved sideband cooling on the relevant motional modes. Resolved sidebands are existing either on the $4S_{1/2} \leftrightarrow 5D_{5/2}$ transition (729 nm) [Lei00, Pos10], or on stimulated Raman transitions via the $4S_{1/2} \leftrightarrow 4P_{1/2}$ transition (397 nm). Due to the shorter wavelength, the stimulated Raman transitions feature a higher momentum transfer, which is advantageous for cooling. Another advantage in our setup is that we can use the same laser beams as we do for single and two-qubit gates, and thereby we can target only specific motional modes at a time (see Chapter 3). We have the option to do either pulsed or continuous sideband cooling. The continuous version requires a very delicate balance of cooling and quenching beam intensities [Mar94], so we choose the more robust pulsed variant, where we perform a number of approximate π pulses on red sidebands² in several rounds [Rus17a]. Here we discuss our specific implementation, illustrated in Fig. 2.3, and we present one example sequence in Table 2.2.

For each round we start by pumping from the $|m_J = -1/2\rangle$ to the $|m_J = +1/2\rangle$

² Excitation of the *N*th *red sideband* at frequency $\omega = \omega_0 - N\omega_x$ relative to a carrier transition with frequency ω_0 decreases the occupation number of the motional mode with frequency ω_x by *N*. Similarly, excitation of the *blue sideband* at frequency $\omega = \omega_0 + N\omega_x$ increases the motional occupation number by *N*. This type of light-motion coupling only holds in the *resolved sideband regime* [Lei03a].

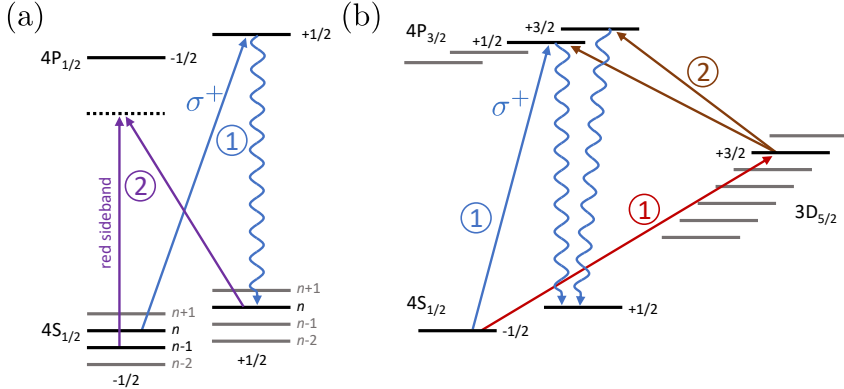


Figure 2.3: (a) One cycle of sideband cooling: Optical pumping to $m_J = +1/2$ using σ^+ polarized light (blue), followed by a Raman π pulse on a red sideband (purple). (b) One cycle of optical pumping to $m_J = +1/2$ via the $3D_{5/2}$ state, for state initialization. σ^+ pumping is faster, but less efficient and polarization dependent.

state using a σ^+ polarized 397 nm beam³. Within the excited state lifetime of 6.9 ns [Jin93], the ion can decay to either of the ground states, but by continuously pumping, the $|m_J = -1/2\rangle$ state is slowly depleted. We usually pump for 1 μ s per cooling round. Then we perform an approximate Raman π pulse on a red sideband of the motional mode that we want to cool. This removes one or two phonons, depending on which sideband we used, and leaves the ion in $|m_J = -1/2\rangle$, after which another round starts. With each round we adapt the pulse duration on the red sideband, to account for changes in the Rabi frequency on the respective mode, as the mean phonon number decreases. When we want to cool several motional modes, for example all radial modes, we perform several rounds on each mode, starting with the 2nd red sidebands of the rocking modes, then the 2nd red sidebands of the center of mass (com) modes, and then the respective 1st red sidebands. Here we need to find a balance between sufficient rounds on a particular mode for ground state cooling, and not leaving the other modes uncooled for too long (depending on the heating rates). Alternating between the 1st and 2nd red sidebands is done to prevent population trapping as the coupling strengths change as a function of the phonon number [Win79]. We experimentally optimized the order of modes, the number of rounds, and the pulse durations for several preset sequences, tailored to the specific application (e.g. cooling on all radial modes for a two-ion crystal, when we perform two-qubit gates). This kind of optimization lends itself very well to the use of optimization algorithms: Using the Nelder-Mead algorithm

³ σ^+ pumping is faster, but less efficient than 729 nm pumping.

[Nel65], we managed to reduce the total cooling time by roughly 37% [Con21]. For daily calibration, we use the constant relation between Rabi frequencies of different sidebands to define all pulse durations relatively, such that we only have to calibrate the Raman π pulse duration for one mode. An example sequence for cooling all radial modes on a two-ion crystal is shown in Table 2.2. It contains a total of 426 pulses and takes 4.7 ms. After cooling, we measured mean phonon numbers of 0.04, 0.05, 0.09, 0.1 on the radial 1 com, radial 2 com, radial 1 rocking, and radial 2 rocking modes, respectively, where 1 and 2 denote the two radial directions perpendicular to the trap axis (see Fig. 2.2).

Round	Red sideband	Cycles	Reference time multiplier	Time increment per cycle
1	2nd radial 2 rocking	2	3	0.002 676 45
2	2nd radial 1 rocking	2	0.367	0.000 32
3	2nd radial 2 com	4	0.3	0
4	2nd radial 1 com	4	0.74	5.5×10^{-5}
5	1st radial 2 rocking	64	0.55	0.016
6	1st radial 1 rocking	23	0.74	0.092
7	1st radial 2 com	55	0.892	0.014
8	1st radial 1 com	63	0.55	0.003
9	1st radial 2 rocking	63	0.55	0.0003
10	1st radial 1 rocking	59	0.74	3×10^{-9}
11	1st radial 2 com	62	0.74	0
12	1st radial 1 com	25	1	0

Table 2.2: Raman pulse sequence for cooling all radial modes of a two-ion crystal. Every round is preceded by 1 μ s of σ^+ pumping to the $|m_J = +1/2\rangle$ state. The multipliers are relative to a calibrated reference time of $\sim 10 \mu$ s. This sequence was used for the high-fidelity gate measurements in Section 2.2 & 2.3. The specific values were found using the Nelder-Mead algorithm (see text).

Qubit initialization

After either Doppler cooling or sideband cooling, we use a combination of 729 and circularly polarized 397 nm light to initialize the qubit state to $|0\rangle \equiv |\uparrow\rangle \equiv |m_J = +1/2\rangle$. Beginning with σ^+ polarized 397 nm light, we pump for 1 μ s to deplete the $|m_J = -1/2\rangle$ state, as in each round of sideband cooling. Additionally, we drive a $|4S_{1/2}, m_J = -1/2\rangle \leftrightarrow |3D_{5/2}, m_J = +3/2\rangle$ π pulse of about 10 μ s coupled with a 4 μ s 854 nm quenching pulse. After a lifetime of 6.9 ns [Jin93], the ion can now only decay to $|m_J = +1/2\rangle$. We repeat this 729/854 cycle 4 times. While the sigma pumping is

faster, the efficiency is technically limited by the purity of σ^+ polarization. Using both techniques together, we reach an efficiency of >99% for pumping into $|0\rangle$.

If initialization to the opposite state is required, we omit the σ^+ pumping, and use the $|4S_{1/2}, m_J = +1/2\rangle \leftrightarrow |3D_{5/2}, m_J = -3/2\rangle$ transition instead. Without the sigma pumping, we need more cycles of 729/854 pumping to reach the same efficiency, for a total of 10 cycles.

For preparing any mixed state, we first initialize to $|\downarrow\rangle$, and then vary the pulse duration of a σ^+ polarized 397 nm pulse until we reach the desired populations. This is an incoherent process due to the spontaneous emission from the $4P_{1/2}$ to the $4S_{1/2}$ state. The precision of the mixed state preparation is then only limited by the initial preparation of $|\downarrow\rangle$, and the pulse time, intensity, and polarization stability of the σ^+ beam. Typical mixed state preparation times using this technique are in the order of 140 μ s, and we can even shorten that to \sim 60 μ s if we initially pump to $|\uparrow\rangle$ and use a Raman π pulse before the σ^+ pumping. This relatively simple and fast mixed state preparation is a major advantage of the trapped ion platform. Other platforms, such as superconducting qubits, do not feature optical transitions and strong coupling to vacuum modes, and therefore do not allow for direct efficient preparation of mixed states. Pure and mixed states are visualized on a Bloch sphere [Nie10] in Figure 2.4.

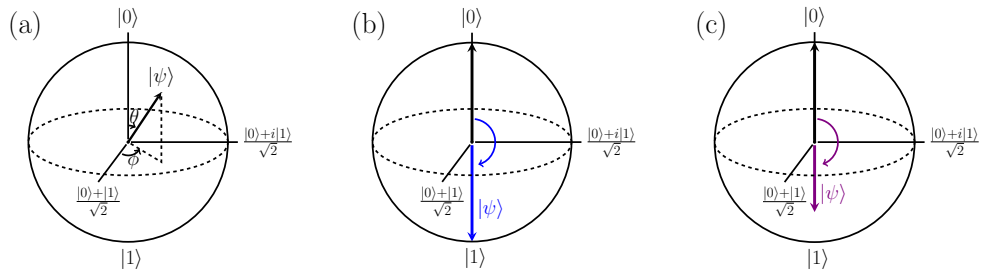


Figure 2.4: Bloch sphere representation of pure and mixed states. **(a)** The pure state space of a single qubit is projected onto the surface of a sphere, with the two basis states $|0\rangle$ and $|1\rangle$ positioned at the poles. Any pure state is geometrically represented by a vector $|\psi\rangle = \cos\theta|0\rangle + e^{i\phi}\sin\theta|1\rangle$, with length 1. Mixed states correspond to vectors with length <1 , lying in the interior of the sphere. **(b)** Initialization to the coherent state $|1\rangle$ (blue). **(c)** Initialization to an incoherent mixture of $|0\rangle$ and $|1\rangle$ (purple). The initial state $|0\rangle$ is shown in black.

Coherent manipulation

For coherent operations on the qubits, we use two laser beams near 397 nm to drive stimulated Raman transitions [Mon95]. If the detuning from the $4S_{1/2} \leftrightarrow 4P_{1/2}$ transition is much larger than the natural linewidth, an effective coupling between the two $4S_{1/2}$ states arises, with an effective coupling strength of [Lei03a]

$$\Omega_{\text{eff}} = \frac{\Omega_{L1}\Omega_{L2}}{2\Delta} e^{-i\phi_{\text{eff}}}, \quad (2.10)$$

where Ω_{L1}, Ω_{L2} are the resonant Rabi frequencies for driving the $4S_{1/2}$ to $4P_{1/2}$ transition with each of the two beams. Importantly, the effective phase is given by the phase difference of the two laser beams, $\phi_{\text{eff}} = \phi_{L2} - \phi_{L1}$. The coherent operations do therefore not rely on the absolute stability of the optical phases, which is a significant simplification.

The choice of the detuning Δ is a compromise between effective Rabi frequency, and coupling to the $4P_{1/2}$ state in the form of spontaneous emission. Since the effective coupling scales as $\Omega \propto I/\Delta$, and the spontaneous emission scales as $R \propto I/\Delta^2$ [Pos10], there is a net decrease of $R \propto 1/\Delta$ if the detuning and the laser intensity I are both increased by the same factor. However, the laser intensity is technically limited as UV light becomes increasingly difficult to handle at higher intensities. Therefore, the detuning is typically set to $\Delta = -2\pi \times 1 \text{ THz}$. Measurements have ruled out spontaneous emission as the limiting factor in the error budget at this detuning.

Since we are using two laser beams, we can choose the effective wave vector by means of the beam geometry $\vec{k}_{\text{eff}} = \vec{k}_{L1} - \vec{k}_{L2}$. This is helpful for coupling to specific motional modes if we want to perform sideband cooling or two-qubit gates. In the case of single qubit gates, we minimize the coupling to any motional mode by employing a pair of co-propagating beams, for which the effective wave vector \vec{k}_{eff} vanishes. This avoids any loss of contrast on Rabi oscillations due to varying phonon numbers. Therefore, we do not need to perform ground state cooling when only working with single qubit gates.

We can realize any single qubit rotation by

$$\hat{R}(\theta, \phi) = \exp \left(-i \frac{\theta}{2} (\hat{\sigma}_x \cos \phi_{\text{eff}} + \hat{\sigma}_y \sin \phi_{\text{eff}}) \right), \quad (2.11)$$

where the Pauli matrices and basis states are represented by

$$\hat{\sigma}_x \equiv \begin{pmatrix} 0 & 1 \\ 1 & 0 \end{pmatrix}, \quad \hat{\sigma}_y \equiv \begin{pmatrix} 0 & -i \\ i & 0 \end{pmatrix}, \quad |\uparrow\rangle \equiv \begin{pmatrix} 1 \\ 0 \end{pmatrix}, \quad |\downarrow\rangle \equiv \begin{pmatrix} 0 \\ 1 \end{pmatrix}. \quad (2.12)$$

The pulse area is given by the effective Rabi frequency and the pulse time $\theta = \Omega_{\text{eff}} t$, and the phase is given by the phase difference between the two beams ϕ_{eff} .

Spin state selective readout

To discriminate between the two spin states, we first map the $|0\rangle \equiv |\uparrow\rangle$ state to the $3D_{5/2}$ state with two rapid adiabatic passage pulses [Mal01], specifically on the transitions⁴ $|4S_{1/2}, m_J = +1/2\rangle \leftrightarrow |3D_{5/2}, m_J = -3/2\rangle$ and $|4S_{1/2}, m_J = +1/2\rangle \leftrightarrow |3D_{5/2}, m_J = +1/2\rangle$. The rapid adiabatic passage pulses consist of 120 kHz chirped pulses, with a sine-squared envelope (see Fig. 2.5b). By slowly changing the eigenstates, the $|\uparrow\rangle$ state population is adiabatically transferred, while being robust against frequency and amplitude drifts [Pos10]. After this mapping operation, the remaining population in the $4S_{1/2}$ state is detected by scattering a saturated 397 nm beam close to the $4S_{1/2} \leftrightarrow 4P_{1/2}$ resonance for 0.8 ms, and counting the number of photons on a photomultiplier tube. The mapping operation is also known as electron shelving [Nag86]. It effectively maps $|\uparrow\rangle / |\downarrow\rangle$ to dark/bright detection, and results in a state discrimination fidelity $>99\%$.

⁴ These transitions were chosen to minimize the effect of magnetic field fluctuations, and to ensure proper quenching via the $4P_{3/2}$ state. However, the rapid adiabatic passage mechanism should cover magnetic field fluctuations. With a suitable polarization for the 854 nm laser (see Chap. 3), all $3D_{5/2}$ substates can be quenched efficiently. For future experiments, it is recommended to use $|3D_{5/2}, m_J = -3/2\rangle$ and $|3D_{5/2}, m_J = 5/2\rangle$ as target states, because the outer regions of the $4S_{1/2} \rightarrow 3D_{5/2}$ spectrum are less crowded with micromotion echos, small motional sidebands, and laser stabilization servobumps.

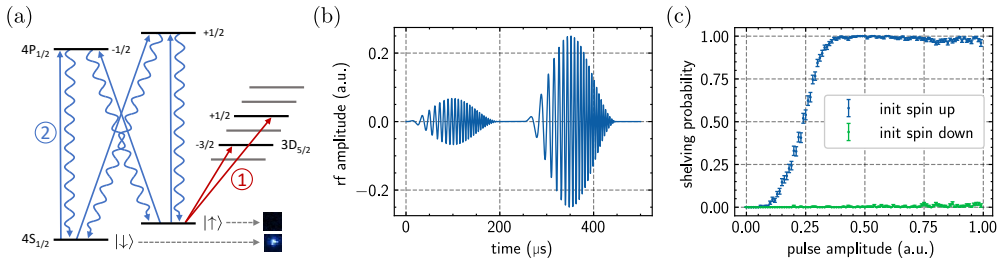


Figure 2.5: Spin readout. (a) First, the $|4S_{1/2}, m_J = +1/2\rangle$ state is adiabatically transferred to two states in the $3D_{5/2}$ manifold, then the remaining population in the $4S_{1/2}$ ground state is detected via fluorescence on the $4S_{1/2} \leftrightarrow 4P_{1/2}$ transition. (b) Two rf pulses, for adiabatic population transfer to either the $|4S_{1/2}, m_J = -3/2\rangle$ or the $|4S_{1/2}, m_J = +1/2\rangle$ state. Each pulse is sine-square-shaped and chirped over 120 kHz, with calibrated amplitudes. The frequencies have been divided by 1000 for demonstration. (c) Calibration curve for one of the pulse amplitudes in (b). Adiabatic transfer of population is shown as a function of pulse amplitude (blue). Undesired excitation of the $|4S_{1/2}, m_J = -1/2\rangle$ state (cross-shelving) is shown in green.

2.2 Multi-qubit entanglement generation - theory and experiment

Entangling gate mechanism and implementation

To generate multi-qubit entanglement, we need to create some kind of coupling between qubits, i.e. between the electronic spin states of several ions. At typical ion distances, the direct magnetic spin-spin coupling lies in the few mHz range and is therefore not sufficient. However, the Coulomb interaction between ions in a crystal leads to shared motional modes and is very well suited for this purpose. There are several popular techniques that use motional modes as a bus for communicating the electronic spin state [Cir95, Sør00, Jon00, GR03, Lei03b, Šaš03, Ber12b]. The most experimentally successful implementations all rely on generating a spin-dependent geometric phase. We will first briefly discuss the general accumulation of a geometric phase in an off-resonantly driven harmonic oscillator, and then our specific implementation, also known as the ‘light-shift’ gate [Lei03b].

In the interaction picture, the Hamiltonian of an off-resonantly driven quantum harmonic oscillator is given by [Roo08a]

$$\hat{H}_{\text{int}}(t) = \hbar\Omega i(\hat{a}^\dagger e^{i\delta t} - \hat{a} e^{-i\delta t}), \quad (2.13)$$

where Ω is the drive coupling strength, $\delta = \omega - \omega_0$ is the detuning between the

driving frequency ω and the resonance frequency ω_0 , and $|\delta| \ll \omega_0$. The creation and annihilation operators a^\dagger and a can be seen as representing the addition and subtraction of phonons, with time-dependent factors due to the off-resonant driving. For the evolution $\hat{U}(t)$ it is possible to write (see [Lee05, Roo08a] for a full derivation)

$$\begin{aligned}\hat{U}(t) &= \lim_{n \rightarrow \infty} \prod_{k=1}^n \exp \left(-\frac{i}{\hbar} \hat{H}_{\text{int}}(t_k) \Delta t \right) \quad \text{with } \Delta t = t/n, t_k = k \Delta t \\ &= \lim_{n \rightarrow \infty} \prod_{k=1}^n \hat{D}(\Omega e^{i\delta t_k} \Delta t) \\ &= \hat{D}(\alpha(t)) e^{i\Phi(t)} \quad \text{with} \quad \hat{D}(\alpha(t)) = e^{\alpha(t) \hat{a}^\dagger - \alpha^*(t) \hat{a}},\end{aligned}\quad (2.14)$$

where the *displacement* $\alpha(t)$ and the *geometric phase* $\Phi(t)$ are given by

$$\alpha(t) = i \frac{\Omega}{\delta} (1 - e^{i\delta t}) \quad \text{and} \quad \Phi(t) = \left(\frac{\Omega}{\delta} \right)^2 (\delta t - \sin(\delta t)). \quad (2.15)$$

The term displacement stands for the normalized complex oscillation amplitude of the driven normal mode. Conceptually, we can see that the displacement is periodic and returns to zero after an interaction time $\tau = 2\pi K/|\delta|$, where K is an integer. After the harmonic oscillator has followed K closed trajectories in phase space, the motion has returned to its original value, but a nonzero geometric phase $\Omega^2 \tau / \delta$ remains.

Now, if we couple the off-resonant driving force to the ion spin state, we obtain a spin-dependent interaction Hamiltonian

$$\hat{H}_{\text{int}}(t) = \hbar \Omega i (\hat{a}^\dagger e^{i\delta t} - \hat{a} e^{-i\delta t}) (\hat{\sigma}_z \otimes \mathbb{1} + \mathbb{1} \otimes \hat{\sigma}_z) \quad (2.16)$$

for two ions. If the ions are prepared in an eigenstate of $\hat{\sigma}_z$, we can replace them by their eigenvalues. Figure 2.6a illustrates how, in this case, states with equal spin move along a closed loop in phase space. For states with opposite spin, the driving force cancels out. We end up with the following truth table

$$\begin{aligned}\{|00\rangle, |11\rangle\} &\rightarrow e^{i\Phi} \{|00\rangle, |11\rangle\} \\ \{|01\rangle, |10\rangle\} &\rightarrow \{|01\rangle, |10\rangle\}.\end{aligned}\quad (2.17)$$

By choosing $\Phi = \pi/2$, and enclosing this geometric phase gate between two single qubit $R(\pi/2, 0)$ rotations, we can create the maximally entangled Bell state $|00\rangle \rightarrow \frac{1}{\sqrt{2}}(|00\rangle + |11\rangle)$.

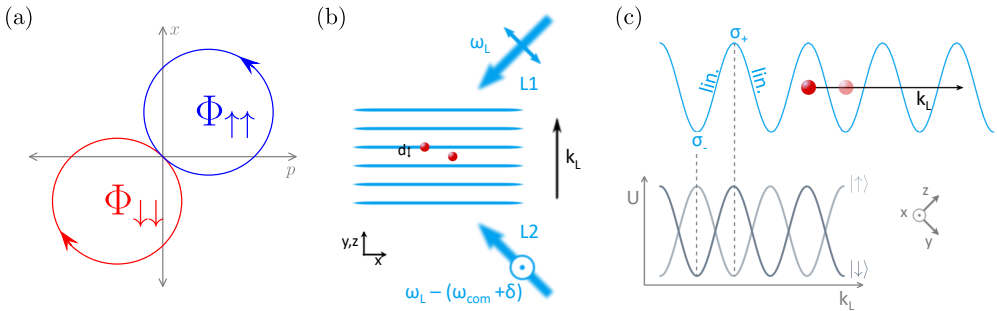


Figure 2.6: (a) State-dependent trajectory in phase space. Two-qubit states with equal spin move along a closed loop. The geometric phase pickup is given by the area of the loop and determined by the driving strength. To disentangle spin and motion at the end of the gate, the loop must be closed. (b, c) Beam geometry that generates a travelling standing wave. Polarization and k -vectors of the two beams and resulting wavefront are indicated. Depending on the orientation of the ions to the wavefront, the com or rocking mode can be driven. In (c), the resulting spin-dependent potential is indicated.

To realize the described interaction, we overlap two laser beams such that their difference k -vector $\Delta\vec{k} = \vec{k}_{L1} - \vec{k}_{L2}$ points in the radial trap direction. The beams are far detuned from the $4S_{1/2} \leftrightarrow 4P_{1/2}$ cycling transition, far as compared to the natural linewidth and the dipolar Rabi frequency. The beams have a mutually orthogonal linear polarization and a relative frequency difference $\Delta\omega = \omega_{\text{COM}} + \delta$, close to the radial com mode frequency ($|\omega_{\text{COM}}| \gg |\delta|$). The polarization interference produces a standing wave which is travelling at the frequency difference between the two beams, $\Delta\omega$ (see Figure 2.6b,c). The electric field gives rise to a Stark shift and a corresponding optical dipole force, which is both polarization- and spin-dependent. Due to the linear \perp linear polarization of the two beams, the resulting polarization ranges from σ^- , to linear, to σ^+ , creating a periodic and opposite potential for the two spin states. If two ions with equal spin are aligned along the wavefront, they will experience a periodic driving force at frequency $\Delta\omega = \omega_{\text{COM}} + \delta$. However, if they have opposite spin states, they will experience opposite forces, which does not drive the com mode. This is exactly the spin-dependent off-resonant driving force we have described earlier.

Note that we can play around with the orientation of the ions and the difference frequency $\Delta\omega$, and thereby choose which motional mode we drive, on which spin states: If the projection of the ion distance⁵ along the two-beam resultant k -vector $\Delta\vec{k}$ equals

⁵ For gates using an axial motional mode this would be the distance along the trap axis, controlled by the axial trap frequency. For gates using a radial motional mode this would be the distance orthogonal to the trap axis, controlled by tilting the two-ion crystal.

$d = \pi(2n + 1)/\Delta k$, $n \in \mathbb{N}$, and the ions have opposite spin, they would still experience the same force, and we could drive the com mode on opposite spin states. On the other hand, if $d = 2\pi n/\Delta k$, the ions have opposite spin, and we change the frequency to $\Delta\omega = \omega_{\text{rock}} + \delta$, we could drive the rocking mode. Choosing a different motional mode does not affect the unitary gate, but it could affect the error rate, since the motional modes have different heating rates.

Error mitigation

The main error sources connected to the light shift gate are thoroughly explored in [Bal14]. Here, we will only discuss the following error-mitigating measures that have been taken in this experiment and mention the connected error sources:

1. Ground state cooling
2. Active stabilization of Raman beam power, magnetic field, and rf drive
3. Alignment of the ions and laser beams
4. Pulse shaping
5. Spin echo pulse
6. Well-defined phase relation between light shift pulses

1. Ground state cooling

In general, the return time (the time after one period of displacement, when spin and motion are again decoupled), and the geometric phase (Eq. 2.15) do not directly depend on any motional mode occupation number. The light shift gate is robust to small excitation, as long as we are still in the Lamb-Dicke regime, where the spread of the ion wavefunction is small compared to the wavelength of the light and the coupling between the ion's internal and motional states is sufficiently small ($\eta \ll 1$) [Win98, Lei03a]. However, the coupling strength depends on the occupation of the gate-mediating mode and all spectator modes. With increasing motional excitation, the wavepacket is more delocalized across the drive field and the effective force decreases. This can be to some extent compensated by drive power, however as there is a coupling strength dispersion, it is not possible to fully compensate, both for thermal and displaced states. Therefore, we perform sideband cooling on all radial modes before starting any sequence that includes two-qubit gates.

2. Active stabilization of Raman beam power, magnetic field, and rf drive

In this category we are dealing with slow drifts and fast fluctuations, relative to the two-qubit gate duration. Slow drifts of the Raman beam power will act as mis-set Rabi frequency, which leads to values of the geometric phase that deviate from the desired one. Slow drifts of the qubit frequency splitting due to magnetic field changes will act as mis-set gate detuning. Mis-set gate detuning leads to nonzero excitation of the gate mode after the gate pulse(s), which leads to entanglement between spin and motion, and therefore to effective spin decoherence. Magnetic field drifts also affect qubits in superposition states by adding a nontrivial phase, as the Larmor precession frequency depends on the magnitude of the quantizing field. Slow drifts of the radial trap frequency will also act as mis-set gate detuning. Since we are using the radial modes, the radial trap frequencies are determined by the amplitude and frequency of the rf trap drive (see chapter 3). Fast fluctuations of any of these parameters will appear as noise that increases motional heating and dephasing. Motional heating or dephasing while the spin state is coupled to the motional state leads to errors. Therefore, we need to stabilize the Raman beam power, the quantizing magnetic field, and the rf drive amplitude and frequency on the slow (seconds to hours) and fast (microsecond) timescales.

3. Alignment of the ions and laser beams

If the laser beams are not perfectly centered on the two-ion crystal, the Raman Rabi frequency will be different for each ion. This means that, in general, each binary spin state will have a different coupling strength. If $\Omega_{\downarrow} = \Omega_{\uparrow}$, the force magnitude will be equal for $|\uparrow\uparrow\rangle$ and $|\downarrow\downarrow\rangle$, and also equal for $|\uparrow\downarrow\rangle$ and $|\downarrow\uparrow\rangle$. By adjusting the beam power, this can be calibrated. If, however, $\Omega_{\uparrow} \neq \Omega_{\downarrow}$, then each of the 4 spin states has a different force magnitude, and hence gains a different geometric phase. This gives an error in the gate operation that cannot be compensated for with a Raman beam power adjustment alone [Bal14]. To minimize this error, we perform a daily alignment of each beam individually on a crystal of two ions. We optimize for equal Rabi frequency and equal Stark shifts, measured by Ramsey interferometry [ROO08b]. Any remaining imbalance will be compensated by the spin echo technique described below.

As discussed before, the orientation of the ions relative to the wavefront of the standing wave determines the coupling of the spin-dependent force to each of the 4 spin states. If we choose to drive the radial com mode on the even states ($|\uparrow\uparrow\rangle, |\downarrow\downarrow\rangle$), we should align either the ions or the beams such that the projection d of the ion distance

along the resulting wave vector $\Delta\vec{k}$ is $d = 2\pi n/\Delta k$, where $n \in \mathbb{N}$. Since it is technically more convenient than moving the laser beams, we apply a small rotation to the two-ion crystal before every gate. The amount of rotation is calibrated by maximizing the motional excitation of the com mode at half the return time of the geometric phase gate. If the beams are well-centered on the ions, it is usually not necessary to change this value on a daily basis. For the experiments in this thesis, a rotation angle of $2.392(7)$ arcminutes was used.

4. Pulse shaping

A rectangular pulse, which is technically the easiest to implement, has a Fourier transform that contains many frequencies, and will therefore cause significant excitation on spectator modes. On the other hand, a sine-shaped pulse, which is much narrower in frequency space, has an area that depends much more strongly on the pulse duration. This means that the effect of a mis-set detuning or mis-set pulse duration is much greater for a sine-shaped pulse than for a rectangular pulse. Additionally, the polarization varying standing wave interference pattern will cause an oscillating light shift error [Bal14]. Most of this error will cancel out, but a small part remains, depending on the pulse shape. The remaining error will be much less significant for a pulse that is slowly turned on, due to the lower amplitudes at the start and end of the pulse. Figure 2.7 illustrates several pulse shapes and their respective geometric phase as a function of pulse duration. As shown, another important feature, which is most present with rectangular pulses, is a plateau w.r.t. the geometric phase at the return times. We found that a smooth rectangle pulse is the best compromise, using a risetime of 10% of the pulse duration. However, we also found a small interdependency between the optimal pulse duration and the optimal amplitude, which makes it hard to calibrate these individually. This interdependency might be avoided with a risetime that is independent of the pulse duration. According to [Bal14, p. 52], with $N \in \mathbb{Z}$ and f_Z for the gate mode motional frequency, a risetime of $t_{\text{rise}} = \frac{N+0.5}{f_Z}$ should result in the lowest off-resonant excitation.

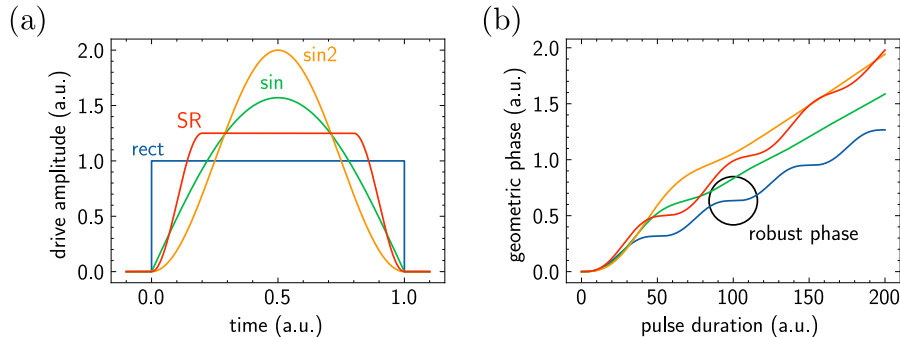


Figure 2.7: (a) Drive amplitude, and (b) resulting geometric phase, for different pulse shapes. A rectangle pulse has the most robust geometric phase around the return times, but also the strongest off-resonant excitation on spectator modes. A smooth rectangle (SR) pulse is the best compromise (shown in red).

5. Spin echo pulse

Any error source that is asymmetric w.r.t. the spin state can be compensated by implementing a two-loop gate with a single qubit $R(\pi, 0)$ rotation on both ions in between the two loops. This includes unequal illumination, and uncompensated ac Stark shifts. Another advantage of using two pulses with each a geometric phase of $\Phi = \pi/4$ is that the individual driving pulses and loops in phase space have smaller amplitudes, leading to less absolute pulse amplitude noise, and a decreased sensitivity of the motional state to noise. Naturally, the total gate time will be longer, which increases the scattering, motional heating, and decoherence errors. Figure 2.8 shows the pulse sequence for a two-loop gate, including spin-echo pulse and enclosing $\pi/2$ pulses, for creating a Bell state.

6. Well-defined phase relation between light shift pulses

For a two-loop gate, we found that the phase relation between the two optical dipole force (ODF) pulses has a strong effect on the gate mechanism, which can be used both for precise calibration, and for making the gate more robust. A calculation of the residual motion after two ODF pulses, as a function of pulse duration and relative phase difference, is shown in Figure 2.9. As illustrated, we can tune the phase of the second pulse to either enhance or undo the residual motion created by the first pulse. In particular, we can find a phase at which the combination of the two loops always returns to the origin in phase space, independent of the pulse duration, and vice-versa. At the intersection of these two lines, we define the ‘double sweet spot’. Here, two closed loops in phase space are completed, and the gate is robust against

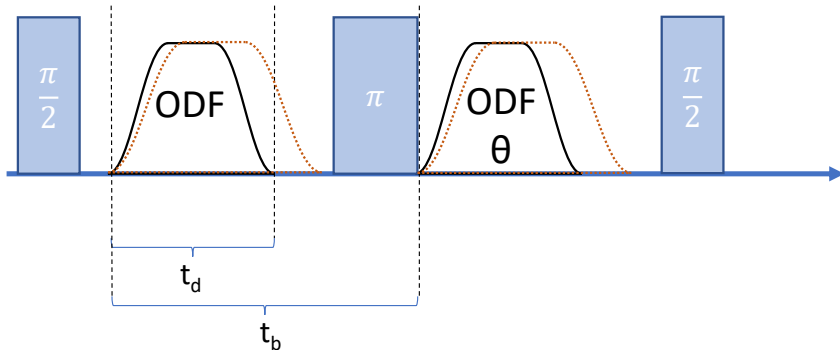


Figure 2.8: Two-loop gate with a spin echo (π) pulse between the two optical dipole force (ODF) pulses. The time between the start of the two pulses is fixed (t_b) and independent of the ODF pulse duration (t_d). θ refers to the relative phase difference between the two ODF pulses. Including the enclosing $\pi/2$ pulses, this sequence generates a Bell state $|00\rangle \rightarrow \frac{1}{\sqrt{2}}(|00\rangle + |11\rangle)$.

trap frequency drift (leading to a vertical shift of the excitation pattern) and mis-set pulse duration. On the other hand, if we tune the phase of the second pulse by a π offset away from this point, the final motional excitation is highly dependent on the pulse duration. This ‘anti-sweet spot’ is very helpful for precise calibration.

To measure the residual excitation after two ODF pulses, we perform a π pulse on the first red sideband of the gate mode. The Rabi frequency depends on the phonon number n as $\Omega_n^{(\text{rsb})} = \eta\Omega\sqrt{n}$, where η is the Lamb-Dicke parameter [Win98] and Ω is the carrier transition Rabi frequency. With a fixed π pulse duration, and for low phonon numbers, the excited state population is proportional to the phonon number. The full measurement protocol is illustrated in Figure 2.10. After initialization to $|00\rangle$, an optional $R_x(\pi)$ pulse is used for initialization to an odd binary spin state ($|01\rangle$ or $|10\rangle$). Before and after the ODF pulses, the ion crystal is rotated back and forth for alignment to the spin-dependent potential wavefront. An optional $R_x(\pi)$ spin echo pulse on both qubits is included, as for the full two-qubit gate. All optional $R_x(\pi)$ pulses are repeated to ensure that the spin state is back to $|00\rangle$ before the final $R_{\text{rsb}}(\pi)$ pulse projects the residual motion to the spin state, and a measurement is performed.

Note that the phase of the second ODF pulse is only well-defined if the time between the start of the two pulses is constant, rather than the time between the end of the first and the start of the second pulse. Otherwise, the pulse duration and effective phase are interdependent, and the sweet spot breaks down. Therefore, we included a buffer time, i.e. a fixed time between the start of the pulses. Measurements of the residual excitation after two ODF pulses are shown in Figure 2.11, (a) without and

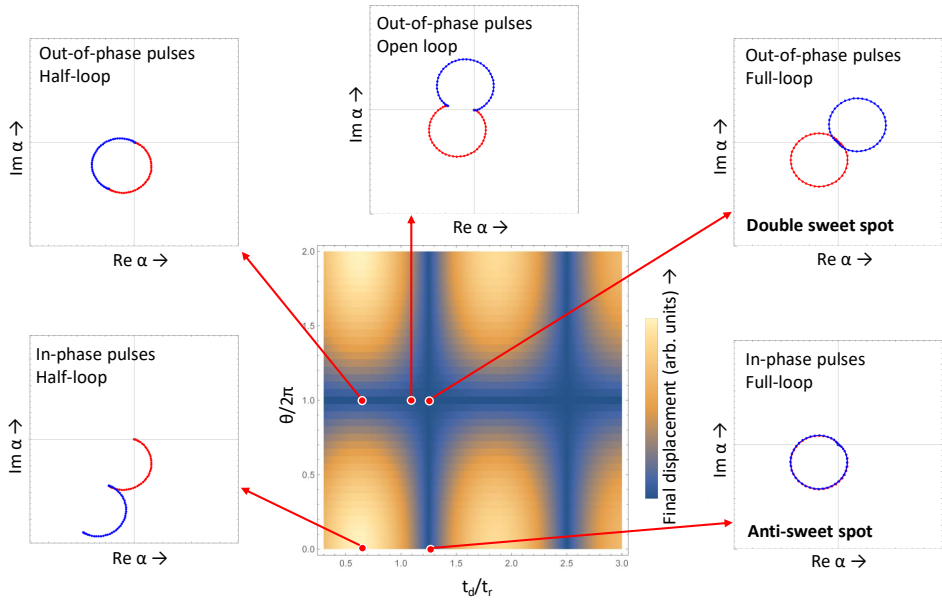


Figure 2.9: Center panel: Calculation of the residual motional excitation of the gate mode, as a function of pulse duration and relative phase of the second ODF pulse (see Fig. 2.8). The second pulse can either amplify, or cancel the residual motion after the first pulse. The most robust gate is performed by doing two full loops in opposite direction, labeled here as double sweet spot. The outer panels show phase space trajectories for various different parameter pairs.

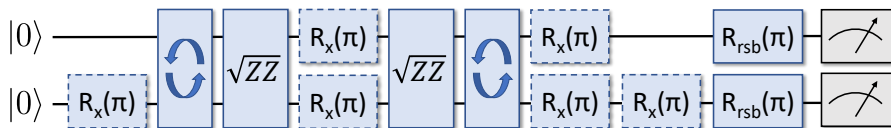


Figure 2.10: Protocol for measuring residual motional excitation after a two-loop geometric phase gate. Alignment of the ions to the wavefront is performed before and after the \sqrt{ZZ} ODF pulses. There are two optional $R_x(\pi)$ pulses on the second qubit for probing odd spin states, and two optional parallel $R_x(\pi)$ pulses for undoing the optional spin-echo spinflip. The red sideband pulses are usually performed on the same mode as the ODF pulses.

(b) with a buffer time. Panel (c) illustrates that there is no statistically significant excitation on the rocking mode when performing the ODF pulses close to the rocking mode frequency on an even state ($|00\rangle$). This confirms that the ions are perfectly aligned to the wavefront of the spin-dependent potential.

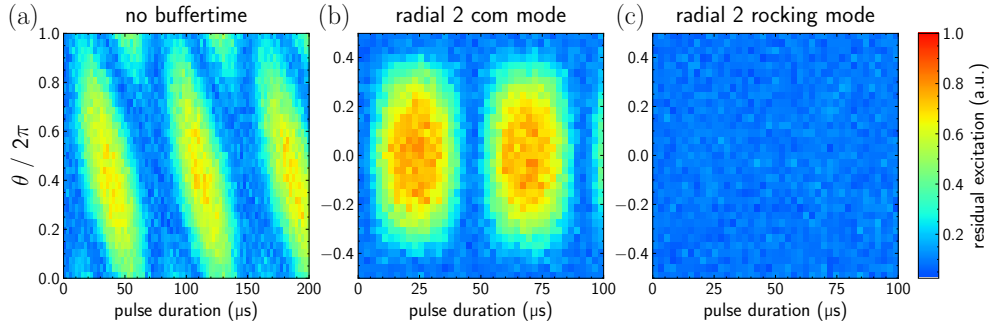


Figure 2.11: Measured residual motional excitation for two ODF pulses on the radial 2 com mode, as a function of pulse duration and relative phase of the second ODF pulse. (a) Without buffer time. (b) With buffer time. (c) With buffer time, performing the ODF pulse and measuring excitation on the radial 2 rocking mode instead, indicating the amount of excitation due to misalignment. The data in (c) did not show statistically significant excitation above the SPAM error, suggesting optimal alignment of the ions to the ODF wavefront. Residual excitation is probed by performing a π pulse on a red sideband after the gate, see Fig. 2.10.

Daily calibration

For daily calibration we optimize all parameters that are related to Raman beam alignment, qubit & trap frequencies, and beam intensity (see Table 2.3). Frequencies are finely calibrated using Ramsey measurements [ROO08b, Rus16]. For the shelving RAP amplitudes we observe the final bright/dark populations, as shown in Fig. 2.5c. Raman beam Stark shift is measured by varying a single-beam Raman pulse duration during a Ramsey measurement on the $4S_{1/2} \leftrightarrow 3D_{5/2}$ transition [Pos10]. The beams are moved with the help of piezo-controlled mirror holders (see Chap. 3). Pulse durations are finely calibrated by varying around a multiple (10x) of the to-be-calibrated pulse duration and observing Rabi oscillations. The sideband cooling reference time is the π pulse duration on the first red sideband of the radial 1 com mode. After calibration, sideband cooling is tested by performing a π pulse on the red sideband of the respective mode. When the ion is close to the ground state, the red sideband cannot be driven and the ion will stay in the initial state $|m_J = +1/2\rangle$, resulting in a dark detection after shelving.

Category	Parameter	Order of magnitude	Approx. daily drift
Shelving $4S_{\frac{1}{2}} \leftrightarrow 3D_{\frac{5}{2}}$	Carrier frequency (3x)	729.34756 nm	1.43 kHz
	π pulse duration (3x)	10 μ s	0.38 μ s
	RAP amplitude (2x)	4-8 mW	0.4 mW
Single qubit	Carrier frequency	$2\pi \times 10.5$ MHz	0.25 kHz
	$\pi/2$ pulse duration	1.3 μ s	0.1 μ s
	π pulse duration	2.10 μ s	0.1 μ s
Two-qubit	Tilt offset voltage for separating a two-ion crystal	7.5 mV	4.2 mV
	Align Raman beams for equal Stark shift on 2 ions (2x)	200 kHz	5%
	Sideband frequencies com mode (6x)	$2\pi \times (10.5 \pm N^*3.8/4.6)$ MHz	1.2 kHz
Sideband cooling	Sideband frequencies rocking mode (6x)	$2\pi \times (10.5 \pm N^*3.5/4.3)$ MHz	0.25 kHz
	Sideband cooling reference time	10 μ s	1.5 μ s
	Relative phase of 2nd ODF pulse (θ)	$-\pi$ to π rad	$\pi/40$ rad
Geometric phase gate	ODF pulse duration	50 μ s	0.5 μ s
	ODF pulse amplitude	~ 3 mW	0.3 mW

Table 2.3: Daily calibrated gate-relevant parameters, order of magnitude, and approximate day-to-day drifts. For sideband cooling, the frequencies of the 1st red, 2nd red, and 1st blue sidebands are calibrated, for both radial modes.

When spin readout, single qubit gates, and sideband cooling are calibrated, and the beams are centered on a two-ion crystal, we proceed with the two-qubit gate parameters, namely ODF pulse duration, phase of the second pulse, and pulse amplitude. From the daily calibrated transition frequencies, we derive the required laser frequencies for an off-resonant drive detuning $\delta = 2\pi \times 20$ kHz. The actual δ_{eff} will vary because the beams used for frequency calibration give rise to an ac Stark shift mediated by the strong carrier transition, which is not there with the gate beams, due to a difference in polarization (see Chap. 3). This can be absorbed in the calibration of the ODF pulse duration, since the return time is $t_r = 2\pi/\delta$. Knowing the expected t_r , we start by scanning the phase of the 2nd ODF pulse at half the return time duration, while measuring the residual excitation with a π pulse on the red sideband of the gate mode. This is effectively a vertical cut-through of Fig. 2.11b, giving us the phase θ for minimal and maximal residual excitation. Then we fix θ at maximal excitation and scan the ODF pulse duration (a horizontal cut-through across the earlier described anti-sweet spot). We now know the location (in terms of t and θ) of the anti-sweet spot for sensitive calibration, and the sweet spot for robust operation. Then we calibrate the ODF pulse intensity by creating a Bell state using the pulse sequence of Fig. 2.8 and measuring the binary probabilities $\{p_{|00\rangle}, p_{|01\rangle}, p_{|10\rangle}, p_{|11\rangle}\}$, see Fig. 2.12a. When scanning the ODF pulse duration for a full two-loop gate, we find that the odd states are strongly suppressed around the sweet spot (Fig. 2.12b), as compared to around the anti-sweet spot (Fig. 2.12c).

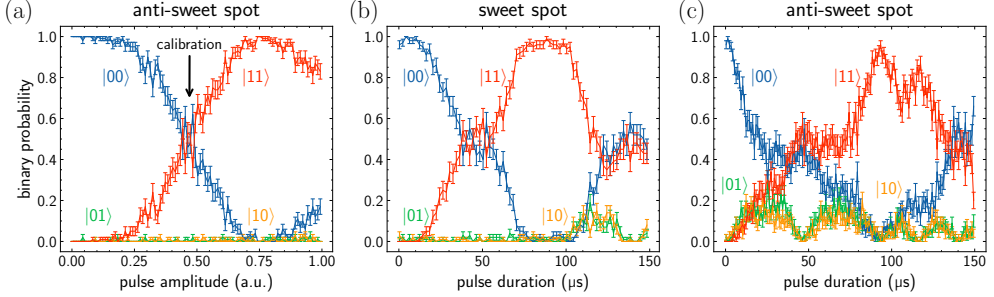


Figure 2.12: Binary state probabilities after performing a two-loop gate (Fig. 2.8). (a) ODF pulse amplitude calibration. For daily calibration, the target state is $\frac{1}{\sqrt{2}}(|00\rangle + |11\rangle)$, indicated by the arrow. The anti-sweet spot (see Fig. 2.9) is used for maximum precision. (b) ODF pulse duration scan around the sweet spot, and (c) around the anti-sweet spot. Odd states are mostly suppressed in (b), leading to a robust gate operation.

2.3 Tomography and benchmarking - theory and experiment

State tomography

Now that we understand the gate mechanism, and have calibrated the important parameters, we describe how to verify that single and two-qubit operations are working properly. One commonly used method of benchmarking a two-qubit state is quantum state tomography [Vog89, ROO04, Lvo09]. It involves measuring the operators $\{\sigma_z, \sigma_y, \sigma_x\}$ for each qubit, resulting in 3^N bases for N qubits, where each operator should be measured with adequate precision to detect the exponentially small populations for most bases. Figure 2.13 shows a state tomography measurement for a two-ion Bell state with a state fidelity $\mathcal{F}(\hat{\rho}) = \max_{\theta} \langle \Psi(\theta) | \hat{\rho} | \Psi(\theta) \rangle$ of 99.8%, with respect to a Bell state of arbitrary relative phase θ : $|\Psi(\theta)\rangle = \frac{1}{\sqrt{2}}(|00\rangle + e^{i\theta} |11\rangle)$. This type of benchmarking has been extended in the current setup up to measuring 81 bases for a four ion GHZ state, after applying 4 sequential two-qubit gates [Kau17c]. Clearly, this approach does not scale very well with the number of gates or qubits. We could also ask if this is the kind of metric that we want to use for benchmarking our quantum processor. It just measures how well we can prepare one specific state, whereas a general quantum processor can be expected to perform well over a whole range of operations and states. Another commonly used method is quantum process tomography: By preparing in 4^N and measuring in 3^N bases, a process is completely characterized. The scaling is even less favorable, and is practically limited to three qubits [Wei04, Kau17b].

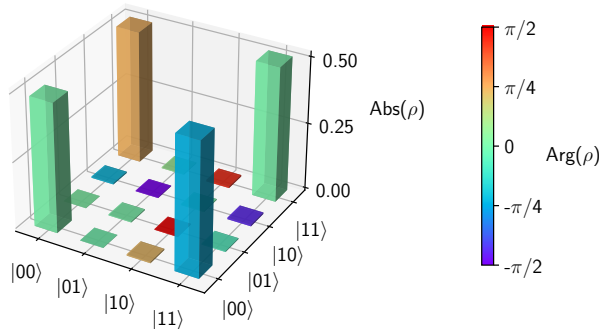


Figure 2.13: Density matrix reconstruction for a state tomography measurement, showing 99.8% fidelity for creating a Bell state. 8000 repetitions were measured, for each of the 9 basis states.

Randomized and cycle benchmarking

One widespread method for quantifying gate fidelities is randomized benchmarking [Kni08]. A random unitary U consists of a sequence of length N , containing N gates that are to be characterized. U is applied to a fixed initial state, after which the inverse unitary U^{-1} is applied, and the survival probability of the initial state is measured. U^{-1} is performed by the lowest number of operations possible. Since the gates that make up the unitaries are faulty, and the errors are not expected to fully cancel each other, the survival probability will be smaller than one.

$$|\langle \psi_i | \psi_f \rangle|^2 = |\langle \psi_i | V^{-1}V | \psi_i \rangle|^2 \leq 1, \quad (2.18)$$

where V and V^{-1} denote the faulty unitaries. This expression only holds for coherent error sources, incoherent error sources can be covered by a density matrix notation along the same lines.

The average error per gate is obtained from the increase in error probability as a function of the number of gates in the unitary U . Compared to tomography, this method is much more fitting for a number of reasons: It mimics the realistic operation of a quantum processor since it deals with the average error in a longer sequence of gates, i.e. it takes into account the n th gate acting on a random input state. Whereas methods such as state tomography require more data $\propto 1/\epsilon^2$ to verify small infidelities ϵ , randomized benchmarking can just make use of longer sequences, i.e. the measurement effort scales only as $1/\epsilon$. State preparation and measurement (SPAM) errors incur only once per measurement. For longer sequences, randomized benchmarking takes into account the error behavior in time, i.e. drifts on a longer timescale than individual

gates are included. There are no extra gates required for state projection that need to have a lower error rate than the gates that are to be benchmarked, as in for example state tomography. And, most importantly, the number of measurements in the current implementation scales only linearly with the number of qubits.

An initial basis-changing rotation is randomly chosen from $\{\hat{R}_x(\pi/2), \hat{R}_y(\pi/2), \hat{R}_z(\pi), \mathbb{1}\}$. Then, the randomly chosen gates that make up U are taken from the Clifford group, which is generated by single qubit $\pi/2$ rotations of the form $e^{-i\hat{\sigma}\pi/4}$ with $\hat{\sigma}$ a product of Pauli operators $\{\mathbb{1}, \hat{\sigma}_x, \hat{\sigma}_y, \hat{\sigma}_z\}$ [Got98, Bal16]. It effectively divides the Bloch sphere into 12 possible rotations and combinations thereof. One reason why Clifford gates are used in conjunction with randomized benchmarking is that also for larger registers, the action of these can be computed efficiently on classical computers [van08], therefore the final rotation can be determined easily. With respect to randomized benchmarking representing general operations on a quantum computer, provided that the errors in these Clifford operations are tolerated, other operations needed for universality can be implemented by state purification [Bra05, Kni05]. When the theoretical unitary U is known, the final state is randomly chosen as either $|0\rangle$ or $|1\rangle$, and the final operation U^{-1} in terms of the 12 possible rotations is computed. The measured bright/dark detection probabilities are then compared to the expected outcome to obtain the *success rate*.

So far we have only dealt with a single qubit. For two qubits we could extend our collection of operations to the 2-qubit Clifford group. However, since implementing each Clifford requires $\mathcal{O}(N^2/\log_e N)$ primitive two-qubit operations [Aar04], this approach provides very coarse information about the primitive operations. Furthermore, a single 10-qubit Clifford operation will have a cumulative error on the order of 100 times the error of a single two-qubit gate, which substantially increases the number of measurements required to accurately estimate the process fidelity [Erh19]. Instead, we take an approach where we perform cycles of single qubit Clifford rotations on both qubits in parallel, alternated with two-qubit entangling gates, see Fig. 2.14. The final operation U^{-1} now consists of two single qubit rotations and an optional disentangling gate in between. With the parallel single qubit operations restricted to identical operations, we operate in the subspace of a pair of qubits in line with [Bal20]. The advantage is that we can perform all operations with a global beam and do not need to separate the two-ion crystal until the final detections (see Chap. 3).

After daily calibration, we typically perform a quick benchmark using a preselected set of sequences of one particular length M . From the average success rate \mathcal{F}_M , a single gate fidelity proxy is then calculated as $\mathcal{F}_1 = \sqrt[M]{\mathcal{F}_M}$, without taking into account

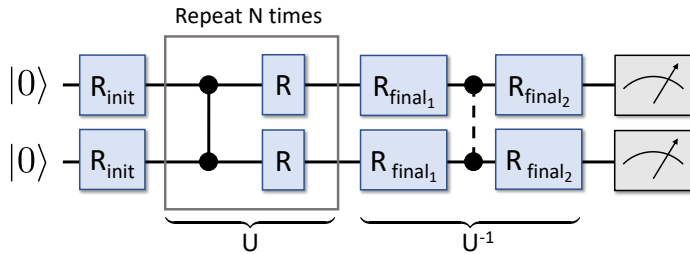


Figure 2.14: Quantum circuit for global cycle benchmarking. All single qubit gates are performed on both qubits in parallel using a global laser beam, and are randomly chosen from the Clifford group. The single qubit gates R are different for each iteration. The final gates are calculated to randomly project the qubit state to either $|0\rangle$ or $|1\rangle$ and the final phase gate is optional.

SPAM parameters or measuring scaling as a function of sequence length. Using the same balanced set of sequences every day ensures having a proper reference, as some sequences are more sensitive to specific error sources than others. Measuring 250 repetitions per sequence, for 20 sequences of length 20, is usually enough to obtain consistent results. Best measured fidelities for this quick reference benchmark are 99.74(5)% per two-qubit gate, and 99.98(1)% per single qubit gate for the earlier described randomized benchmarking.

Full measurements of randomized- and cycle benchmarking success rates as a function of sequence length are shown in Figure 2.15. In this case, the mean success rate can be fitted to a scaling model for the expected success rate as a function of the number of gates: $S(N) = S_B + (S_{\text{spam}} - S_B)\mathcal{F}^N$, where S_B is the baseline success rate for $N \rightarrow \infty$, S_{spam} is the SPAM error, N is the number of gates, and \mathcal{F} is the single gate fidelity. For both the single- and two-qubit case, we can see a clear spread in success rate for different sequences. This difference in sensitivity is attributed to the amount of time that is spent in a superposition state. The fitted single gate fidelities are 99.96(21)% for single qubit gates and 99.19(13)% for two-qubit gates in these particular measurements.

Cycle benchmarking as a tool for parameter optimization

Cycle benchmarking can also be used as a tool for optimizing all gate control parameters. Fig. 2.16 illustrates how the measured bright probability for a number of fixed random cycle benchmarking sequences varies while scanning the ODF pulse duration. The expected outcome for any particular sequence is either 0 or 1. We observe a region with relatively high success rates for some sequences, beyond which the success rates quickly decay to 0.5. Again we see that some sequences are more sensitive than others,

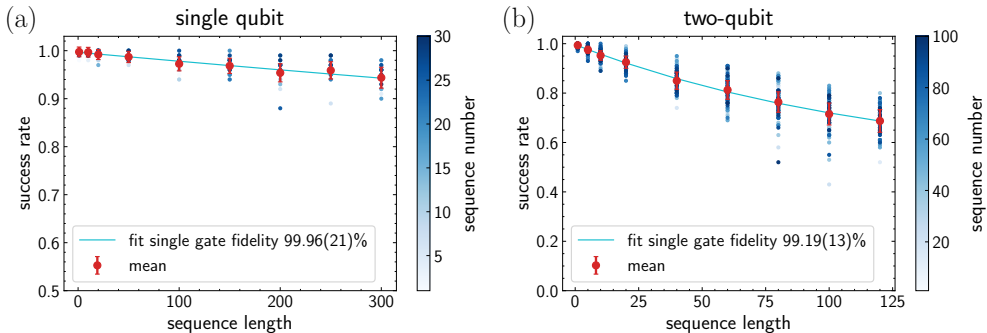


Figure 2.15: Randomized and cycle benchmarking, showing success rate as a function of the sequence length. (a) Single ion randomized benchmarking for 30 different sequences at each length. (b) Two-ion cycle benchmarking for 100 different sequences at each length.

which also depends on which parameter we are scanning. For any parameter we can tune the sensitivity by choosing specific sequences and varying the number of gates. Note that this is a ‘black box’ approach: We tune any parameter and observe the result on the final gate fidelity. It is most useful for fine-tuning, when all parameters are already close to their optimum.

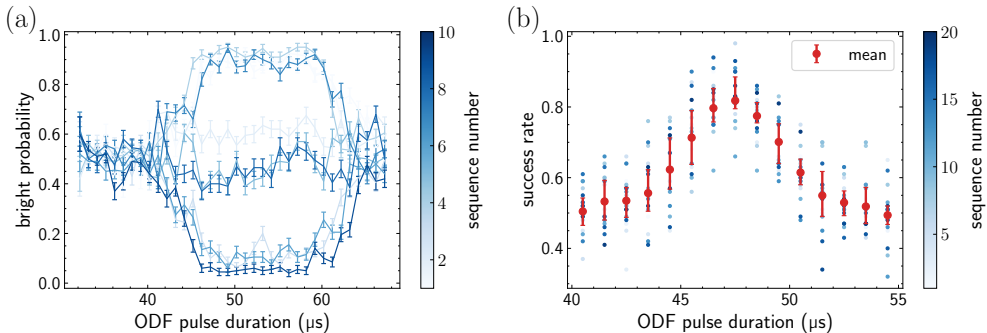


Figure 2.16: Cycle benchmarking while scanning ODF pulse duration. (a) Bright probabilities for a number of random sequences with expected outcome 0 or 1. (b) Success rates for a preselected set of 20 sequences, each containing 20 gates. The error bars in (b) indicate the region from first quartile, to mean, to third quartile.

Long-term gate stability

For longer data acquisition it is essential that the gate fidelities stay at a high level and no frequent recalibration is required. When the fidelities eventually start to degrade, it is important that we know which parameters are involved and how to

quickly recalibrate them. Cycle benchmarking is an excellent tool for continuously monitoring the stability, as measurements take little time⁶ and random sequences can be chosen for near-arbitrary sensitivity without significantly affecting the measurement time. Putting all that we have learned about robust, high fidelity gates to the test, we measured success rates for the reference set of 20 random sequences containing 20 two-qubit gates, during a 12 hour session. Results are shown in Figure 2.17. In parallel, we monitored laser wavelengths, transition frequencies, laser intensities, and qubit state readout. The measurement gap of \sim 30 minutes is due to a laser unlock. There were no intermediate recalibrations. The gates proved robust against a qubit frequency drift of 500 Hz, as the overall success rate could only be correlated with a decrease in fluorescence, which in turn was due to a drifting repump laser. Starting with a success rate of 99.59(5)% and ending with 99.37(5)%, we calculate an average 12-hour success rate of 99.40(29)%. These measurements were taken without the active magnetic field stabilization described in Sec. 3.3.

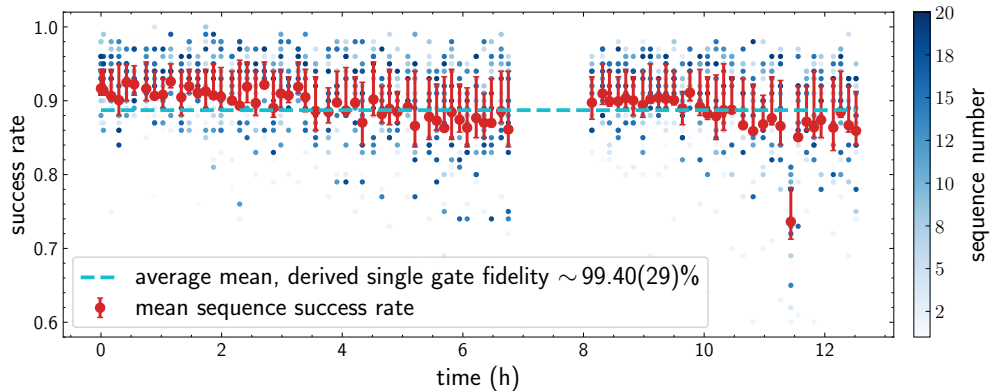


Figure 2.17: Repeated cycle benchmarking stability measurement for a 12 hour period. The missing datapoints are due to a laser instability that automatically paused the measurement. No recalibrations were performed. With each sequence containing 20 two-qubit gates, the single gate fidelity is computed as $f = \sqrt[20]{\text{average mean success rate}} = 99.40(29)\%$.

⁶ Typically < 1 minute for the quick benchmark measurements presented in this thesis, which are using 20 sequences, each containing 20 gates, and providing an accuracy of $\sim 0.05\%$.

Outlook

By optimizing the two-qubit gates and measuring their stability we gained a lot of experience in which parameters are important and how they drift. There are already many background tracking procedures in place, and the first steps have been made towards fully automated periodic recalibration. With a robust $< 1\%$ error rate we are in a good position to start working on integrated active error correction [Rau07, Ber17]. Still, cycle benchmarking remains a ‘black box’ method as it does not directly reveal particular error sources. Also, it requires its own measurement protocol, which would have to be run interleaved with measurements and does not necessarily reveal the most relevant error sources for the particular measurement at hand. In Chapter 4 we will introduce a framework that discriminates between unitary and non-unitary error sources, and that can be applied to any unitary quantum circuit.

Chapter 3

Experimental Setup

This chapter addresses the technical implementation of the elements from Chapter 2. In Section 3.1 we discuss the heart of the quantum processor, which is a multi-layered segmented linear Paul trap. The rf trap drive stabilization is discussed, which is crucial for obtaining long motional coherence times, and the operations that provide a scalable quantum register are considered. In Section 3.2 we discuss the next layer of the setup, which is formed by the vacuum chamber, the magnets that provide a quantization axis for the spin qubit, and the magnetically shielding μ -metal enclosure. Section 3.3 addresses the additional active magnetic field stabilization, which uses two 3D fluxgate sensor packs and three pairs of large coils in Helmholtz configuration, to suppress external magnetic field changes. In Section 3.4 we discuss the laser light sources and optical setup for ion loading and qubit operations. In Section 3.5, the control infrastructure, and the arbitrary waveform generator that provides time-dependent voltages for the dc electrodes are discussed. As the majority of components were initially developed and described in earlier works [Kau17a, Rus17a, Kau19], the descriptions are kept brief, and details are only discussed when additions or improvements are involved.

3.1 Multi-layered segmented linear Paul trap

The heart of the setup is formed by a segmented linear Paul trap, consisting of 32 pairs of dc electrodes and interconnected rf electrodes (see Figures 3.1 and 3.3). The electrodes are constructed from two 127 μm Al_2O_3 wafers, which are laser machined, gold-coated, and separated by an insulating 254 μm alumina spacer layer. The electrodes have a width of 166 μm , a depth of 143 μm , and are separated by 34 μm isolation trenches. The trap slit measures $12.84 \times 0.384 \text{ mm}^2$. These dimensions were chosen to balance optical access with the possibility for high electrical fields at the position of the ions, which are needed for tight confinement and fast time-dependent control of the trapping

potentials. Fabrication of the trap consisted of five steps: The trap slit and electrodes are laser machined using a femtosecond laser, followed by evaporation of a 50 nm titanium and 500 nm gold layer to create the inert electrical surfaces. A second round of laser machining separates the electrodes from each other. The thickness of the gold layer is increased to $\sim 8 \mu\text{m}$ by electroplating. This has led to lower heating rates, which might be due to lower electrical noise. Finally, the chips are diced for electrical isolation of the electrodes, and assembled under the microscope for precise alignment. To minimize the rf pickup on the dc electrodes, the trap is mounted in a filter board containing an 8 MHz lowpass RC filter for each of the 64 dc electrodes. The trap is connected to the filter board by wire bonds, and from there to the vacuum flange and electrical feedthrough by kapton insulated copper wires. Figure 3.1 shows pictures of the trap mounted in the filter board, and of the filter board mounted in the vacuum chamber. The design and fabrication process is described in more detail in [Kau17a].

A steel tube containing calcium granules is directed at the trap and heated to provide a constant stream of atoms, which can be ionized for trapping by turning on the photo-ionization lasers (Sec. 3.4). This *calcium oven* is continuously electrically heated by a current of 2.9 A, to prevent thermal drifts of the setup, and to obtain a stable background pressure.

All large unused surfaces on the trap chip and filter board are either grounded, or individually wired to be used as *compensation electrodes*. Ideally, the rf node coincides with the center of the dc potential. If this is not the case, the amplitude of the micromotion (Sec. 2.1) will increase, giving rise to impaired doppler cooling, decreased fluorescence on resonance, and other detrimental effects [Pos10]. The otherwise unused surfaces on the trap chip are used as compensation electrodes, and are typically set to -33 V. A global difference between upper and lower dc electrodes of typically $2 \times 0.12446 \text{ V}$ is used for additional micromotion compensation. As part of a regular calibration routine, the global difference is optimized by minimizing the amplitude of Rabi oscillations on a micromotion echo of one of the narrow $4S_{1/2} \leftrightarrow 3D_{5/2}$ carrier transitions.

Trap drive stabilization

The radial confinement (see Fig. 2.2) is mainly determined by the frequency and amplitude of the rf drive. Keeping it stable is essential for obtaining long motional coherence times and driving high-fidelity entangling gates. The first steps are stable generation, low noise amplification, and spectral filtering of the rf trap drive signal.

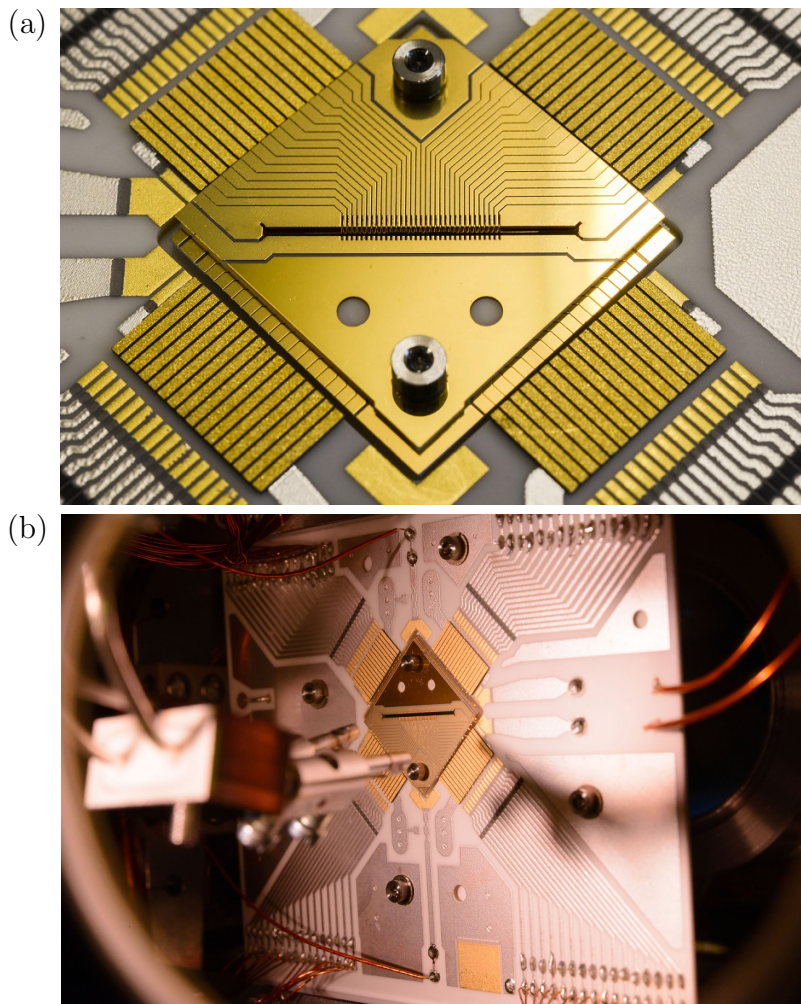


Figure 3.1: Pictures of the segmented ion trap, (a) mounted in the filter board, and (b) observed through a vacuum chamber window. The trap consists of two laser-machined and gold-coated 127 μm thick alumina wafers, which are spaced by 254 μm . This results in 32 pairs of individually controllable dc electrodes and interconnected rf electrodes, with a distance of 200 μm between neighboring electrode centers. The trap slit measures $12.84 \times 0.384 \text{ mm}^2$, including extended outer electrodes to reduce axial micromotion. Each of the dc electrodes is connected to an 8 MHz lowpass RC filter close to the trap, to minimize rf pickup at 33.48 MHz. All rf and dc connections are wire-bonded to the filter board, from where they are connected to the electrical vacuum feedthrough by kapton insulated copper wires. In the foreground of panel (b), the oven can be observed, which contains calcium granules. While ions are only trapped when the photo-ionization lasers are turned on, the oven is continuously heated to prevent thermal drifts and obtain a stable background pressure.

A DDS-based signal generator¹ generates a 33.48 MHz sine wave at -16 dBm. The signal is amplified by a water-cooled amplifier² and connected to a custom-made *helical resonator*. The function of the helical resonator is voltage transformation, filtering, and to prevent reflections by decoupling the high-impedance load of the trap and vacuum feedthrough from the 50Ω output impedance of the rf source. The design and fabrication is described in [Kes12]. All cables are kept as short and rigid as possible to improve passive stability. The helical resonator is mounted on top of the vacuum chamber (Sec. 3.2) and shielded by a silver-plated aluminum enclosure. The stability of a similar system was analyzed in [Dil14], and a strong correlation between temperature and rf output amplitude fluctuations was found. An active stabilization circuit was developed and also applied to this setup [Kau17a]. As shown in Fig. 3.2, a capacitive divider is used to probe about 1% of the output of the helical resonator. The probe signal is rectified and compared to a reference signal by a homemade PI controller, which is connected to the modulation input of the rf signal generator. An oscilloscope is used to monitor the feedback signal from the PI controller, and the capacitive divider output via a voltage probe³. The typical rf amplitude calculated from this probe measurement is $\sim 410 \text{ V}_{\text{pp}}$. In the course of this thesis, an attempt was made to replace the homemade PI controller with a fast commercial PI-regulator⁴. Ramsey spectroscopy [ROO08b] was used to measure motional coherence on all radial modes, and trap frequency drifts over a period of 60 minutes. However, no significant improvement could be measured, and the homemade circuit was retained.

¹ Rohde & Schwarz SMB100A.

² Mini-Circuits ZHL-5W-1+.

³ Tektronix P2220.

⁴ TEM Messtechnik NoiseEater 3V0.

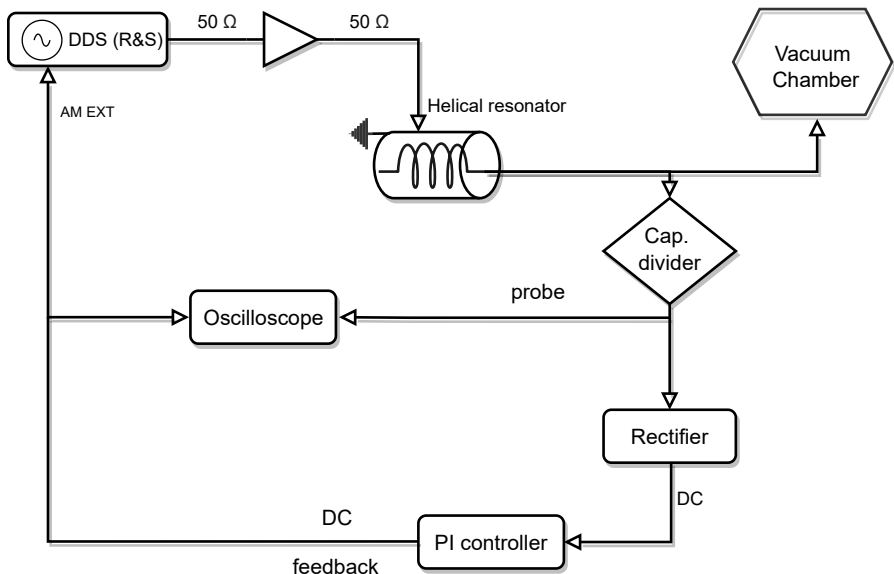


Figure 3.2: Active rf stabilization circuit. A DDS-based signal generator provides 33.48 MHz, which is amplified and connected to a helical resonator. The output is supplied to the trap and probed by a capacitive divider. A PI controller compares the rectified probe signal to a reference and regulates on the signal generator amplitude modulation input. The feedback signal and rf probe are observed on an oscilloscope. Details can be found in [Dil14, Kau17a].

Trap operations

In order to realize a fully reconfigurable qubit register as described in [Kie02], each of the 32 dc electrode pairs forms one segment, which can be supplied with an independent dynamical voltage. All lasers are focused on segment 19, known as the laser interaction zone (LIZ). These properties result in the following basic toolset of operations, illustrated in Figure 3.3. A detailed discussion can be found in [Hil22a].

Transport

A single trapping potential is typically created by supplying one segment with -6 V and grounding both neighboring segments. By dynamically adjusting the voltages on a set of two segments at a time, segment-wise transport of ion crystals is realized, with a typical transport time of 21 μ s per segment. Multiple crystals can be transported in parallel. For the work in this thesis, the optimized segment-wise voltage ramps were concatenated to form multi-segment transport sequences. A software implementation of fully optimized multi-crystal and multi-segment voltage ramps is under development. With the current implementation, axial mode excitation of 0.1 motional quanta per segment has been measured [Wal12]. An additional fall-off time of 50 μ s is included after every transport operation.

Separation and merge

Using the two neighboring segments on either side of a trap segment, ion crystals can be deterministically separated and merged. After a one-time calibration of the trap potentials, the procedure can be controlled by three parameters: a static potential tilt U_t , a voltage offset U_{CP} at the *critical point* - where the harmonic confinement by the external potential vanishes, and the total duration of the process t_{tot} [Rus14]. Typical values are $U_t = 41$ mV, $U_{CP} = 5\text{-}30$ mV, and $t_{tot} = 90$ μ s. Out of these, the static potential tilt is the most sensitive to daily drifts, and has a strong effect on the residual axial motional excitation. An automated ten-minute interval recalibration procedure has been implemented. Furthermore, empty potential wells are added to all shuttling sequences, to maintain electrostatic symmetry around the LIZ at the critical point. The merge operation is realized as a time-inverse separation. Thus far, these operations have only been performed at the LIZ, due to the required laser-driven calibration measurements. Remote calibration measurements have been conceived and are planned in the near future.

Laser-driven operations

All laser-driven operations described in Sec. 2.1 are executed at segment 19. The light-shift gate is performed on radial motional modes, to minimize the effect of axial excitation induced by transport operations. The 729 nm laser used for shelving is arranged perpendicular to the trap axis to minimize coupling to the axial motional modes, for the same reason.

Crystal rotation

By changing the voltages on the neighboring diagonal pairs of dc electrodes, ion crystals can be rotated, resulting in a physical ion swap around the center of the crystal. This operation has been performed with up to four-ion crystals, with minimal residual excitation, and on all trap segments [Kau17b, Kau19, Kau20]. For two ions it is equivalent to a logical laser-driven SWAP gate (Fig. 6.3), but a physical swap is preferred since it provides unit fidelity. Recently, the voltage ramps have been optimized for providing constant trap frequencies, to ensure that no motional excitation is transferred between different motional modes [Ort21]. This leaves only the duration as a free parameter, with a typical value of 60 μ s.

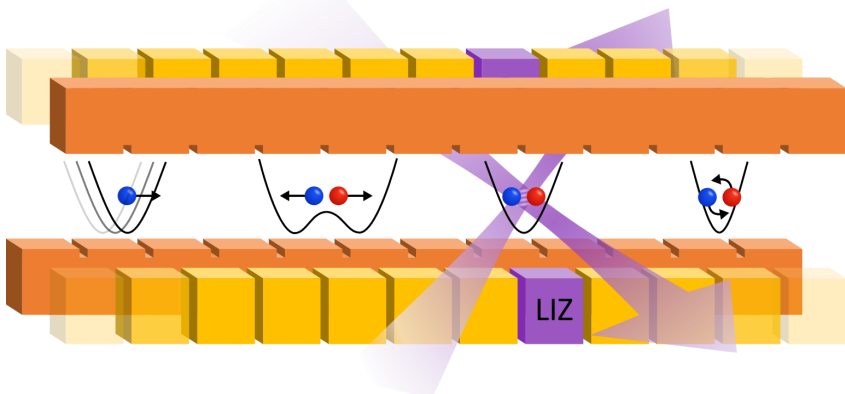


Figure 3.3: Schematic representation of all basic trap operations. From left to right: ion crystal transport, separation/merge, laser-driven operations at the laser interaction zone (LIZ), and rotation. Together, these operations constitute a fully reconfigurable and scalable qubit register. Figure taken from [Kau19].

3.2 Vacuum chamber and passively shielded quantizing magnetic field

The vacuum chamber, which is described in detail in [Kes12], provides a compact and robust trap enclosure, while minimizing the amount of magnetic parts in the vicinity of the trap. An ion pump, and an additional passive ion-gauge are mounted at a distance of 60 cm, and are keeping the pressure below 2×10^{-10} mbar. Six vacuum windows allow for horizontal optical access, with one window mounted in an inverted viewport, such that an imaging objective can be placed close to the trap. The assembly and bakeout procedures are described in [Kau17a].

Magnetic field sensitive qubits

The spin qubit in ${}^{40}\text{Ca}^+$ (see Fig. 2.1) is based on the Zeeman sublevels of the $4\text{S}_{1/2}$ ground state. A magnetic field of ~ 0.37 mT is required for the Zeeman splitting of the sublevels, and to provide a spin quantization axis. The stability of this external field is crucial, as any fluctuations directly affect the spin coherence, and shift the Raman transition lasers out of resonance. Ideally, the field is also homogeneous over the 6.4 mm wide range of the trap: any deviation leads to a shuttling-induced qubit phase ϕ according to

$$\phi = \int_{t_1}^{t_2} \Delta\omega_Z(x(t)) dt, \quad (3.1)$$

where $\Delta\omega_Z(x(t))$ is the difference in Zeeman splitting on the path $x(t)$, taken by an ion between two single qubit rotations at times t_1 and t_2 . These phases need to be corrected for, either by individual circuit calibration, or by calculation with the help of a measured magnetic field map [Kau17c, Kau17a, Kau19]. We combine a third-generation array of temperature-compensated permanent magnets with a μ -metal enclosure and an active compensation system to provide the required level of stability and homogeneity. What follows now is a short historical overview, with a specification of the latest generation permanent magnets. The μ -metal enclosure is briefly mentioned, and the active compensation system is discussed in Section 3.3. Figure 3.4 shows a complete layout of the apparatus.

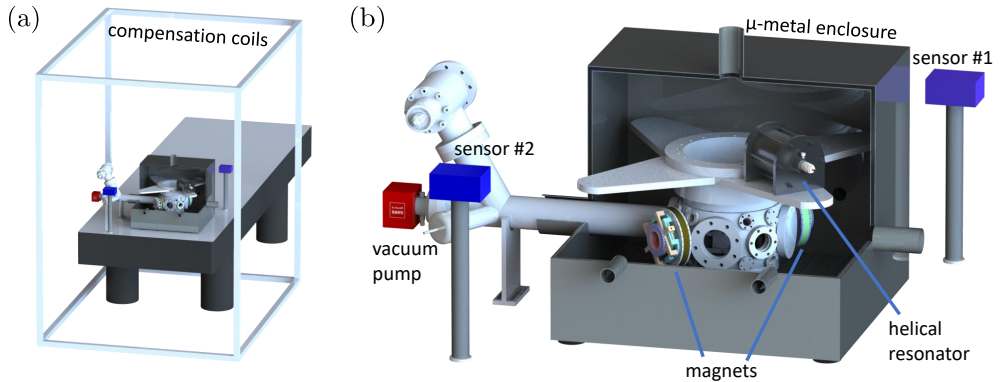


Figure 3.4: Overview of the complete apparatus. (a) Six magnetic field compensation coils are mounted around the entire setup. The dimensions were chosen to provide a relatively homogeneous field over the entire trap area. (b) Close-up, showing in particular the μ -metal enclosure, vacuum chamber, third generation permanent magnets, and magnetic field sensor packs. The vacuum pump is mounted outside the shielding enclosure to minimize the magnetic footprint. The sensor packs are mounted on the quantizing magnetic field axis. One upper half of the μ -metal enclosure is not shown.

Previous magnet iterations

Initially, two current-stabilized electromagnetic coils mounted in a near-Helmholtz configuration were used for generation of the quantizing magnetic field [War15, Rus17a]. They were replaced by the first generation of permanent magnets, consisting of 80 cylindrical $\text{Sm}_2\text{Co}_{17}$ magnets mounted in two aluminum rings on top of the inactive coils [Rus17a]. This change from active noisy heat-generating coils to passive magnets, combined with the shielding μ -metal enclosure, resulted in a qubit spin-echo coherence time increase from 45(3) ms to 2.1(1) seconds [Rus16]. However, even though the $\text{Sm}_2\text{Co}_{17}$ magnets have a low temperature dependence, temperature-induced magnetic field drifts were still significant, and a considerable nonlinear magnetic field gradient was measured [Rus17b]. The second generation made use of additional NdFeB magnets to counter the temperature-induced drifts, and employed a different geometry for greater mechanical stability. The temperature dependence was decreased by a factor 6, but a much larger field gradient was measured - possibly due to magnetization of the vacuum chamber [Nic17, Kau19].

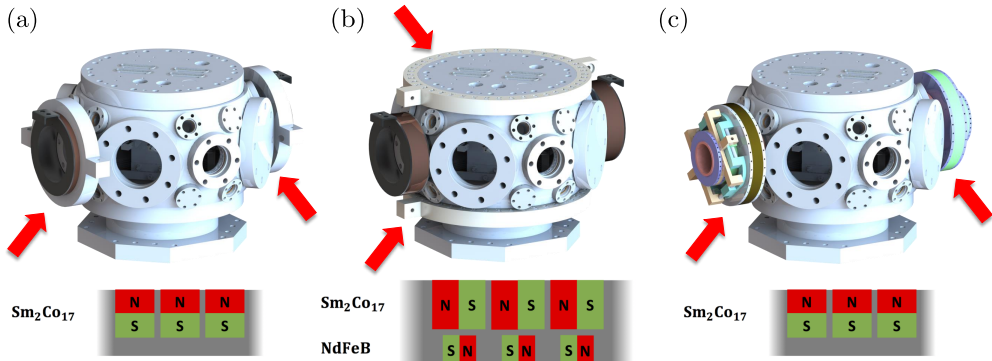


Figure 3.5: Iterations of magnetic field generating coils/magnets. (a) The first iteration of 80 $\text{Sm}_2\text{Co}_{17}$ magnets was mounted in aluminum rings on top of the original field-generating coils. (b) The next version, which employed additional NdFeB magnets to counter temperature-induced drifts, was mounted on the top and bottom flanges for greater mechanical stability. (c) The third generation of more stable $\text{Sm}_2\text{Co}_{17}$ magnets is mounted in place of the coils, in a near-Helmholtz configuration. A special tuning mechanism is shown on the left magnet rings. Details for all iterations can be found in [War15, Rus17a, Nic17, Kau19].

Present magnetic field generation and shielding

The third generation features a temperature-compensated version⁵ of the $\text{Sm}_2\text{Co}_{17}$ magnets, with a Reversible Temperature Coefficient (RTC) of $-0.001\text{ }^{\circ}\text{C}$ and a residual induction of 0.83 T. On each side of the vacuum chamber, one main ring and two additional rings with opposing magnets are mounted. By changing the position of the outermost ring using an included non-magnetic tuning mechanism, the magnitude and homogeneity of the total field can be tuned. A schematic layout of the magnets and a simulation of the resulting field are shown in Figure 3.6. The magnet rings are mounted on the flanges that used to hold the electromagnetic coils (see Fig. 3.5). Design, fabrication, and testing was carried out in collaboration with Andreas Conta, Björn Lekitsch, and Janine Hilder.

After installation, the magnetic field in the trap was measured using a Ramsey-type measurement that determines the accumulated phase after shuttling an ion to each of the trap segments [Rus17b]. The resulting magnetic field map is compared to previous generations in Figure 3.7. A Zeeman-splitting of 10.664 MHz and an inhomogeneity

⁵ Electron Energy EEC2:17-TC16.

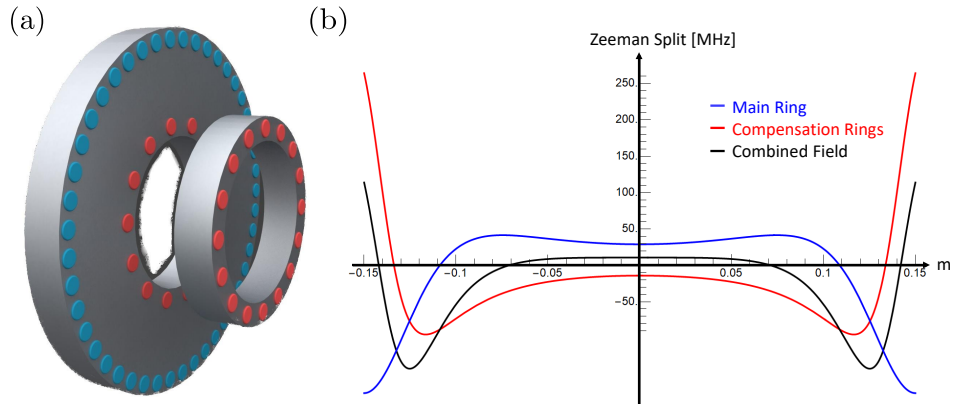


Figure 3.6: Third and present generation of permanent magnets. (a) 45 cylindrical $\text{Sm}_2\text{Co}_{17}$ magnets (blue) with a diameter of 6 mm and a height of 14 mm provide the main magnetic field. The magnets are mounted in an aluminum ring. Two additional smaller rings (red), containing 10 and 12 opposing magnets, are used to tune the magnitude and homogeneity of the combined field. The position of the outer ring can be adjusted using a specially designed non-magnetic brass tuning mechanism (not shown in this layout). (b) Simulation of the effective Zeeman splitting along the trap axis, resulting from two series of rings shown in (a), mounted on opposite vacuum chamber flanges.

well below 1 kHz were repeatedly found. A year later, measurements indicated that the inhomogeneity of the field had significantly increased. This may again be explained by magnetization of the vacuum chamber. Mechanical settling after repeatedly opening and closing the μ -metal enclosure may also have contributed (see Fig. 3.7). An attempt was made to restore the field by adjusting the outer ring positions, but the tuning range proved insufficient. The center of the homogeneous field was no longer overlapping with the center of the trap. Additional magnets were taped to several of the rings, until the field gradient was centered again. See Figure 3.7 for a comparison of magnetic field maps before and after adjustments, and the change due to opening part of the μ -metal enclosure. Ideas for future iterations are to use piezo-driven motors for precise tuning, and water cooling to stabilize the temperature of the magnets. Furthermore, simulations in COMSOL have shown that a Halbach configuration is more favorable for an optimal field homogeneity.

As shown in Figure 3.4, the vacuum chamber and surrounding optics are magnetically shielded by a μ -metal⁶ enclosure, consisting of two 2 mm thick sheets of μ -metal, spaced by 6 mm aluminum. In order to guide magnetic field lines around any openings, the

⁶ An alloy of 80% Ni and 20% Fe, with a magnetic permeability of 80 000 at 50 Hz.

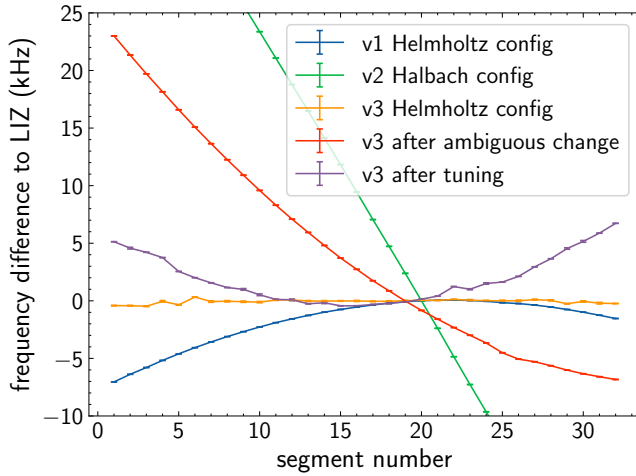


Figure 3.7: Magnetic field map of all trap segments, for different permanent magnet iterations. The field is measured by shuttling an ion to the indicated segment and calculating the accumulated phase upon return [Rus17b]. The third iteration endured an ambiguous change in homogeneity, which was partially compensated by tuning the outer rings and attaching additional magnets.

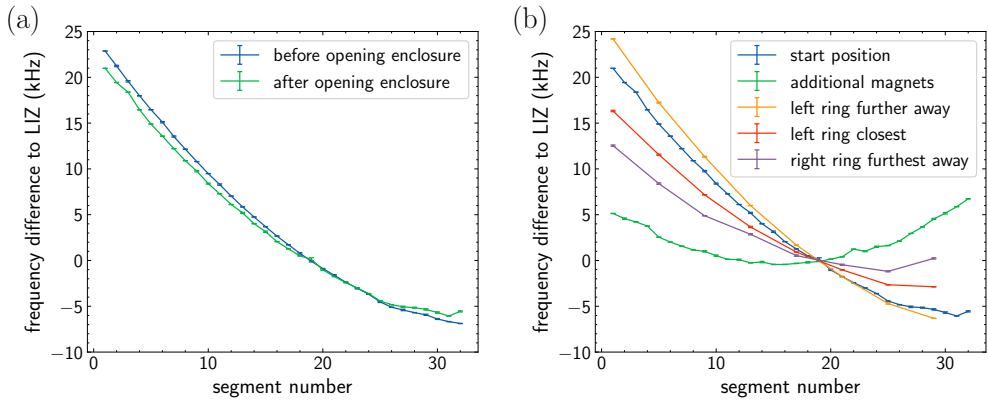


Figure 3.8: Magnetic field maps of all segments after the increase of inhomogeneity. (a) A small change was measured due to partly opening the μ -metal enclosure. Repeated opening of the entire μ -metal enclosure may have contributed to the large shift. (b) Tuning the field by changing the position of the outer rings and attaching additional magnets.

design features 10 cm long sleeves for feedthroughs of fibers and electrical signals, and 1 cm overlapping edges between the bottom and top parts. As simulations were not available at the time, the design was based on experience⁷, and was aimed at shielding factors of >100 for frequencies of 50 and 100 Hz [War15]. Shielding factors of 20-30 dB for frequencies of 500 Hz-100 kHz were measured by Kesser [Kes12], and about a factor 25 was measured for magnetic field drifts on the timescale of minutes. Recent simulations in COMSOL revealed that a significantly higher overlap and distance between the μ -metal layers is required for a high shielding factor at low frequencies. A newly constructed enclosure for another setup employs three layers of μ -metal at a spacing of about 4.5 and 7.5 cm to reach a shielding factor of ~ 25000 .

3.3 Active magnetic field stabilization

High frequency noise is successfully mitigated by the μ -metal enclosure. However, the low-frequency attenuation factor of 25 proved insufficient to shield the experiment from external magnetic field changes. In particular, one experiment in the same building was generating fully automated and randomly scheduled ramps between -11 and +11 T at a rate of up to 0.5 T/min. This was harmful for the following reasons: First, a constant offset in Zeeman splitting of the qubit states leads to miscalibrated laser frequencies and thereby to faulty operations. An automated interleaved tracking- and recalibration procedure was implemented [Kau17c], but resulted in too much measurement overhead at the given rate of change. Second, a Zeeman splitting drift during a single measurement leads to phase instability. For the experiments discussed in [Hil22b], qubit superposition states need to be maintained throughout a sequence duration of 15 ms. Assuming that a qubit phase accumulation of $\Delta\phi \leq 0.05\pi$ is sufficient for obtaining the required contrast in these measurements, and using Eq. 3.1 with constant position, we require a maximum Zeeman splitting drift of $\frac{\Delta\omega_Z(t_2) - \Delta\omega_Z(t_1)}{t_2 - t_1} \approx 2\pi \times 113 \text{ Hz/s}$. With $\Delta\omega_Z = g_S \mu_B B / \hbar$ and 25x attenuation, this translates to $\frac{\Delta B}{\Delta t} \approx 100 \text{ nT/s}$ outside the μ -metal enclosure. To approach this level of stability, an active regulation system was devised.

Two 3D fluxgate sensor packs⁸ are mounted on the quantizing magnetic field axis, outside the μ -metal enclosure, at a distance of ~ 60 cm from the center of the trap. The sensors are not placed directly next to the μ -metal enclosure to avoid measuring

⁷ Collaboration with Sekels GmbH, Ober-Mörlen, Germany.

⁸ One pack of 3xFL1-20 and one pack of 3xFL1-200, by Stefan Mayer Instruments. The fluxgate sensors are mounted orthogonally in a 3D printed non-magnetic polylactide enclosure.

a higher field density, as the magnetic field lines are bending around the enclosure. Placing the sensors and coils outside the shielding enclosure is helpful, as it effectively increases the resolution of the stabilization, and because the enclosure acts as a filter for field inhomogeneity and current supply noise from the coils. See Figure 3.4 for a mechanical layout, and Figure 3.9 for an electrical layout. Each sensor pack is connected to a 24 bit analog-to-digital-converter (ADC) evaluation board⁹, which is controlled by a Raspberry Pi over a serial-peripheral-interface (SPI). The ADC has a least-significant-bit (LSB) step of $1.2 \mu\text{V}$, with optional 50 Hz filtering, and a three-channel output rate up to $\sim 10 \text{ kHz}$. Both sensor packs, consisting of either $3 \times \text{FL1-20}$ or $3 \times \text{FL1-200}$ sensors, have a noise level of $< 20 \text{ pT}/\sqrt{\text{Hz}}$ at 1 Hz. The analog outputs are $0.5 \text{ V}/\mu\text{T}$ and $0.05 \text{ V}/\mu\text{T}$, respectively. At a readout rate of 20 samples per second, reading out all three axes sequentially, the resolution of both sensor packs is noise-limited to 52 pT. Stable power supplies¹⁰ provide $\pm 12/16 \text{ V}$ for the sensors, and $+5 \text{ V}$ for the ADC. The sensor data is read out via SPI and made accessible to any client by a TCP server. Thus, two Raspberry Pis are continuously providing the sensor data, while one master Raspberry Pi is processing the data from both sensor packs in a PID regulation and controlling six coils via three current supplies¹¹. The regulation frequency is typically 2 Hz, and is limited to 10 Hz by the USB communication to the current supplies.

The coils were designed to maximize field homogeneity in an area of $\sim 1 \text{ m}^3$ around the trap, while taking into account the existing space constraints in the lab. Consisting of 32 windings of stranded copper wire¹², the coils are mounted in three square Helmholtz configurations, with total dimensions $2.45 \times 1.85 \times 2.5 \text{ m}^3$. At the recommended maximum current for the chosen wire, the magnetic field change near the trap is $\Delta \vec{B}_{\text{coils}}^{(\text{max})} = (9.41, 8.35, 0.78) \mu\text{T}$ as measured on the sensors, which corresponds to a qubit Zeeman splitting change of $\Delta \omega_z^{(\text{max})} \approx 2\pi \times 3.4 \text{ kHz}$.

⁹ Analog Devices EVAL-AD4112.

¹⁰ Statron 6371 and Keysight E3648A, running on a battery to minimize 50 Hz noise.

¹¹ Keysight E3648A.

¹² Four layers of Lappkabel DB 49900045DE.

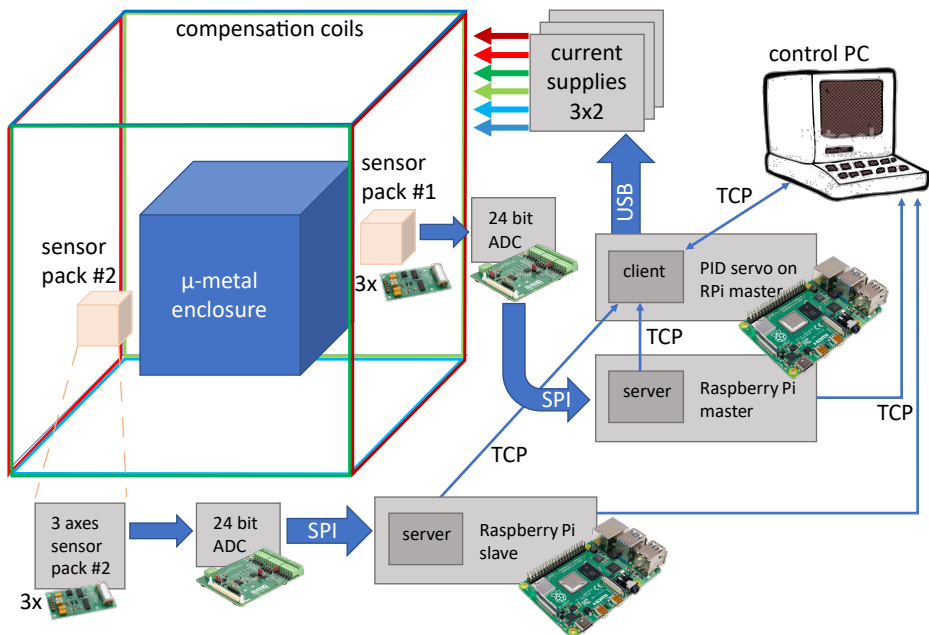


Figure 3.9: Electrical layout for the active magnetic field stabilization system. Two 3D sensor packs are each connected to a Raspberry Pi via an ADC. The readings are communicated over SPI and made available by a TCP server. The master Raspberry Pi also runs a PID servo that reads the sensor data via a TCP client and acts on 6 current supplies via USB. The current supplies are connected to the compensation coils. The PID servo can be remotely controlled, and the TCP server data can be logged from any computer.

Initially, error values were computed with individual setpoints for each sensor, and the error values for both sensor packs were added together in each of three independent PID regulations for the x, y, z axes. However, no setpoints could be found where the sensors were not working against each other. A single sensor pack regulation provided the best stabilization, and is illustrated by a qubit transition frequency tracking measurement in Figure 3.10a. During a 22 T magnetic field ramp of an experiment three floors below the quantum processor, the qubit transition frequency drift is reduced from 1350 Hz to ~ 110 Hz, and is comparable to the drift induced by magnet temperature changes.

To further improve the stabilization, a *control matrix* was measured, which describes the response of sensor values as a function of coil currents. An example is shown in table 3.1. Each of these numbers gives a change in μT on one of the sensors as a consequence of a 1 A current change on one of the coils. Further details are described in [Ort21], and are briefly summarized here. The measurements indicated that there was a significant coupling between the x and y axes of the sensors and coils, which could lead to interference between PID regulations. Additional measurements of each coil's effect on the qubit frequency showed a factor 100 difference between the x/y and z coils, due to the quantization axis pointing in the x/y direction. Therefore the z axis can be neglected. Using the control matrix for the x and y axes, current control vectors can be calculated that each only affect a single sensor value. With these current control vectors, four PID regulations can be operated independently without affecting each other. Note that the coils are now controlled individually instead of in Helmholtz configuration. Figure 3.10b shows the remaining qubit transition frequency drift of ~ 80 Hz during a similar external magnetic field ramp. While a magnetic field drift of ~ 26 nT can still be seen on the z axis sensors, this should not affect the qubit transition frequency according to the earlier described control matrix measurements. The remaining transition frequency drift can be explained by a field bending effect of the μ -metal enclosure. However, as the bending effect is direction-dependent, any significant drift source would have to be characterized individually. According to the calculation at the start of this section, the present stabilization is sufficient for the purpose of this work.

$\mu\text{T}/\text{A}$	coil x_1	coil x_2	coil y_1	coil y_2
sensor 1 x	-169.2	-68.7	29.2	76.4
sensor 2 x	62.2	-32.6	-87.6	-248
sensor 1 y	-45.1	21.4	-174.3	-69.2
sensor 2 y	-87.9	-183.7	49.6	1.7

Table 3.1: Control matrix describing fluxgate sensor responses as a function of stabilization coil currents. The z axis coils and sensors are not included, as measurements showed a very weak coupling to the qubit transition frequency.

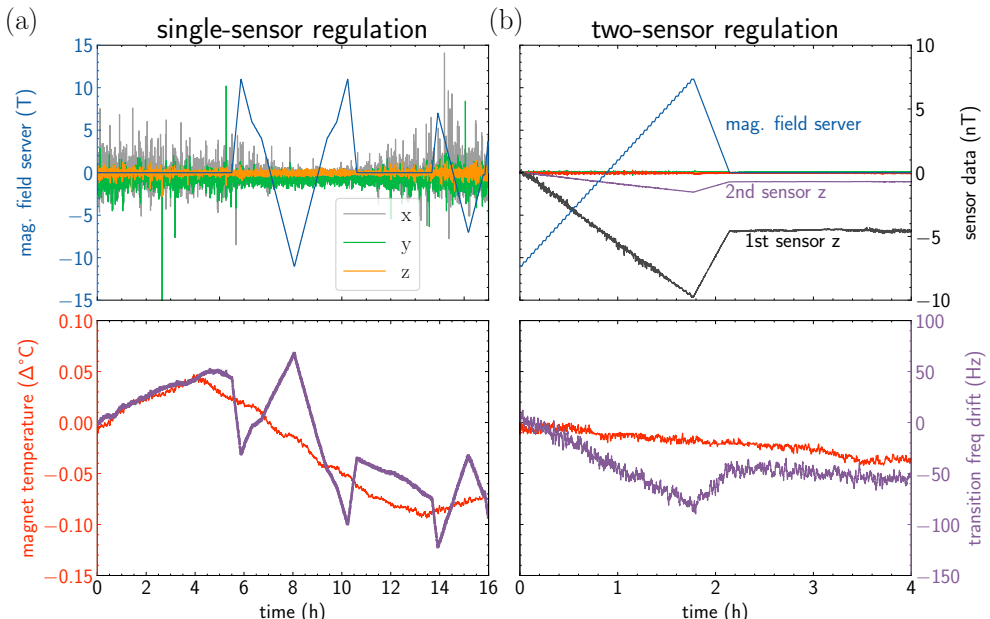


Figure 3.10: Qubit frequency drift measurements. (a) Single-sensor regulation on x, y, z axes. (b) Two-sensor regulation on x, y axes. Magnetic field ramps of an experiment three floors below the quantum processor were communicated via a TCP magfieldserver. The qubit frequency tracking measurement in (b) was performed at $\frac{1}{30}$ th of the accuracy of (a), and a running average was computed.

3.4 Laser light sources for ion loading and qubit operations

The operations described in Section 2.1 are driven by seven diode laser systems, mounted on an optical table outside the μ -metal enclosure. Mechanical shutters and acousto-optical modulators (AOMs) provide intensity, frequency, and phase control, after which the light is guided to the experiment by single-mode optical fibers. Inside the μ -metal enclosure, the beams are focused onto the laser interaction zone from five different directions, depending on the desired interaction. See Figure 3.11 for an overview of the beam configuration. A detailed description of the beam-focusing and polarizing optics inside the enclosure can be found in [Rus17a], with the following highlights: The optics are mounted in cage systems¹³ for stability and compactness. A fraction of each beam is split off and monitored by a photodiode¹⁴, and the fine-alignment of the beams can be remotely adjusted with the help of piezo-controlled mirror holders¹⁵. Typical beam parameters are also listed in [Rus17a]. Here we only discuss the main characteristics and purpose of each laser.

¹³ Thorlabs GmbH

¹⁴ Thorlabs SM05PD1A

¹⁵ Picomotor, Newport GmbH

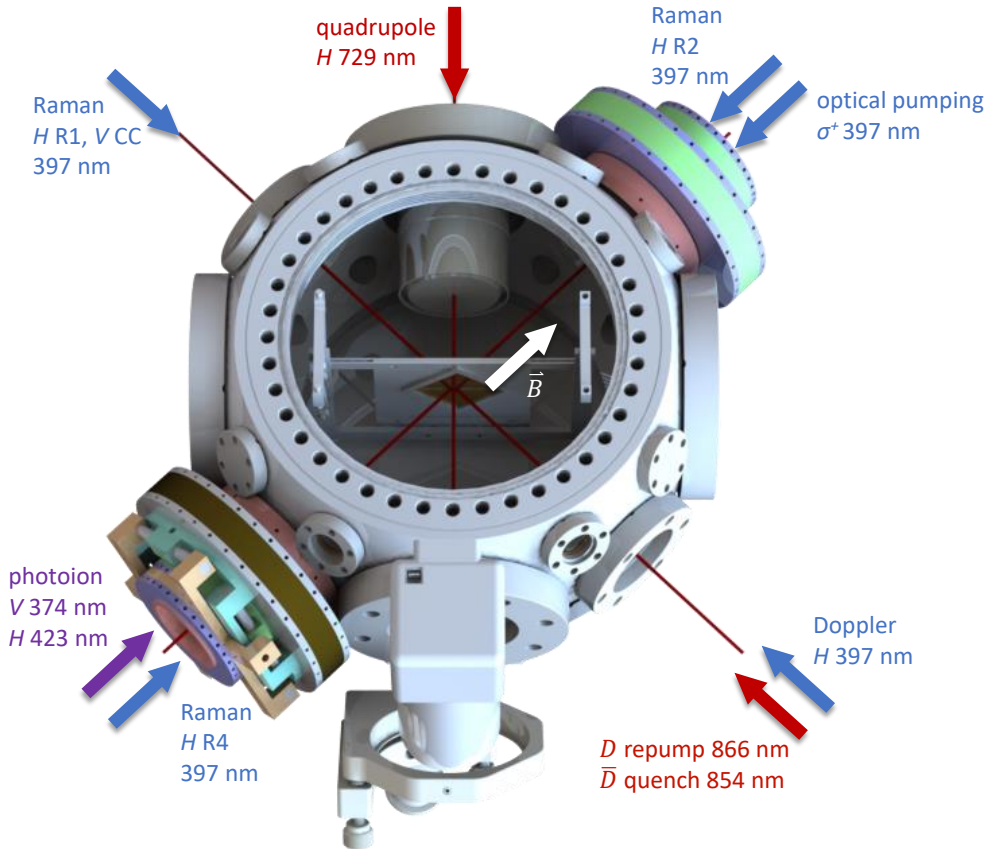


Figure 3.11: Top-down view of the vacuum chamber to illustrate the laser beam configuration. The polarizations are labelled: horizontal (H), vertical (V), diagonal (D), anti-diagonal (\bar{D}), and right circular (σ^+). The inverted viewport at the top allows for placing a high-NA objective relatively close to the trap, outside the vacuum. The trap is mounted on a filterboard, described in detail in [Kau17a]. The electrical feedthroughs are mounted in the top flange (not visible here). A laser alignment camera is mounted at the front (bottom) vacuum window. Details about the optics mounted around the vacuum chamber can be found in [Rus17a].

Ionization, trapping & cooling, optical pumping

Ionization is a two-step process (see Fig. 2.1) and is performed by two diode lasers¹⁶. The first laser is regulated to 423.791 nm based on a wavemeter reading¹⁷, and the second laser is free-running around 374 nm. The lasers are combined on a polarizing beam splitter and sent through the same fiber, after which they are incident on the trap at a 90° angle to the atomic vapor beam from the calcium oven. The oven is continuously running, to provide fast trapping, and to keep the current-induced magnetic field constant. The ionization lasers are switched on using shutters¹⁸.

Another diode laser¹⁹, locked to 396.959 nm on a low-finesse cavity via the Pound-Drever-Hall technique [Bla01], is split in three branches, each containing an AOM for frequency and intensity control. The first branch is shifted by $-2\pi \times 110$ MHz, and used for initial trapping and recrystallizing hot ions. The second branch is shifted by $+2\pi \times 216$ MHz, which brings it to about half the natural linewidth from the $4S_{1/2} \leftrightarrow 4P_{1/2}$ transition. This branch is used for Doppler cooling at the start of each experimental run, and, with the frequency tuned close to resonance, for fluorescence detection. The first two branches are combined and sent to the experiment through the same optical fiber. At the experiment side, the less detuned beam is horizontally polarized to eliminate any circular components. This way, the driven subtransitions are closer together, decreasing the effective linewidth of the cooling transition, and therefore leading to a lower Doppler temperature. The third branch is tuned to the same frequency as the second branch and used for optical pumping, after being transported through a separate fiber. The polarization is changed to σ^+ on the experiment side, such that only the $\Delta m_J = +1$ transition is driven. The lasers are switched and frequency- or amplitude-modulated by adjusting the rf signal supplying the AOMs. The signals are generated by voltage controlled oscillators²⁰ (VCOs), amplitude-modulated by variable attenuators²¹, and amplified²² to ~ 2 W.

A diode laser²³ at 866.451 nm is included to pump any ions that have decayed to the $3D_{3/2}$ state back into the cooling or detection cycle. This laser is also locked on

¹⁶ DL Pro, Toptica Photonics AG

¹⁷ HighFinesse WSU-30, accuracy 1.0 pm.

¹⁸ Self-built from SC 4.7 ND, Visaton GmbH

¹⁹ DL Pro, Toptica Photonics AG

²⁰ Mini-Circuits ZOS-150

²¹ Mini-Circuits ZX73-2500+

²² Mini-Circuits ZHL-5W-1

²³ DL Pro, Toptica Photonics AG

a low-finesse cavity via the Pound-Drever-Hall technique, as well as frequency- and amplitude-controlled using an AOM. The polarization is diagonal, to enable driving of $\Delta m_J = 0, \pm 1$ transitions.

Qubit operations

Raman transitions between the $4S_{1/2}$ ground states (see Fig. 2.1) are driven by a frequency-doubled diode laser²⁴ close to 397 nm. The SHG cavity is locked to the fundamental infrared laser via the PDH-technique, resulting in a UV linewidth of < 500 kHz, and slow drifts of ~ 0.3 GHz/day. These drifts are insignificant compared to the $4S_{1/2} \leftrightarrow 4P_{1/2}$ detuning of $\Delta \approx 2\pi \times 1$ THz. The laser is intensity-stabilized, and distributed over four beams, which can each be individually frequency-, amplitude-, and phase-controlled using an AOM. Here, the frequency difference stability is important, since it has to be resonant with the Raman transition between the two $4S_{1/2}$ states. See Appendix A for a detailed description of the intensity stabilization circuit and the beam distribution setup. After distribution, the four beams are coupled into three fibers²⁵, and guided into the μ -metal enclosure. There, the beams are focused on the laser interaction zone from three directions (see Fig. 3.11), and are used pairwise for different operations: Beams R1 and CC are mutually orthogonal linearly polarized, have no resultant k -vector, and propagate perpendicular to the quantizing magnetic field. Therefore, these beams can drive $\Delta m_J = 0, \pm 1$ transitions, and do not couple to motional states, i.e. there are no sidebands. R1 and CC are used for coherent single qubit operations. R4 can be combined with either R1 or CC to couple to the radial motional modes. Similarly, R2 can be combined with R1 or CC to couple to axial motional modes. Due to the polarization and the direction of the magnetic field, the combination with R1 can drive $\Delta m_J = 0, \pm 1$ transitions, and the combination with CC can only drive motional excitation. Therefore, either R4 or R2 is coupled with R1 for sideband cooling and probing of motional excitation of the desired radial or axial mode. R4 is coupled with CC to provide the mutually orthogonal linearly polarized beams that can drive radial two-qubit gates (see Sec. 2.2). Directly after the fiber outputs in the μ -metal enclosure, the polarization of the beams is either rotated or filtered to achieve a high purity (see [Rus17a] for details). Fine alignment of the beams can be remotely adjusted using piezo-controlled mirror holders.

²⁴ TA-SHG Pro, Toptica Photonics AG

²⁵ PMC-E-400Si-2.3-NA014-3-APC.EC/OPC, Schäfter + Kirchhoff GmbH

Qubit state initialization & readout

Quadrupole transitions $4S_{1/2} \leftrightarrow 3D_{5/2}$ are driven using a 729 nm diode laser²⁶, which is locked via the PDH-technique to a high-finesse Fabry-Pérot cavity²⁷, resulting in an estimated linewidth of ~ 100 Hz [Mac12]. See Appendix B for an overview of the locking setup. Frequency-, amplitude-, and phase control is provided by a double pass AOM. After being guided close to the μ -metal enclosure by a fiber, the beam enters the enclosure via free-space and is focused onto the LIZ at a 90° angle to the trap axis, to avoid coupling to axial motion, which may be induced by shuttling. This way, the shelving operation can still be performed with high fidelity after a long shuttling sequence. The beam is horizontally polarized such that it only couples to $\Delta m_J = 0, \pm 2$ transitions, minimizing errors due to off-resonant excitation. Ion-fluorescence after decay from the $4P_{1/2}$ state is captured along the same beam path in the opposite direction: after exiting the μ -metal enclosure, a dichroic mirror separates the 729 nm light from the 397 nm fluorescent light. The image is magnified and focused on an EMCCD camera²⁸ and a photomultiplier tube²⁹ (PMT) in a ratio of 0.1:0.9. The camera is used for alignment and monitoring, while the PMT is used for detection. See [Rus17a] for more details about the imaging system.

As the $3D_{5/2}$ state has a lifetime of 1.17 s, an 854 nm diode laser³⁰ is included to ‘quench’ the ion back into the $4P_{3/2}$ state, from where it will quickly decay to the ground state. This laser is wavemeter-regulated to 854.4437 nm, and is transported into the μ -metal enclosure by the same fiber as the 866 nm laser. The polarization is anti-diagonal, such that it couples to all $3D_{5/2}$ substates.

3.5 Experimental control infrastructure

Experimental sequences, in particular the voltages on the dc trap electrodes and the switching of laser pulses, need to be precisely timed on a microsecond to nanosecond timescale. Toward this end, the heart of the control structure, shown in Fig. 3.12, is jointly formed by a control PC and a multichannel arbitrary waveform generator (mAWG). The mAWG is based on a custom programmed FPGA, and is described

²⁶ TA Pro, Toptica Photonics AG

²⁷ ATF 6020 notched cavity, Stable Laser Systems

²⁸ Andor iXon, Model No. DV860DCS-UVB

²⁹ Photon counting head H10682-210, Hamamatsu Photonics K.K.

³⁰ DL 100, Toptica Photonics AG

in detail in [Kau19, Kau20]. It features 80 analog output channels that provide the trap electrode voltages, and 24 TTL outputs which are mainly used for switching laser pulses, and as device triggers. The analog outputs can be varied between ± 40 V, with a resolution of 1.2 mV, an update time of 360 ns, and a slew rate of ~ 20 V/ μ s. Additional to the in-vacuum filters discussed in Sec. 3.1, two stages of lowpass filters with a cut-off frequency of 100 kHz are employed, one at the output of the mAWG, and one at the vacuum feedthrough. Switching of laser pulses is done by composing the rf pulses that drive the AOMs, either by triggering shaped rf pulses on a DDS-based versatile frequency generator³¹ (VFG), or by switching³² the continuous rf supply of a number of voltage controlled oscillators³³ and a DDS³⁴, with a time resolution of 20 ns. A typical experimental sequence, sketched in Figure 3.13a, proceeds as follows: The control PC generates device instruction data based on the current user interface parameters and the programmed experiment. A pulse list is sent to the VFG over USB, and the rest of the sequence data is sent to the mAWG over ethernet. The control PC then requests the mAWG for the repeated execution of the sequence for a number of *countcycles*. The mAWG varies the voltages on the dc trap electrodes, and sends TTL signals to switch laser pulses, trigger preprogrammed pulses on the VFG, and trigger the PMT counter. In the meantime, an evaluation process on the control PC is waiting for the PMT counts. Upon arrival, the results are evaluated and plotted, after which the next sequence is sent by the control PC. In this case, one sequence represents one datapoint. Statistics depend on the number of countcycles per point, which typically ranges from 10-200. Optionally, before and after every datapoint, a standardized measurement termed *postselection* confirms that the ion(s) are still trapped, by performing a detection with the 854 nm laser enabled. Any population in the $3D_{5/2}$ state is then returned to the $4S_{1/2} \leftrightarrow 4P_{1/2}$ detection cycle. If required, the individual countcycles can be synchronized with an external 50 Hz AC line trigger, to filter out related noise. One countcycle or shot consists of the timed electrode voltages and laser TTLs that make up the particular experiment, and is often built together from standard components: Doppler cooling, sideband cooling, shelving, detection, and custom (multi-crystal) postselection. As an example, the pulse sequence for probing motional excitation is shown in Figure 3.13b.

³¹ VFG-150, Toptica Photonics AG

³² Mini-Circuits ZYSW-2-50DR

³³ Mini-Circuits ZOS-150

³⁴ Rohde & Schwarz SML01

Besides orchestrating experimental sequences, the control PC is used for various logging and calibration procedures that are less time-critical. Connections are made via ethernet, USB, and multifunction analog and digital I/O devices³⁵. The involved components and connections are shown in Figure 3.12.

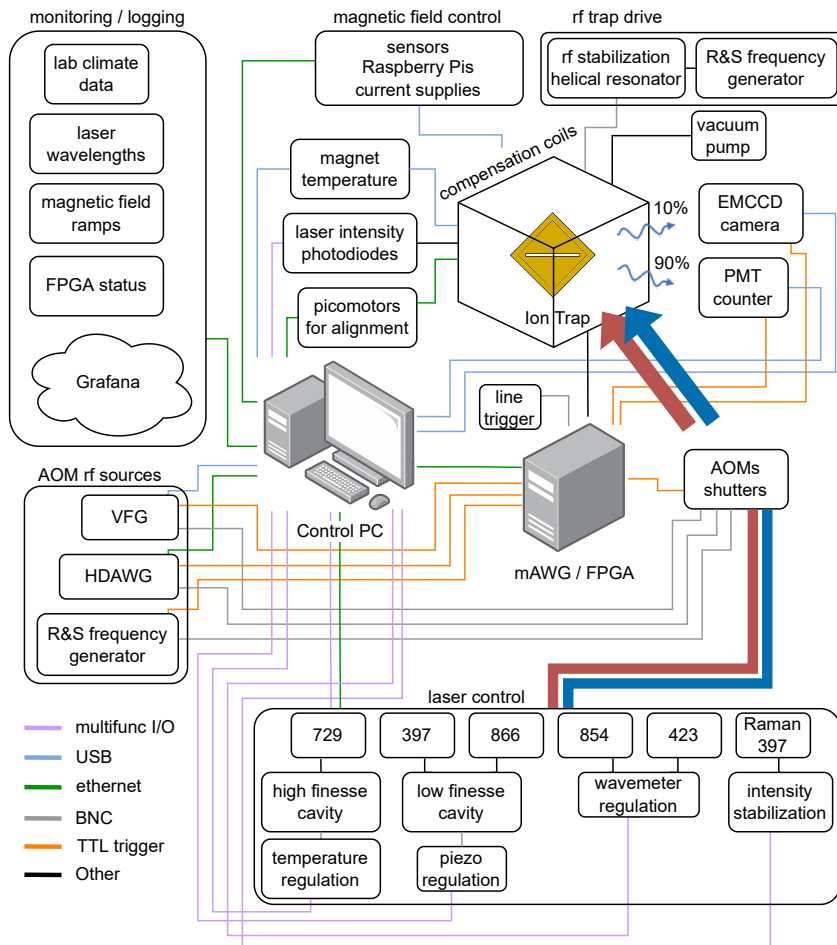


Figure 3.12: Overview of major components of the control infrastructure. The connections are color coded by type. The red and blue lines represent UV to infrared laser light transported by various fibers. The wiggly arrows represent fluorescent light for detection, guided to the PMT counter and EMCCD camera in a ratio of 0.9:0.1.

³⁵ National Instruments USB-6000 & USB-6008

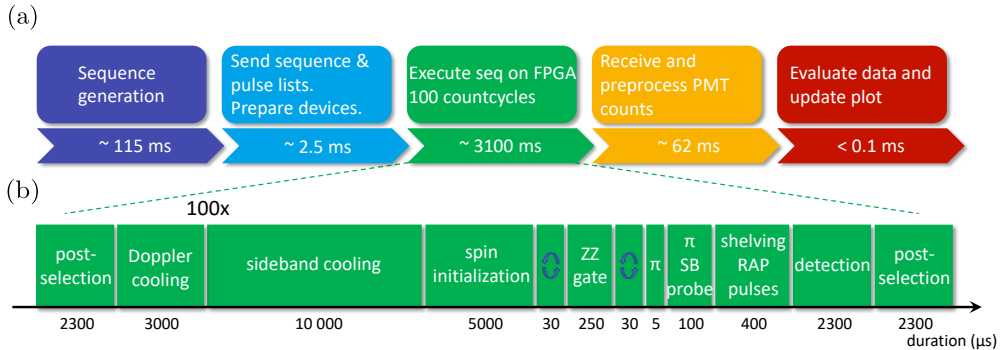


Figure 3.13: (a) Approximate timings for communication and execution of an experimental sequence for a single datapoint. Note that the timings are averaged and that some device communication is performed in parallel. (b) Example pulse sequence for one shot of motional excitation probing. Electrode voltages are not shown, as they are mostly constant for this particular experiment. This sequence performs the circuit shown in Fig. 2.10 for an even spin state, including spin-echo spinflip. The detection/postselection time is the total time required for splitting a two-ion crystal and detecting the ions individually, with a PMT exposure time of 800 μ s.

To provide all this functionality, a considerable collection of mainly C++ libraries and a user interface were built in the years before and during the work for this thesis. An extensive description can be found in [Hil22a]. In addition to implementing the calibrations and experiments described in this thesis, contributions were made to the following elements:

- Live interactive 2D color plotting.
- Automated ion loading with a far-detuned (re)crystallization beam, assisted by image recognition using a neural network.
- Code structure for inserting characterization measurements at predefined breakpoints in long shuttling sequences, e.g. to probe motional excitation or finely calibrate two-qubit gate parameters.
- Integration of an advanced multichannel AWG³⁶ for long-term replacement of the VFG, toward enabling shaped pulses on both Raman beams for high fidelity gates.
- Interleaved tracking and optional recalibration of transition frequencies, secular frequencies, readout fidelity, laser intensities, ion loss rates, and crystal separation parameters.

³⁶ HDAWG, Zurich Instruments AG

- Fully automated concatenated execution and evaluation of calibration procedures, which can be run at a specified time interval, or interleaved with measurements.
- Remote control and monitoring of all important devices, to enable remote measurement sessions.
- TCP communication between the control PC, the wavemeter, and the piezo control of the cavity which is used for stabilizing the 397 nm and 866 nm lasers. This enabled pausing measurements based on wavemeter readings, and compensating the cavity length for temperature drifts.
- Integration of magnetic field sensor logging and coil control, for the functionality described in Sec. 3.3.
- Logging of all laser wavelengths in a remote database, visualized by Grafana³⁷.

³⁷ <https://www.grafana.com>

Chapter 4

Theory of Passivity-Based Inequalities

This chapter introduces the theoretical frameworks for global passivity [Uzd18b] and passivity deformation [Uzd21]. We start with the evolution of a closed system in a thermal state, under influence of an external - possibly noisy - control field (see Fig. 4.1). Such a system is governed by the second law of thermodynamics, and by the equivalent Clausius inequality. Then we introduce the concept of passivity and show how it restricts the evolution of such a system in a similar way. However, it also holds for a system and environment which are initially correlated, and it can be used to provide stricter bounds. Finally we introduce passivity deformation, which can provide even stricter bounds, and can also be used in the ultracold limit, i.e. for non-thermal initial states.

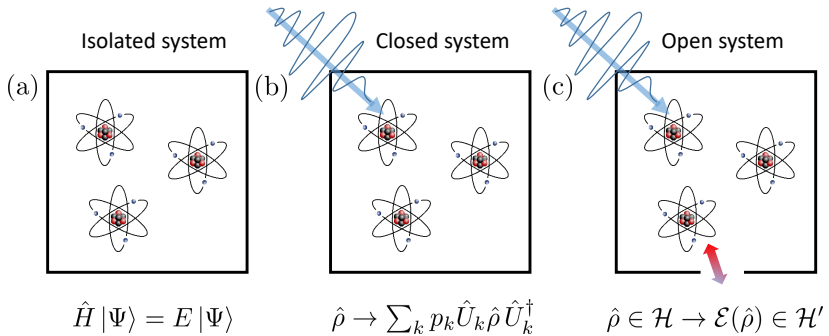


Figure 4.1: Evolution of three types of thermal systems. (a) Isolated system, governed by the time-independent Schrödinger equation. (b) Closed system, under influence of an external control field, e.g. a noisy laser, causing unitary evolution (see text). This type of system is governed by the time-dependent Schrödinger equation. (c) Open system, where particles or heat can be exchanged with the environment. This type of system can be described by a CPTP map [Dav76, Key02, Dan21], and generally gives rise to quantum dissipation [Fey63]. The inequalities described in this chapter hold for a closed system, but not for an open system.

4.1 Evolution of a composite system in a thermal state

We consider a collection of subsystems as our total closed system. The subsystems are initially uncorrelated, and each subsystem is prepared in a thermal state. The density operator for the total system is then given by

$$\hat{\rho}_0^{\text{tot}} = e^{-\beta_1 \hat{H}_1} \otimes \cdots \otimes e^{-\beta_N \hat{H}_N} / Z_0, \quad (4.1)$$

where $Z_0 = \text{tr} [e^{-\sum_{i=1}^N \beta_i \hat{H}_i}]$ is the partition function, \hat{H}_i are the Hamiltonians of the subsystems, and β_i correspond to the initial inverse temperatures. The evolution of this total system is governed by a microscopic form of the Clausius inequality [Cla65, Uzd18a, Str21],

$$\Delta S^{\text{sys}} + \sum_k \beta_k q_k^{\text{bath}} \geq 0, \quad (4.2)$$

where^{1,2} $q_k^{\text{bath}} = \Delta \text{tr} [\hat{\rho}_k \hat{H}_k] = \Delta \langle \hat{H}_k \rangle$ is the change in the average energy of microbath k . We consider any process, without restrictions, evolving the system from t_{initial} to t_{final} . A ‘microbath’ is defined as a small and initially thermal environment, which can develop strong correlations to any subsystem. When the system develops from an initial state ρ_0^{sys} to a final state ρ_f^{sys} , the change in entropy is given by $\Delta S^{\text{sys}} = S(\rho_f^{\text{sys}}) - S(\rho_0^{\text{sys}})$, where the von Neumann entropy is defined as $S^{\text{sys}}(\hat{\rho}^{\text{sys}}) \equiv -\text{tr} [\hat{\rho}^{\text{sys}} \ln \hat{\rho}^{\text{sys}}]$. $\text{tr} [\dots]$ denotes the trace, and the density operator for the system can be obtained by tracing out the baths, $\hat{\rho}^{\text{sys}} = \text{tr}_{\text{baths}} [\hat{\rho}^{\text{tot}}]$. Equation 4.2 basically states that the entropy for the total composite system can only remain constant, if the process is reversible, or increase, if the process is not reversible.

In our special case, there is no distinction between the ‘system’ and any microbath. Any part that would be considered the ‘system’ can be written as another sum of microbaths using the relation between entropy and heat transfer [Sch00] $\Delta S^{\text{sys}} = \oint \frac{\delta Q^{\text{sys}}}{T} = \sum_l \beta_l q_l^{\text{sys}}$. The Clausius inequality then reduces to a simple sum over microbaths

$$\sum_m \beta_m q_m \geq 0. \quad (4.3)$$

This inequality holds for arbitrary small systems, and for any unitary evolution, but not with initial correlations between the subsystems [Uzd18b]. We will come back to

¹ ΔX denotes the change for any operator or value X : $\Delta X \equiv X_{\text{final}} - X_{\text{initial}}$.

² The expectation value of an observable \hat{X} on a density operator $\hat{\rho}$ is defined as $\langle \hat{X} \rangle \equiv \text{tr} [\hat{\rho} \hat{X}]$ [Per02].

this equation later.

If the system is closed in the sense that only classical (possibly noisy) external driving fields are applied, an initial state $\hat{\rho}_0$ will evolve into a final state

$$\hat{\rho}_f = \sum_n p_n \hat{U}_n \hat{\rho}_0 \hat{U}_n^\dagger, \quad (4.4)$$

i.e. the evolution is determined by a mixture of unitary transforms \hat{U}_n , where p_n denotes the probability of performing the unitary \hat{U}_n . The driving field can vary due to noise, such that the performed unitary $\hat{U}_{n'}$ does not correspond to the desired \hat{U}_n . The transformation $\hat{U}_{n'}$ is different, but still unitary. In other words, a faulty operation can be represented by a mixture of unitary transforms, with probabilities p_n to perform a different, but still unitary, operation. This evolution is called *unital* [Men09]. It stands in contrast to the non-unital evolution of an open system, which exchanges particles or heat with an environment (see Fig. 4.1). The evolution of an open system is described by a completely positive trace-preserving (CPTP) map between spaces of operators: $\hat{\rho} \in \mathcal{H} \rightarrow \mathcal{E}(\hat{\rho}) \in \mathcal{H}'$. This map should preserve the normalization of states, and thus be trace-preserving (TP). It should map positive operators to positive operators, also when applied to part of a larger system, which is known as complete positivity (CP) [Dav76, Key02, Dan21].

Thus, by certifying non-unital evolution, we can determine that there must be a *heat leak* somewhere in the system. That is the heart of the technique presented here. How to certify non-unital evolution is given by the restrictions that the framework of passivity imposes.

4.2 Global passivity

Passivity [Pus78] always involves two operators. The condition for an operator \hat{X} to be denoted *passive* with respect to another operator \hat{Y} is

- $[\hat{X}, \hat{Y}] = 0$, i.e. the operators commute, a common set of eigenvectors exists.
- Decreasingly ordered eigenvalues of \hat{X} correspond to increasingly ordered eigenvalues of \hat{Y} .

We may replace \hat{X} by a special operator, the density operator of a quantum state, and \hat{Y} by another operator, the Hamiltonian: Now, a density operator $\hat{\rho}$ is passive with respect to a Hamiltonian \hat{H} , if the eigenvalues of the density operator (the probabilities) are decreasing, while the eigenvalues of the Hamiltonian (the energies) are increasing

(see Fig. 4.2). The most common example is a thermal (Gibbs) state $\hat{\rho} = e^{-\beta \hat{H}}/Z$, for which the state occupation probability monotonically decreases as a function of the energy eigenvalue. Hence, a thermal state is passive with respect to the Hamiltonian.

If a density operator $\hat{\rho}$ is not passive with respect to a particular Hermitian operator \hat{X} , we can always find a passive density operator $\hat{\rho}_{\text{pass}}^{(\hat{X})}$ by unitary transformation. We choose the transformation operator \hat{U}_t such that the expectation value of \hat{X} is the lowest possible. \hat{U}_t can be constructed by representing $\hat{\rho}$ in the eigenbasis of \hat{X} , and permuting the rows and columns such that the eigenvalues are monotonically decreasing. A permutation operator is always unitary. We then obtain $\hat{\rho}_{\text{pass}}^{(\hat{X})} = \hat{U}_t \hat{\rho} \hat{U}_t^\dagger$, for which

$$\langle \hat{X} \rangle_{\text{pass}} = \text{tr} [\hat{\rho}_{\text{pass}}^{(\hat{X})} \hat{X}] = \min_{\text{all } \hat{U}_t} \left[\text{tr} [\hat{U}_t \hat{\rho} \hat{U}_t^\dagger \hat{X}] \right]. \quad (4.5)$$

By definition, for this transformed density operator $\hat{\rho}_{\text{pass}}^{(\hat{X})}$, the expectation value is the lowest achievable:

$$\langle \hat{X} \rangle \geq \langle \hat{X} \rangle_{\text{pass}}. \quad (4.6)$$

Then, if we start with this density operator $\hat{\rho}_{\text{pass}}^{(\hat{X})}$, for which the expectation value is minimal, the difference of the expectation value of \hat{X} applied to any future state must be positive. Thus, with $\hat{\rho}_0 = \hat{\rho}_{\text{pass}}^{(\hat{X})}$,

$$\Delta \langle \hat{X} \rangle = \langle \hat{X} \rangle_f - \langle \hat{X} \rangle_0 = \text{tr} [\hat{\rho}_f \hat{X}] - \text{tr} [\hat{\rho}_0 \hat{X}] = \text{tr} [(\hat{\rho}_f - \hat{\rho}_0) \hat{X}] \geq 0, \quad (4.7)$$

for any unitary evolution $\hat{\rho}_f = \hat{U} \hat{\rho}_0 \hat{U}^\dagger$. By linearity, this inequality also holds if the evolution is described by a mixture of unitaries, as in unital evolution (Eq. 4.4).

Instead of finding a passive density operator $\hat{\rho}_{\text{pass}}^{(\hat{X})}$ for a particular operator \hat{X} , we can also do the inverse. That means finding an operator $\hat{X}_{\hat{\rho}_{\text{pass}}}$ that is passive with respect to a particular density operator $\hat{\rho}$. Returning to our composite system in a thermal state (Eq. 4.1), we choose

$$\hat{X}_{\hat{\rho}_{\text{pass}}} = \hat{B} \equiv -\ln \hat{\rho}. \quad (4.8)$$

It is simple to verify that \hat{B} is passive with respect to $\hat{\rho}_0$: By inverting Eq. 4.8, we find $\hat{\rho} = e^{-\hat{B}}$, which implies that larger eigenvalues of \hat{B} are associated with lower probabilities. As we have seen before from Eq. 4.7, if we start with a density operator that is passive with respect to an observable, the difference in expectation value for

any unital evolution must be positive,

$$\Delta\langle\hat{B}\rangle \geq 0. \quad (4.9)$$

If we apply \hat{B} (Eq. 4.8) to our initial state $\hat{\rho}_0^{\text{tot}}$ (Eq. 4.1), we find

$$\hat{B}(\hat{\rho}_0^{\text{tot}}) = \sum_k \beta_k \hat{H}_k + \ln(Z_0) \mathbb{1}, \quad (4.10)$$

where $\mathbb{1}$ is the identity operator. Now, the difference in expectation value of \hat{B} comes down to the sum over the differences in expectation values of the Hamiltonian. Additionally, we can use our earlier definition of q_k as the change in the average energy of microbath k , and obtain

$$\Delta\langle\hat{B}\rangle = \sum_k \beta_k \Delta\langle\hat{H}_k\rangle = \sum_k \beta_k q_k \geq 0, \quad (4.11)$$

which is equivalent to the reduced Clausius inequality for this system (Eq. 4.3). Using the global passivity³ framework we have now derived an equation similar to the Clausius inequality. However, this inequality can be extended to include strong correlations between the subsystems. This can be useful for a number of reasons, as discussed in [Uzd18b]. For this work, we use Eq. 4.9 to generate a new family of global passivity inequalities, by defining a new operator

$$\hat{B}^\alpha \equiv \text{sgn}(\alpha) (-\ln \hat{\rho})^\alpha \quad \forall \alpha > 0, \alpha \in \mathbb{R}. \quad (4.12)$$

Using the same reasoning we can verify that this operator is also globally passive with respect to the density operator, and conclude

$$\Delta\langle\hat{B}^\alpha\rangle \geq 0. \quad (4.13)$$

The exponent α can be used to tune the sensitivity of the inequality. As before, the inequality only holds for unital evolution. Non-unital evolution, possibly due to a heat leak, may cause a difference in expectation values of \hat{B}^α below zero. Figure 4.3 shows the effect that different values of α have in a specific example. In general, for $\alpha \gg 1$, the largest eigenvalue of \hat{B} dominates, and it corresponds to the smallest eigenvalue of

³ We use the term global passivity to indicate that passivity applies to the whole closed system ($\hat{\rho}_0^{\text{tot}}$), not just to a subsystem of interest, as is the case in standard passivity [Pus78].

$\hat{\rho}_0$, as \hat{B}^α is passive with respect to $\hat{\rho}_0$. Thus, as $\alpha \rightarrow +\infty$, inequality Eq. 4.13 states that the probability of the state that was initially least populated cannot decrease beyond its initial value. Conversely, for $\alpha \rightarrow -\infty$ we learn that the probability of the state that was initially most populated cannot increase beyond its initial value. Different values of α put emphasis on different eigenvalues of the expectation values, and can therefore potentially detect different types of heat leaks.

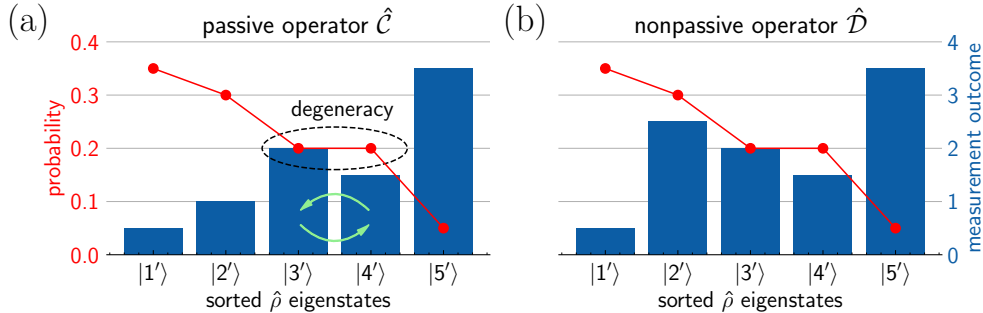


Figure 4.2: An operator \hat{C} is passive with respect to a density operator ρ_0 if a common set of eigenvectors exists, and if increasingly ordered eigenvalues of \hat{C} (measurement outcomes) correspond to decreasingly ordered eigenvalues of $\hat{\rho}$ (probabilities). Degeneracies allow for local deviations in ordering.

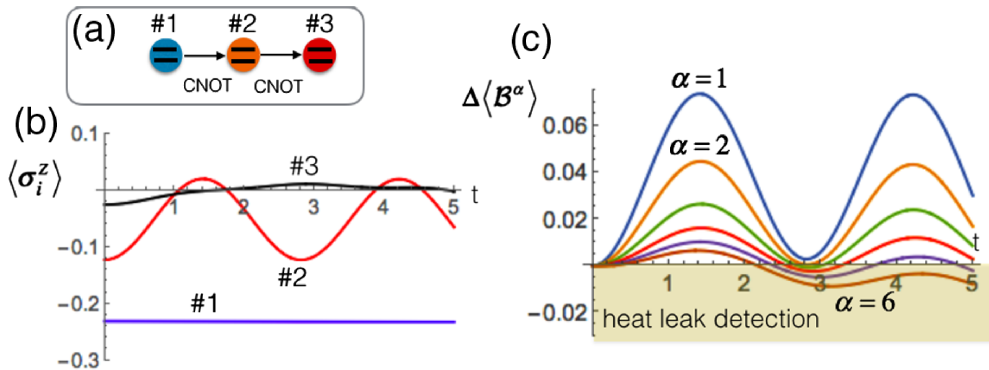


Figure 4.3: Example calculation of $\Delta\langle\hat{B}^\alpha\rangle$ for different values of α , showing that α affects the sensitivity to heat leaks. (a) For a system of three qubits, two CNOT gates are simultaneously and repeatedly applied. Each qubit has a small chance of decaying to the ground state, which forms the heat leak in this example. The decay becomes dominant after 1000 CNOT cycles. (b) Expectation values of the polarization for each qubit as a function of time in CNOT cycles. (c) Expectation value $\Delta\langle\hat{B}^\alpha\rangle$ as a function of time, for different values of α . $\alpha = 1$, which corresponds to the Clausius inequality (Eq. 4.2), stays positive during the first 5 cycles, whereas $\alpha = 6$ turns negative after a little more than 2 cycles. This example is taken from [Uzd18b].

4.3 Passivity deformation

Using the concept of passivity deformation we can derive even tighter constraints on the evolution of our composite system. Passivity deformation uses a globally passive operator \hat{B} to generate inequalities involving another observable \hat{A} that does not have to be passive. We introduce the operator

$$\hat{B}' = \hat{B} + \xi \hat{A} \quad (4.14)$$

where $\xi \in \mathbb{R}$ is the deformation parameter, and \hat{A} is any observable of interest that commutes with the globally passive operator \hat{B} : $[\hat{B}, \hat{A}] = 0$. Then, \hat{B} and \hat{B}' have the same eigenstates. We can expect the operator \hat{B}' to be globally passive as well for a certain range of deformation parameters ξ . If the eigenvalue ordering of \hat{A} and \hat{B} is the same, the global passivity of \hat{B} is inherited by \hat{B}' and the inequality

$$\Delta\langle\hat{B}'\rangle \geq 0 \quad (4.15)$$

holds for any value of ξ and any unital evolution. Otherwise, if \hat{A} is not globally passive, and the deformation parameter ξ is nonzero, the inequality does not have to hold. However, there is a finite range of ξ values for which \hat{B}' is always globally passive, independent of \hat{A} (see Fig. 4.4a). The tightest constraints on the evolution are obtained for the largest values of $|\xi|$ within this range.

We will now continue with the derivation of this range of ξ parameters for which \hat{B}' is globally passive. If \hat{A} is not globally passive, there is a nonzero value of ξ for which degeneracies appear, as shown in Fig. 4.4b. Above this value of $|\xi|$ the order of the operator eigenvalues changes and \hat{B}' is no longer globally passive, as shown in Fig. 4.4c.

The condition for degeneracy between successive eigenvalues $\lambda_k^{(\hat{A}, \hat{B})}$ of operators \hat{B} and \hat{A} is

$$\lambda_{k+1}^{(\hat{B})} + \xi \lambda_{k+1}^{(\hat{A})} = \lambda_k^{(\hat{B})} + \xi \lambda_k^{(\hat{A})}. \quad (4.16)$$

Using this condition, we can define critical values ξ_k , where degeneracies appear:

$$\xi_k = \frac{\lambda_{k+1}^{(\hat{B})} - \lambda_k^{(\hat{B})}}{\lambda_k^{(\hat{A})} - \lambda_{k+1}^{(\hat{A})}}, \quad (4.17)$$

where k values that nullify the numerator or denominator are excluded, since degeneracies in either \hat{A} or \hat{B} do not affect the relative ordering of the two operators. From

these critical values ξ_k we can define a range where the operator \hat{B}' is passive:

$$\xi_m = -\min(-\xi_k > 0) \quad \text{and} \quad \xi_p = \min(\xi_k > 0), \quad (4.18)$$

such that Eq. 4.15 holds for $\xi_m < \xi < \xi_p$. If the eigenvalues of \hat{B} and \hat{A} are known, finding the limit values $\xi_{m,p}$ analytically or numerically is a simple task, as we will see in Chapter 6.

Thus, by rewriting Eq. 4.15, we obtain the passivity deformation inequality

$$\Delta\langle\hat{A}\rangle \geq -\frac{1}{\xi}\Delta\langle\hat{B}\rangle \quad \forall \quad \xi_m \leq \xi \leq \xi_p \quad (4.19)$$

Often, as in our earlier example for a composite system in a thermal state, \hat{B} will describe energetics (see Eq. 4.10). In contrast, \hat{A} may describe a non-thermal property, like the ground state population, and its evolution can still be bound (i.e. Eq. 4.15 requires that the dynamics is restricted to a subset of allowed unitaries). Furthermore, unlike global passivity, the passivity deformation inequality is guaranteed to be tight, even when the environment is small, and in the case of non-thermal initial states and/or correlation buildup. Consequently, the passivity deformation inequality may have stronger sensitivity for detecting heat leaks, as we will see in Chapter 6.

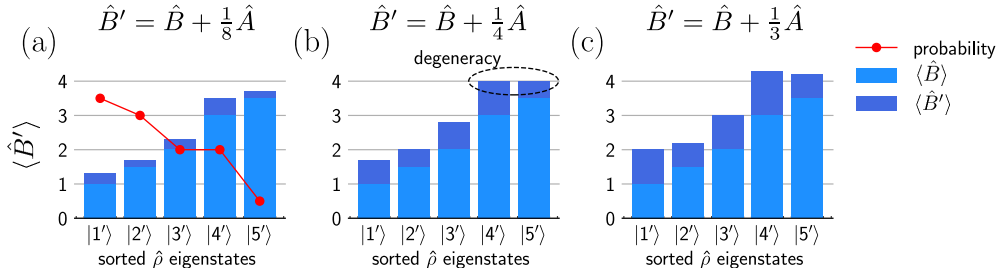


Figure 4.4: Three cases of passivity deformation, showing eigenvalues of \hat{B} and \hat{B}' (see Eq. 4.14), for different values of ξ . (a) For a passive operator \hat{B} , non-passive operator \hat{A} , and sufficiently small ξ , \hat{B}' is also passive. (b) For $\xi = \frac{1}{4}$, degeneracies appear. (c) For $\xi > \frac{1}{4}$, \hat{B}' is no longer passive.

Chapter 5

Experimental Realization of Global Passivity

In this chapter, we apply the framework of global passivity to a system of two qubits, with an additional third qubit representing the environment. All qubits are initialized in thermal states, such that they represent the thermal baths described in Chapter 4. The two system qubits undergo unital evolution, and are optionally coupled to the environment qubit via a SWAP gate. The global passivity framework is then used to detect this coupling, crucially, by only measuring the system qubits. The capability of detection is compared for the microscopic second law (Eq. 4.11), and the global passivity inequality (Eq. 4.13). Special attention is given to the calibration of the thermal state initialization, and to the calibration of a customized entangling gate employed in the unitary evolution of the system qubits.

5.1 Framework application to a collection of three qubits

We consider a cold qubit c and a hot qubit h , each described by Hamiltonian $\hat{H}_{c,h}$, and initial thermal states

$$\hat{\rho}_j^{(0)} = e^{-\beta_j \hat{H}_j} / Z_j \quad j = c, h \quad (5.1)$$

with inverse temperature β_j and partition functions $Z_j = \text{tr}[e^{-\beta_j \hat{H}_j}]$. The initial state of the joint cold/hot system is uncorrelated

$$\hat{\rho}_0^{\text{tot}} = \hat{\rho}_c^{(0)} \otimes \hat{\rho}_h^{(0)} = \frac{e^{-(\beta_c \hat{H}_c \oplus \beta_h \hat{H}_h)}}{Z_c Z_h}. \quad (5.2)$$

Analog to Eq. 4.10-4.13, choosing a passive operator $\hat{B}^\alpha \equiv \text{sgn}(\alpha)(-\ln \hat{\rho})^\alpha$ yields

$$\hat{B}^\alpha(\hat{\rho}_0^{\text{tot}}) = \text{sgn}(\alpha)(\beta_c \hat{H}_c \oplus \beta_h \hat{H}_h + d \mathbb{1}_{ch})^\alpha \quad (5.3)$$

where $\mathbb{1}_{ch}$ is the identity operator on the product Hilbert space of qubits c and h , and d is a suitable constant to enforce nonzero and positive eigenvalues. $\ln(Z_c Z_h)$ is absorbed in d . For the difference in expectation value of \hat{B}^α , we obtain the family of global passivity inequalities (Eq. 4.13)

$$\Delta \langle \hat{B}^\alpha \rangle = \Delta \langle \text{sgn}(\alpha) (\beta_c \hat{H}_c \oplus \beta_h \hat{H}_h + d \mathbb{1}_{ch})^\alpha \rangle \geq 0. \quad (5.4)$$

Note that the microscopic form of the second law, Eq. 4.11, is retrieved for $\alpha = 1$. A violation of the inequality Eq. 5.4, for any given value of α , necessarily implies that one of the underlying assumptions is violated, either that the initial state is not passive or that the system evolution is not unital, indicating an interaction with some environment. In this case, the environment is modeled by a third qubit e , which is also initialized in a thermal state.

For each system qubit (c, h) , we assign the dimensionless energy eigenvalues $E_0 = 0$ and $E_1 = 1$ to the qubit states, such that

$$\hat{H}_j |0_j\rangle = 0 \quad \text{and} \quad \hat{H}_j |1_j\rangle = |1_j\rangle \quad j = c, h. \quad (5.5)$$

Thus, the free Hamiltonian reads

$$\hat{H}_j = |1_j\rangle \langle 1_j| \quad j = c, h. \quad (5.6)$$

The inverse spin temperatures β_j for $j = c, h, e$ (in terms of the dimensionless energy eigenvalues) are given from the Boltzmann weights via

$$\beta_j = \ln \left(p_0^{(j)} / \left(1 - p_0^{(j)} \right) \right), \quad (5.7)$$

where $p_0^{(j)}$ is the population of state $|0_j\rangle$, ranging from 0 to 1. Note that the definition of the qubit states $|0\rangle$ and $|1\rangle$ is opposite to what is defined in Chapter 2. This choice was made due to the technical realization of optical pumping (from $|\downarrow\rangle$ to $|\uparrow\rangle$), and to keep the intuitive definition of $|0\rangle$ as the ‘ground state’.

5.2 Quantum circuit formulation and implementation

The quantum circuit for demonstrating a violation of Eq. 5.4 is shown in Figure 5.1. For the simplest possible demonstration, a single entangling gate enclosed by two global single qubit gates was chosen as unitary evolution for the system qubits. The

initial spin temperatures (see Table 5.1), as well as the single qubit rotation angles, and a customized phase for the two-qubit light-shift gate (see Chap. 2), were chosen to provide optimum sensitivity for detection of the heat leak. For the two-qubit gate, the evolution is described by

$$\begin{aligned} \{|0_c0_h\rangle, |1_c1_h\rangle\} &\rightarrow e^{i\Phi} \{|0_c0_h\rangle, |1_c1_h\rangle\} \\ \{|0_c1_h\rangle, |1_c0_h\rangle\} &\rightarrow \{|0_c1_h\rangle, |1_c0_h\rangle\}. \end{aligned} \quad (5.8)$$

with $\Phi = 3\pi/4$. The single qubit gates are rotations applied individually to both system qubits, described by

$$\hat{U}_y = \exp \left(-i \frac{\pi}{4} (\hat{\sigma}_y^{(c)} \oplus \hat{\sigma}_y^{(h)}) \right), \quad (5.9)$$

where $\hat{\sigma}_y^{(j)}$ is the Pauli Y operator (Eq. 2.12) for qubit j . After this unitary evolution, the optional coupling to the environment qubit is provided by a full SWAP operation [Nie10]. The SWAP operation was chosen because it is a native operation with high fidelity on the current platform [Kau17b]. In future experiments, the SWAP gate could be replaced by an operation that mimics more realistic system-bath interactions, e.g. Ising-type coupling or SWAP^{-n} gates mimicking thermalization.

qubit j	$p_0^{(j)}$	β_j
c	0.097(4)	2.23(4)
h	0.395(6)	0.43(2)
e	0.117(4)	2.02(4)

Table 5.1: Initial spin temperatures, expressed in measured population $p_0^{(j)}$ of state $|0_j\rangle$, and computed inverse temperature β_j (using Eq. 5.7). For the populations, the closest round numbers were chosen as target, to provide optimum sensitivity for detection of the heat leak.

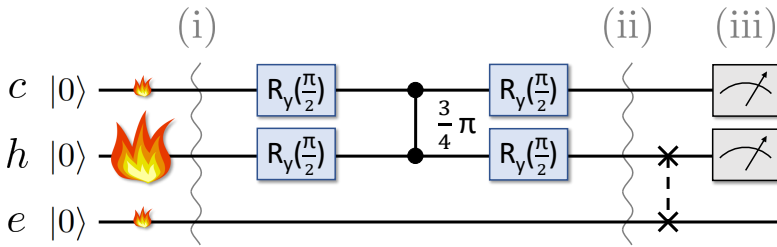


Figure 5.1: Quantum circuit used for demonstrating a violation of the global passivity inequality Eq. 5.4. All qubits are initialized to thermal states (before (i)), the system qubits undergo unitary evolution (before (ii)), and one of the system qubits is optionally swapped with the environment qubit before measurement (iii). Initialization to thermal states is depicted by the flame, with the flame size indicating the spin temperature.

For implementation of the quantum circuit shown in Fig. 5.1, the following shuttling sequence is performed. Each experimental run starts with Doppler and sideband cooling, and initialization to $|0\rangle$ (see Chap. 2), after which qubits c , h , and e are successively moved to the laser interaction zone (LIZ) and initialized to thermal states by controlled incomplete optical pumping (see Section 2.1). Next, the system qubits c, h are stored pairwise at the LIZ while the unitary evolution is realized as laser-driven single- and two-qubit gates, as explained in Chapters 2 and 3. After the coherent evolution, qubits c and h are separated [Kau14], then qubits h and e are merged at the LIZ, where they can undergo an optional SWAP gate. If toggled on, it gives rise to a heat leak as energy exchange between h and e takes place. The SWAP gate is executed via physical swapping of the ion positions, which has been shown to realize a unit-fidelity gate in [Kau17b]. Finally, all qubits are read out successively. While all qubits are read out for calibration and monitoring purposes, only the results of qubit c and h ¹ are used for detection of the heat leak. The shuttling sequence is depicted in Figure 5.2. After each experimental run, all ion states are successively reset and detected. If an ion was lost, an automated retrapping sequence is performed. The ions are returned to their initial positions before the next experimental run. The total duration of one experimental run is 13.4 ms.

¹ The ions are also labelled c , h , and e . After the optional SWAP operation, ion e becomes qubit h and vice versa.

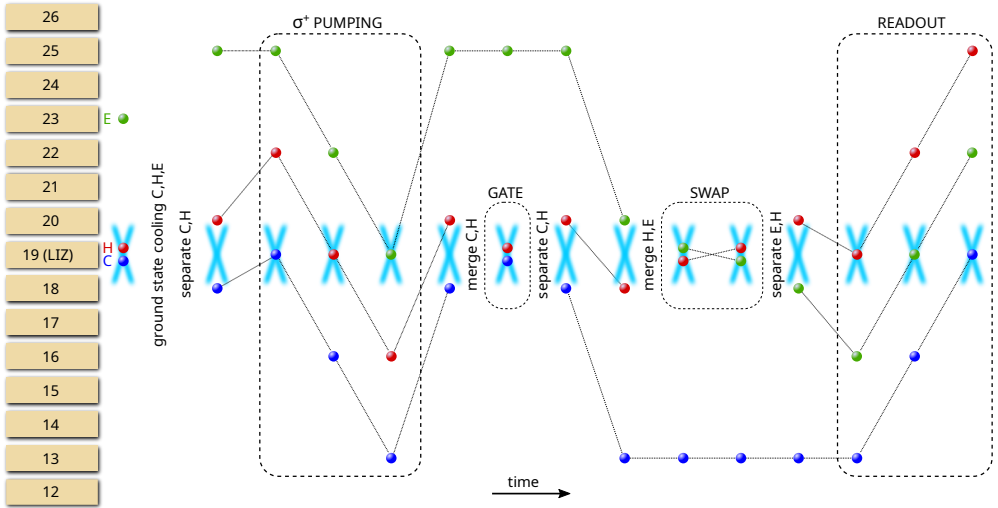


Figure 5.2: Experimental shuttling sequence that realizes the quantum circuit shown in Fig. 5.1. Movement of ions c (blue), h (red), and e (green) is shown relative to trap segments 12-26 (goldbrown). All laser-driven operations are performed at segment 19. The main elements of the quantum circuit are highlighted. The SWAP gate is optional, which only changes the order of readout. The full sequence contains 21 qubit operations (initialization, gates, readout) and 29 shuttling operations.

5.3 Thermalization and customized entangling gate calibration

Aside from the daily calibrations described in Chapter 2, the controlled incomplete optical pumping, and the customized two-qubit light-shift gate require special calibration. For the optical pumping, a single ion is initialized to $|0\rangle$, after which an optical pumping pulse of varying length is applied. The desired populations $p_0^{(j)}$ of state $|0_j\rangle$ are matched to pulse durations, which are then applied to the full measurement sequence. Due to laser intensity and polarization fluctuations, averaging over a high number of repetitions is needed. A typical curve with 5000 repetitions per point is shown in Fig. 5.3. Note that the qubits are usually initialized to $|4S_{1/2}, m_J = +1/2\rangle = |\uparrow\rangle$ after sideband cooling, but that optical pumping only works from $|\downarrow\rangle$ to $|\uparrow\rangle$. Prior to optical pumping, the state can be swapped via either a Raman π pulse, or 10 cycles of 729 pumping on the $|4S_{1/2}, m_J = +1/2\rangle \leftrightarrow |3D_{5/2}, m_J = -3/2\rangle$ transition. Any fluctuation in state preparation would carry over into the final results. Both methods were tried, but no significant difference was observed. The final data was taken using a Raman π pulse before optical pumping.

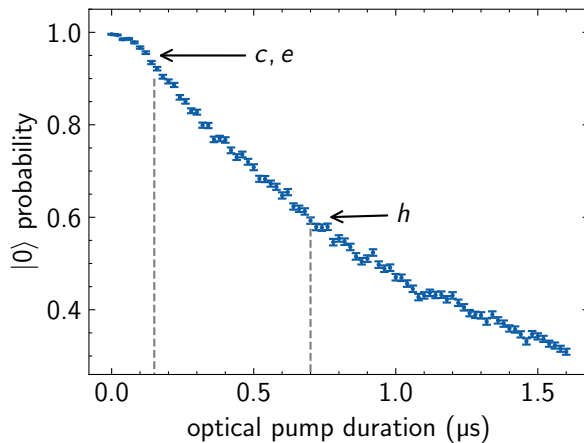


Figure 5.3: Calibration curve for thermal state preparation via optical pumping, showing population $p_0^{(j)}$ of state $|0_j\rangle$ as a function of pulse duration. 5000 repetitions per point are used.

For calibration of the light-shift gate with phase $\Phi = 3\pi/4$, several methods were developed. Starting from a calibrated gate with phase $\Phi = \pi/2$ and a fidelity of $> 99\%$ (see Chap. 2), the required laser intensity is estimated at 1.5 times the calibrated value. Except for one, all methods perform the full shuttling sequence to include any systematic effects.

The first method involves measuring the binary probabilities for qubit c and h directly after the gate, while scanning either the gate pulse duration or amplitude, and computing the root-mean-square error (rmse) [Hyn06] to the theoretically expected probabilities. The qubits are initialized to an even and odd state and rmse curves are compared. A pulse duration and amplitude scan for a gate applied to an even state ($|00\rangle$) is shown in Figure 5.4. Note that the ideal pulse duration is expected to be similar to the duration for the $\Phi = \pi/2$ gate. To first order, the geometric phase only depends on the pulse amplitude (see Chap. 2). However, since we are using shaped pulses, and because of a small intensity-dependent Stark shift, the ideal duration and intensity may be somewhat interdependent. Nevertheless, the rmse measurement did not lead to significantly different pulse durations from the $\Phi = \pi/2$ gate.

A second method uses adapted cycle benchmarking sequences (see Section 2.3). Twenty random gate sequences containing each 4 two-qubit $\Phi = 3\pi/4$ gates were generated. Of these twenty sequences, five sequences showed significant sensitivity to the employed gate pulse amplitude. An example of the success rate of these sequences as a function of gate pulse amplitude is shown in Figure 5.5. Due to the already

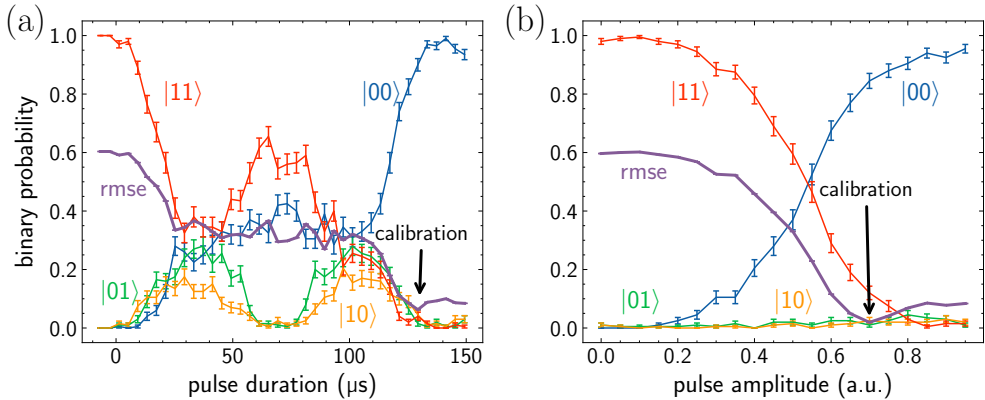


Figure 5.4: First two-qubit gate phase calibration method. After applying the gate to a $|00\rangle$ state, binary probabilities for qubit c, h are measured and the rmse to the target state is computed. (a) Scanning gate pulse duration. (b) Scanning gate pulse amplitude.

existing software infrastructure for cycle benchmarking, this experiment was performed on a two-ion crystal initialized to $|00\rangle$, without any further operations apart from the random gate sequence.

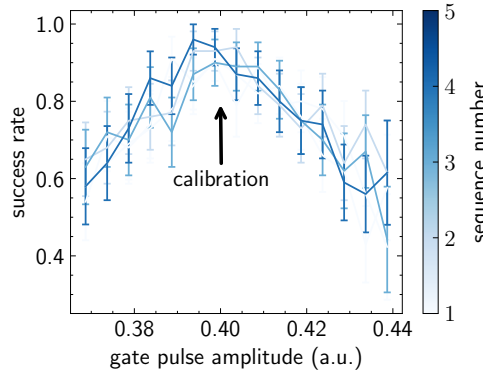


Figure 5.5: Second two-qubit gate phase calibration method. Five cycle benchmarking sequences containing each 4 gates with phase $\Phi = 3\pi/4$ are applied to two qubits in initial state $|00\rangle$. The success rate is shown as a function of gate pulse amplitude.

A third method consists of running the global passivity protocol (Fig. 5.1) up to i) after thermal state initialization, and ii) after the unitary evolution, for varying gate pulse amplitude. Each amplitude is repeated for 50 shots, the expectation values are evaluated (Eq. 5.10), and compared to theoretical expectation values that were computed using the measured thermal state probabilities and the ideal unitary evolution. This is essentially calibrating the two-qubit gate on the final measurement result. An

example calibration curve is shown in Figure 5.6. This method did not give consistent and precise enough results with the number of shots that were used, most likely due to fluctuations in the optical pump laser intensity.

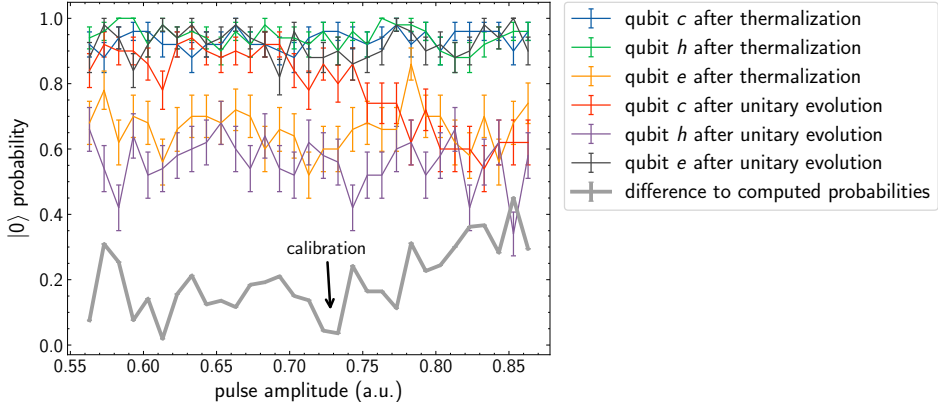


Figure 5.6: Third two-qubit gate phase calibration method. For every repetition, the circuit of Fig. 5.1 is performed up to i) after thermal state initialization, and ii) after the unitary evolution. Expectation values for \hat{B}^α (Eq. 5.10) are computed using measurement data, and using the ideal unitary evolution. The difference as a function of gate pulse amplitude, shown in grey, is used for calibration. Large fluctuations can be observed in the thermal state preparation, most likely due to intensity or polarization noise of the optical pumping laser.

The final and most successful method uses a Ramsey-type measurement [ROO08b] to directly deduce the accumulated geometric phase. Two qubits are initialized to $|00\rangle$. The control qubit is optionally flipped while the target qubit is projected to the X-basis. The geometric phase gate is performed and the target qubit is projected and measured in the X- and Y-basis (see Fig. 5.7). The phase is calculated using a Bayes phase estimation algorithm [Hil22a]. Finally, the phase of the target qubit is compared for both control qubit states. As the control qubit determines the direction of the phase shift, the difference is twice the phase shift per gate. An example calibration is shown in Figure 5.8. The calibration for the final measurement data was performed using this method.

To obtain a measure for the precision of the calibration, the theoretical binary probabilities after the unitary evolution were calculated for a range of geometric phases, using the measured thermal state populations (before the unitary evolution). The final theoretical populations are compared to the measured populations and the minimum of the summed differences is taken as the effective geometric phase, illustrated in Fig. 5.9. Aiming for 0.75π , we obtain an accuracy of 0.018π rad.

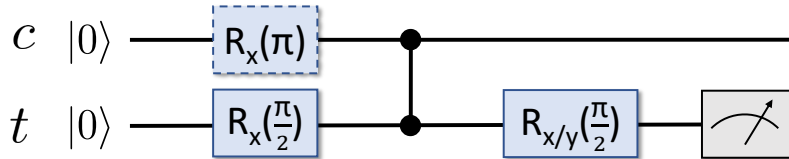


Figure 5.7: Quantum circuit for measuring the geometric phase of the light-shift gate. The control qubit (c) is prepared in $|0\rangle$ or $|1\rangle$, while the target qubit (t) is prepared in the X-basis. After applying the light-shift gate, the target qubit is projected to the X- or Y-basis and measured. The phase difference for the two target qubit states is twice the applied geometric phase.

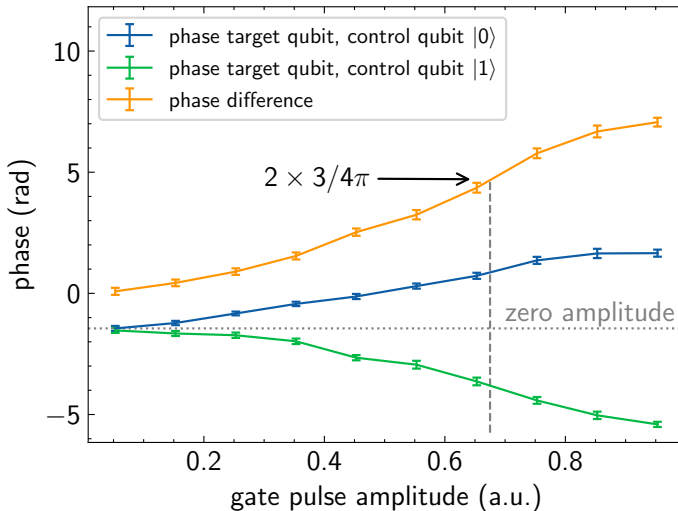


Figure 5.8: Fourth two-qubit gate phase calibration method. The circuit of Fig. 5.7 is used to measure the phase of the target qubit for two control qubit states. The calculated phase difference is twice the applied geometric phase.

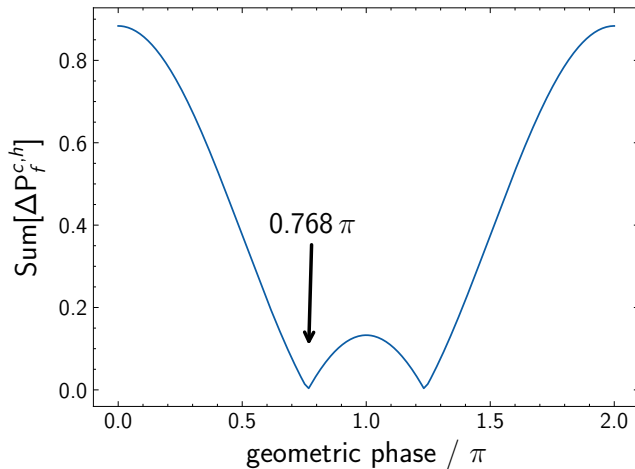


Figure 5.9: For one set of probabilities of qubit c, h after thermal state initialization and after unitary evolution, the theoretical unitary evolution is compared to the measured values, for a range of theoretical geometric phases. The summed difference in final probabilities is shown, and the minimum is taken as the effective calibrated geometric phase.

The gate stability is evaluated by repeating the measurement of Fig. 5.8 75 times over a timespan of ~ 5 hours, and computing the root-mean-square difference between the collected phase as a function of gate pulse amplitude. We find a linear drift of $\frac{0.82}{1000} \pi$ rad/min.

5.4 Readout and evaluation

The qubits are read out via laser-driven, state-selective population transfer to the metastable $D_{5/2}$ state, followed by detection of state-dependent laser-induced fluorescence, as explained in Chap. 2. In this case, above (below)-threshold detection of fluorescence corresponds to the qubit being detected in $|0\rangle$ ($|1\rangle$). Repeated execution of the experimental sequence yields estimates of the occupation probabilities for each logical basis state of the qubit register. The relevant error sources are given by shot noise for a finite number of shots, yielding statistical errors, and systematic measurement errors.

Each repetition k yields one of the results $\{|0_c 0_h\rangle, |0_c 1_h\rangle, |1_c 0_h\rangle, |1_c 1_h\rangle\}$, corresponding to the measured energies $E_j^{(k)} = \{0, +1\}$ for system qubits c and h . This

yields the single-shot measurement result of operator \hat{B}^α (Eq. 5.3) via

$$B_{(k)}^\alpha = \text{sgn}(\alpha)(\beta_c E_c^{(k)} + \beta_h E_h^{(k)} + d)^\alpha. \quad (5.10)$$

From N acquired shots, we evaluate the expectation values by evaluating sample averages based on the obtained single-shot measurement results (Eq. 5.10). We acquire three independent data sets, each consisting of 6700 shots in total, for the cases where the measurements take place i) after thermal state preparation, ii) after the gates acting on c and h , without the SWAP gate and iii) after the SWAP gate between qubits h and e . Expectation values $\langle \hat{B}^\alpha \rangle$ are computed for all three data sets for varying α . Changes $\Delta\langle \hat{B}^\alpha \rangle$ with respect to α are then computed for both the cases with and without SWAP gate, with respect to the expectation values computed for the initial thermal state. The results are shown in Fig. 5.10. Estimates for the statistical error are computed via non-parametric bootstrapping: Artificial event rates for detecting $\{|0_c 0_h\rangle, |0_c 1_h\rangle, |1_c 0_h\rangle, |1_c 1_h\rangle\}$ are generated by drawing event numbers from a multinomial distribution, governed by the measured event rates. These rates are used for computing expectation values $\langle \hat{B}^\alpha \rangle$ from Eq. 5.10, which are used in turn to compute a 1σ error channel.

For the case without SWAP gate, we observe $\Delta\langle \hat{B}^\alpha \rangle \geq 0$ for the entire range of α values, which indicates unital evolution of qubits c and h . In contrast, for the case with SWAP gate, we observe $\Delta\langle \hat{B}^\alpha \rangle \leq 0$ for values of α below 0.5090(75). This shows a clear violation of the global passivity inequality (Eq. 5.4). Note that the microscopic form of the second law ($\alpha = 1$) provides $\Delta\langle \hat{B} \rangle \geq 0$, which confirms that the framework of global passivity provides an increased sensitivity for experimental verification of heat leaks.

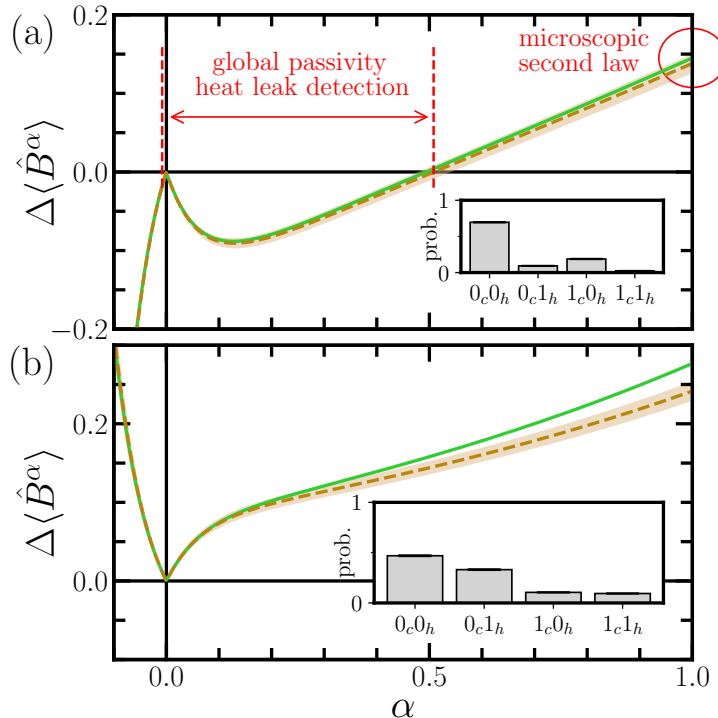


Figure 5.10: Results of the global passivity protocol, Fig. 5.1, 6700 repetitions: $\Delta\langle\hat{B}^\alpha\rangle$ is shown as a function of α . (a) For the case with final SWAP gate, the system qubits are coupled to the environment qubit, and we observe $\Delta\langle\hat{B}^\alpha\rangle \leq 0$ for $\alpha < 0.5090(75)$. (b) For the case where the SWAP gate is not performed, we observe no violation of the global passivity inequality (Eq. 5.4). The experimental data (dashed) is shown along with error channels (shaded, see text) and compared to theoretical values (green). The insets show the measured populations for system qubits c, h , from which the experimental data is calculated.

Chapter 6

Implementation of Passivity Deformation

In this chapter, the application of the global passivity framework to a collection of three qubits from Chapter 5 is expanded with the framework of passivity deformation. The initial spin temperatures are chosen slightly different, and the two-qubit geometric phase gate in the unitary evolution is replaced by a full SWAP gate. We discuss the choice of deformation parameter \hat{A} , the changes in the circuit, and the calibration of the SWAP gate. The SWAP gate is implemented as a physical swapping of the ion positions, or as a laser-driven gate. Finally, we compare the sensitivity of passivity deformation to that of global passivity.

6.1 Framework application

We start with the same definitions as in Chapter 5, Equations 5.1-5.7. As deformation operator \hat{A} (see Eq. 4.14), we choose the Hamiltonian of the hot qubit. Using Eq. 5.6, we then obtain

$$\hat{A} = \hat{H}_h = \mathbb{1}_c \otimes |1_h\rangle \langle 1_h|, \quad (6.1)$$

such that

$$\begin{aligned} \hat{B}^\alpha &= \text{sgn}(\alpha)(\beta_c \hat{H}_c \oplus \beta_h \hat{H}_h + d \mathbb{1}_{ch})^\alpha \\ \hat{B}' = \hat{B} + \xi \hat{A} &= \beta_c \hat{H}_c \oplus (\beta_h + \xi) \hat{H}_h + d \mathbb{1}_{ch}. \end{aligned} \quad (6.2)$$

Both operators \hat{B} and \hat{B}' are diagonal, with eigenvalues

$$\begin{aligned} \text{eig}(\hat{B}) &= \{0, \beta_h, \beta_c, \beta_h + \beta_c\} \\ \text{eig}(\hat{B}') &= \{0, \beta_h + \xi, \beta_c, \beta_h + \beta_c + \xi\}. \end{aligned} \quad (6.3)$$

The inverse temperatures β_i are shown in Table 6.1. Note that the eigenvalues of \hat{B} are sorted, while the eigenvalues of \hat{B}' are not necessarily sorted, due to the variable ξ . The inequality $\langle \hat{B}' \rangle \geq 0$ requires the eigenvalues of \hat{B}' to have the same sorting as for \hat{B} , which leads to a definition of ξ_m and ξ_p :

$$\begin{aligned}\beta_h + \xi &\leq \beta_c \leq \beta_h + \beta_c + \xi \\ \beta_h + \xi_p &= \beta_c = \beta_h + \beta_c + \xi_m\end{aligned}$$

such that the range of valid values for ξ is

$$-\beta_h = \xi_m \leq \xi \leq \xi_p = \beta_c - \beta_h. \quad (6.4)$$

Using the definitions in Equations 6.1 and 6.2, the passivity deformation inequality (Eq. 4.19) then yields

$$\Delta\langle \hat{H}_c \rangle \geq -\frac{\beta_h + \xi}{\beta_c} \Delta\langle \hat{H}_h \rangle \quad \forall \xi_m \leq \xi \leq \xi_p. \quad (6.5)$$

This inequality holds for any unital evolution. A violation therefore indicates non-unital evolution, i.e. a heat leak. The quantum circuit formulated in the next section is optimized for the demonstration of such a heat leak, in the case of interaction with the environment qubit.

qubit j	$p_0^{(j)}$	β_j
h	0.250(8)	1.10(4)
c	0.166(7)	1.62(5)
e	0.097(5)	2.23(6)

Table 6.1: Initial spin temperatures, expressed in measured population $p_0^{(j)}$ of state $|0_j\rangle$, and computed inverse temperature β_j (using Eq. 5.7). For the populations, the closest round numbers were chosen as target, to provide optimum sensitivity for detection of the heat leak.

6.2 Quantum circuit formulation and implementation

The initial spin temperatures (Table 6.1) and the unitary evolution were chosen to detect a heat leak for the widest range of initial spin temperatures, to allow for some miscalibration or drift of the optical pumping. As depicted in Fig. 6.1, the joint local qubit rotations are replaced by a rotation about 2.5 rad of qubit h only. The phase

gate between qubit c and h is replaced by a SWAP gate.

To allow for the single qubit rotation on qubit h , ion h is individually shuttled to the LIZ before and after the first SWAP gate. Otherwise, the shuttling sequence remains the same, as illustrated in Fig. 6.2.

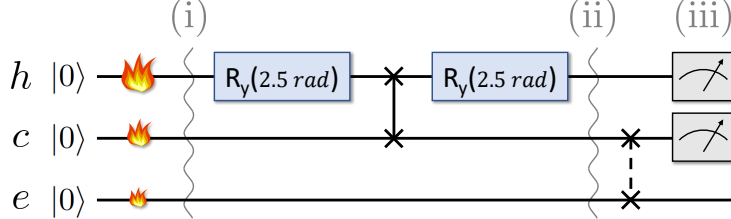


Figure 6.1: Quantum circuit used for demonstrating a violation of the passivity deformation inequality Eq. 4.19. All qubits are initialized to thermal states (before (i)), the system qubits undergo unitary evolution (before (ii)), and one of the system qubits is optionally swapped with the environment qubit before measurement (iii). Initialization to thermal states is depicted by a flame, with the flame size indicating the spin temperature.

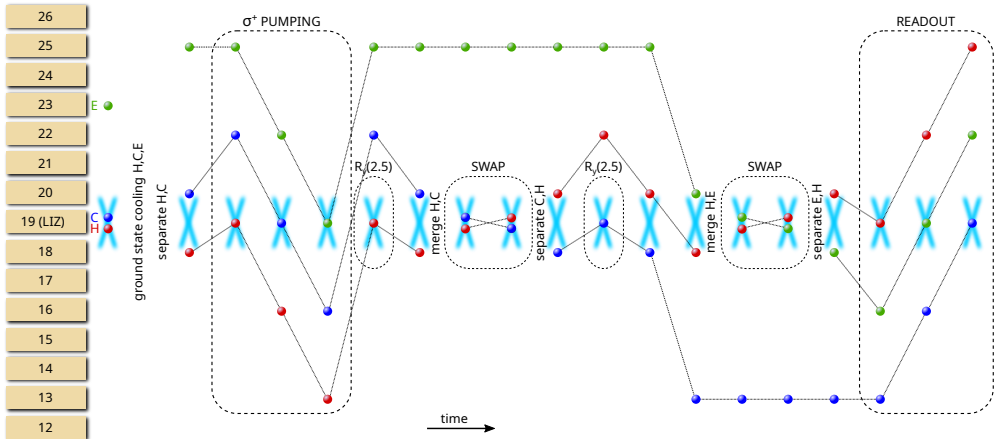


Figure 6.2: Experimental shuttling sequence that realizes the quantum circuit shown in Fig. 6.1. Movement of ions h (red), c (blue), e (green) is shown relative to trap segments 12-26 (goldbrown). All laser-driven operations are highlighted. The main elements of the quantum circuit are highlighted. The second SWAP gate is optional, which only changes the order of readout. The full sequence contains 21 qubit operations and 35 shuttling operations.

6.3 SWAP gate calibration

After daily calibrations (see Section 2.2), optical pumping for thermal state initialization is calibrated in the same manner as in Chapter 5, for the different spin temperatures shown in Table 6.1. The customized single qubit rotation about 2.5 rad is calibrated as follows: The population in $|0\rangle$ is measured after performing 10 identical Raman pulses with varying pulse duration. Using $2.5/\pi * 10 = 7.95775$, we calibrate to the pulse duration that results in 0.95775 $|0\rangle$ population, just before the 8th full state swap.

Extra attention is given to the calibration of the SWAP gate, as strong fluctuations on the populations have been observed directly after performing a SWAP gate. For the standard positional ion swap, there are several parameters to be calibrated, as explained in [Kau17b]. Various parameter sets were tested by measuring the excitation of all radial modes directly after a swap via red sideband probing [Goo16]. Much improvement was gained by calculating parameter sets for which the motional mode frequencies remain constant and well-separated during the swap [Hil22a]. Only the total duration is then left to be varied, and it was optimized to 60 μs . Finally, an attempt was made to replace the positional ion swap by a laser-driven swap. The quantum circuit is shown in Fig. 6.3. It was optimized for having the least amount of geometric phase gates possible while still only using global single qubit gates, such that the whole laser-driven swap can be performed on a two-ion crystal without any separate/merge operations. As this combination of single- and two-qubit gates will always have a nonzero probability for errors, the unit-fidelity positional ion swap is preferred. Both options were tried in the full passivity deformation circuit (Fig. 6.1). Results were varying, but overall, the agreement with theoretically calculated values was better for the positional ion swap. The final data was taken using the positional ion swap.

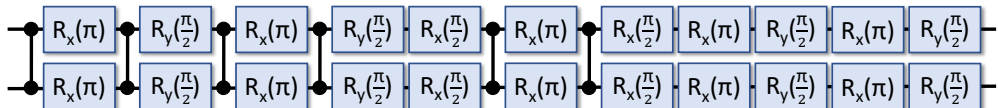


Figure 6.3: Quantum circuit for a laser-driven SWAP operation. The circuit is optimized to contain only global single qubit gates, such that no separate/merge operations are required [Hil22a]. The two-qubit light-shift gates have a phase $\Phi = \pi/4$.

6.4 Measurement and evaluation

The qubit readout and computation of $\Delta \langle \hat{B}^\alpha \rangle$ is performed identical to Chapter 5. However, this time we also compute both sides of the passivity deformation inequality Eq. 6.5. The results are shown in Fig. 6.4. For the case with final SWAP, we observe a clear violation of Eq. 6.5 for $\xi < -0.880(1)$, which is about 5.3 standard deviations above the bound ξ_m . From the evaluation of $\Delta \langle \hat{B}^\alpha \rangle$ on the measurement data with final SWAP, we find that global passivity fails to detect the heat leak for this scenario, as $\Delta \langle \hat{B}^\alpha \rangle \geq 0$ for any α . This demonstrates that passivity deformation based inequalities yield increased sensitivity to heat leaks as compared to global passivity.

In the last two chapters, we have demonstrated the relevance of passivity-based inequalities for detecting controllable heat leaks, i.e. the presence of measurable interactions with the environment. So far, these experiments show that passivity-based constraints are experimentally relevant and that they are more sensitive to heat leaks as compared to a microscopic form of the second law of thermodynamics.

One remark for these particular protocols could be that a full SWAP gate does not accurately reflect thermal interaction with an environment. Future versions of these experiments could aim at using periodically repeating protocols to amplify the effect of a heat leak and therefore increase the detection sensitivity, in order to detect genuine heat leaks rather than artificially introduced environments.

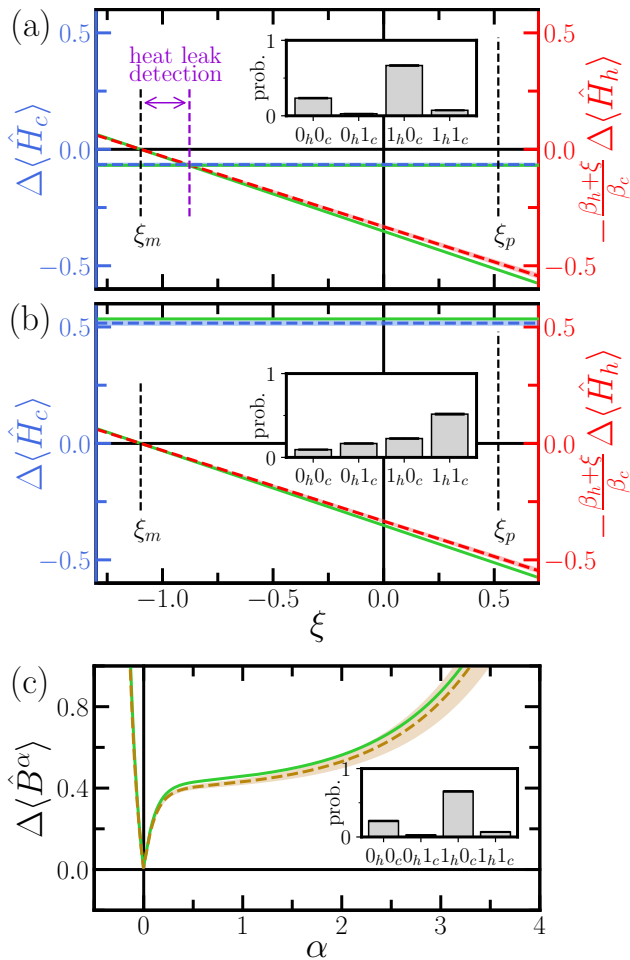


Figure 6.4: Results of the passivity deformation protocol, Fig. 6.1, 3200 repetitions: For varying ξ , we compare the energy change of the cold qubit (blue) to the rescaled energy change of the hot qubit (red) (left- and right-hand-sides of inequality 6.5). Panel (a) shows the scenario with SWAP gate, where we find a violation of inequality 6.5 for $\xi_m \leq \xi \leq -0.880(1)$ (purple arrow). Panel (b) shows the case without final SWAP gate, where no violation of Eq. 6.5 is observed. In panel (c), the difference in expectation values \hat{B}^α is calculated as a function of α , for the case with final SWAP gate. Inequality Eq. 5.4 is not violated, showing that the global passivity protocol alone does not detect the heat leak for this circuit. Experimental data (dashed) is compared to theoretical values (solid, green). The measured populations for system qubits h, c , from which the data is calculated, are shown as insets.

Chapter 7

Outlook - Periodicity Algorithms and a Quantum Heat Engine

In Chapter 5 we have seen how the framework of global passivity allows for detecting a heat leak, i.e. non-unital evolution of two system qubits, due to interaction with an environment qubit. The heat leak could be detected by measurements on the system qubits alone, and was not detected by a microscopic form of the second law of thermodynamics. Chapter 6 showed a case where a similar heat leak could not be detected by global passivity, but was detected by the more sensitive framework of passivity deformation. In the context of quantum computation, this shows the relevance of passivity-based inequalities for detection and classification of incoherent errors, which lead to non-unital evolution. However, there are a few limitations to the presented methods: Although these frameworks are agnostic to the particular unitary evolution, they require initially uncorrelated thermal states. As most quantum algorithms require pure initial states, benchmarking a system will still involve executing a separate protocol, which may or may not be tunable to reflect the performance of the specific algorithm at hand. Thus, these methods are more suitable for general system characterization than for individual algorithm optimization.

In the next years, experiments with more than 50 qubits are planned. Therefore, it is important to further develop benchmarking methods that scale more efficiently than e.g. tomography. We intend to conduct experiments in line with the following 3 ideas:

Initial correlations and pure states in passivity-based inequalities

Passivity-based inequalities allow for initial correlations and pure states to a certain degree. In [Uzd18b], the authors use passivity to derive an Initial Correlation Clausius Inequality:

$$\Delta S^{\text{sys}} + \Delta \langle \hat{B}^{\text{env}} \rangle + \Delta \langle \hat{B}^{\text{corr}} \rangle \geq 0, \quad (7.1)$$

where ΔS^{sys} is the change in the system entropy, $\Delta \langle \hat{B} \rangle$ is the change in the expectation value of observable \hat{B} (see Eq. 4.8), and \hat{B}^{corr} is defined as the difference between \hat{B}^{tot} and the sum of \hat{B}^{sys} and \hat{B}^{env} . This inequality is shown to correctly describe the unital evolution of an initially correlated system, and further experimental study is suggested. In [Uzd21], the authors show that passivity deformation can handle the ultracold limit as long as there is still a sufficient difference in temperature between subsystems, i.e. part of the system can be in a pure state. However, the authors also note that passivity deformation fails to detect any heat leaks above a certain environment temperature. On a sidenote, passivity-based inequalities can be used to set bounds on the evolution of certain observables. Fig. 7.1 shows an example for the covariance between the polarization of an initially coherent spin and the energy of a dephasing environment. Passivity deformation sets significantly tighter bounds.

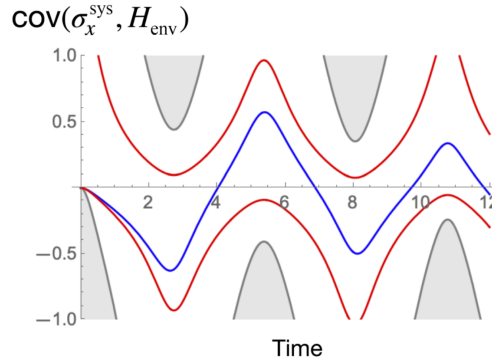


Figure 7.1: The dynamics of the normalized covariance between the polarization of an initially coherent spin σ_x^{sys} , and the energy of a dephasing environment composed of three thermal spins \hat{H}_{env} . The exact dynamics is shown in blue and the gray areas are the forbidden zones according to the global passivity bound $\Delta \langle \hat{B}^2 \rangle \geq 0$. Using the passivity deformation framework, we find significantly tighter bounds (red). Figure taken from [Uzd21].

Periodicity inequalities

Ultimately, any entropy-related inequality will have problems dealing with initial pure states. If the initial state is pure, the initial entropy is zero, and it is not possible to decrease it any further. Hence, the second law cannot be used to detect heat leaks for initial pure states. In general, finding constraints on observables undergoing unitary evolution without knowing anything about the dynamics is very difficult. The authors of [Pan] circumvent this problem by exploiting periodicity. They consider a periodically driven system undergoing unitary evolution, where each cycle consists of a certain unitary and its inverse. As in randomized benchmarking, the survival probability is the probability to return to the initial state. With R_n representing the survival probability after n cycles, they find general inequalities of the form

$$S_n = \sum_k w_k R_k \geq 0, \quad \text{with} \quad \sum_k w_k = 0 \quad \text{and} \quad \sum_k |w_k| = 1, \quad (7.2)$$

i.e. for n cycles, the corresponding inequality has alternating survival probability coefficients that add up to ± 0.5 . In the weak action limit (the survival probability decreases very slowly over many cycles), they predict exponential decay. This means that, using extrapolation, only $\pi\sqrt{n}$ points are needed to evaluate S_n , and more importantly, that the type of decay can classify the error mechanism as coherent or incoherent. Figure 7.2 illustrates this concept. This framework can be applied to any repeatable unitary circuit for which an inverse operation can be calculated, and is therefore well suited for both general system characterization and error classification in a specific algorithm. Note however that in the case of a deliberate heat leak introduction via coupling to an environment qubit, the authors were only able to detect the heat leak with a non-binary pure input state ($|+0\rangle$). With a clever choice of observables, this framework can also be used to locate the source of an incoherent error within a circuit [Uzd].

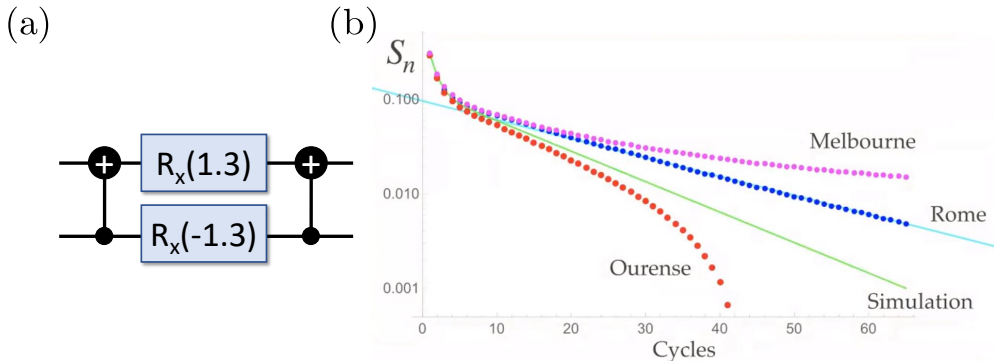


Figure 7.2: Application of the periodicity framework to a number of IBM quantum processors. (a) Periodic unitary circuit. (b) Weighted sum of survival probabilities S_n (Eq. 7.2) as a function of n cycles, for different processors. Violation of $S_n \geq 0$ indicates either nonperiodic or nonunitary evolution, and exponential decay is predicted. A heat leak is detected for the Ourense and Melbourne processors, by violation and nonexponential decay, respectively. The Rome processor does not show a heat leak, but follows a different exponential decay than the simulation, indicating a coherent error, e.g. due to miscalibration. Figure taken from [Uzd20].

Quantum Heat Engine

Making use of the excellent qualities such as fast thermal state preparation, the quantum processor described in Chapters 2 and 3 can also be employed to realize and explore quantum thermodynamics, in particular the dynamics of quantum heat engines. A single spin heat engine has been realized in a similar setup, where the work agent was a single ion's spin degree of freedom, the reservoirs were realized via optical pumping, and the ion's motional degree of freedom served as flywheel [Lin19]. The coupling between spin and motion was mediated by a phase-stable optical lattice, giving rise to spin dependent optical dipole forces [Sch16b]. This concept will be extended to a multi-particle interaction: Reservoirs H and C consist of small, extendable ion Coulomb crystals. Effective spin temperatures can be realized and maintained by optical pumping, as described in Section 2.1, thus emulating effective macro-reservoirs. Heat is transferred between reservoirs by dynamical crystal-reconfiguration and shuttling of work agent ion W , followed by laser-mediated spin-spin interaction, thus realizing e.g. $\sqrt[n]{SWAP}$ gates for heat transfer between either W and H or W and C . The state of the work ion can be reconstructed e.g. via quantum state tomography after a given number of operation cycles. Generated work will be extracted from the system ion W by interspersed coupling to yet another flywheel ion F . The concept is illustrated in Figure 7.3. This scheme will allow for investigating the buildup of non-classical correlations between

the reservoirs [Kha20], the implementation of optimal work extraction protocols, the study of work efficiency with micro versus macro reservoirs, and the investigation of generalized bounds of the efficiency in the regime of finite-time operations.

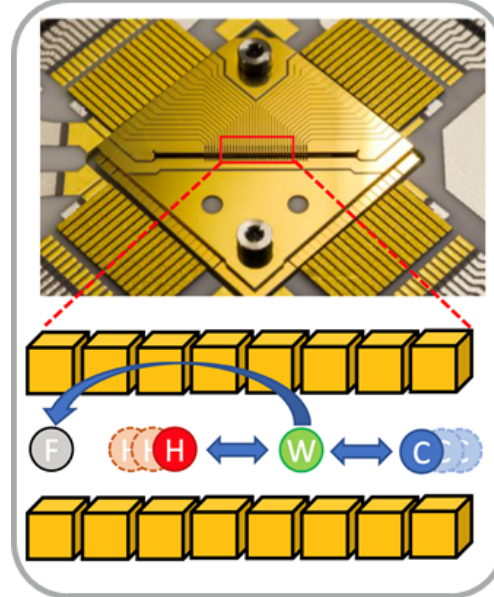


Figure 7.3: Ion spin heat engine with work mediating ion W, sequentially coupled to cold micro-reservoirs C and hot micro-reservoirs H, and flywheel ion F.

Appendix A

Raman laser intensity stabilization and beam distribution

A.1 Intensity stabilization

To drive high fidelity gates, the intensity of the laser driving the Raman transitions has to be stabilized on the timescale of typical gate pulses (1-100 μ s). This is done using a combination of a photodiode¹, a fast analog PID regulator² with a bandwidth of 1 MHz, and an electro-optical modulator³ (EOM). The setup is shown in Figure A.1. Directly after the laser⁴ output, the polarization is made linear and aligned to the EOM crystal axis by a $\lambda/4$ and $\lambda/2$ waveplate. After the EOM, a polarizing beamsplitter cube (PBS) splits off the fraction of vertically polarized light to a beam dump, such that the polarization change induced by the EOM is converted to an intensity change after the PBS. A $\lambda/2$ waveplate aligns the polarization with the slow axis of the fiber. Due to the high laser intensity at this position (100-400 mW), coupled with the strong optical tweezer effect for UV light, the probability for burning either the fiber tip or the fiber coupler lens is relatively high. A custom 3D-printed enclosure with included fan and air filter minimizes the amount of dust around the fiber coupler by keeping a slight overpressure in the enclosure at all times. Additionally, a glue-free coupler lens⁵ and a photonic-crystal fiber⁶ (PCF) with a large core diameter were used. Despite these measures, the coupling efficiency repeatedly degraded over a timespan of several weeks. This was solved by either exchanging the coupler, or lightly

¹ Thorlabs PDA8A/M

² NoiseEater 3V0, TEM Messtechnik

³ Linos LM 0202 P 5W KD*P 3x3 mm

⁴ 397 nm TA-SHG Pro, Toptica Photonics AG

⁵ 60FC-4-A15-01, Schäfter + Kirchhoff GmbH

⁶ LMA-PM-5, NKT Photonics

polishing the fiber tip, depending on where the burn had occurred. At the fiber output, the beam is collimated⁷ to a $1/e^2$ diameter of ~ 1.2 mm. A PBS is used to convert polarization drifts to intensity drifts, after which the transmission of a mirror⁸ ($\sim 0.1\%$) is measured by the photodiode. The signal is amplified by a custom-made fast amplifier to a range of several volts, and compared to an externally supplied⁹ setpoint by the PID regulator. The feedback signal is amplified¹⁰ and connected to the EOM. This setup compensates for intensity and polarization fluctuations up to the photodiode. Therefore, it is crucial that the successive beam distribution setup is highly stable. A second intensity stabilization, with the intensity measured on the photodiodes¹¹ in the μ -metal enclosure, and regulated on the rf amplitude driving the AOM for each beam, is planned for the near future.

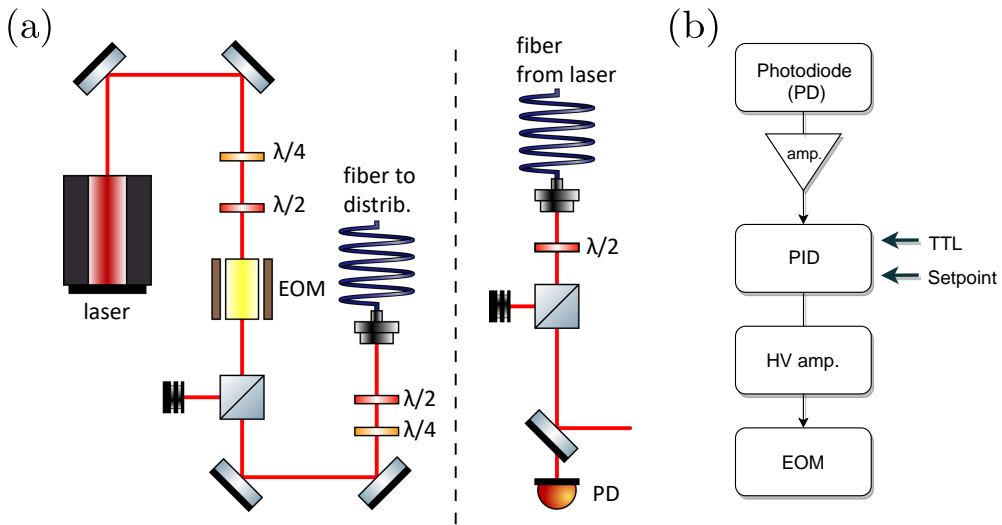


Figure A.1: Raman intensity stabilization. (a) The light is first guided through an EOM and a PBS. The function of the PBS is to convert EOM-induced polarization changes to intensity changes. After the fiber, the horizontally polarized component is partially picked off on a PD. (b) The signal from the PD is amplified and processed by a PID regulator, which acts on the EOM after high voltage amplification. The regulation bandwidth is 1 MHz, set by the PID regulator.

⁷ 60FC-4-A6.2S-01, Schäfter + Kirchhoff GmbH

⁸ Laseroptik HR370-430nm L-13519

⁹ Keysight E3648A

¹⁰ HighVoltageAmplifier-Fast, TEM Messtechnik

¹¹ Thorlabs SM05PD1A

A.2 Beam distribution

The four beams discussed in Sec. 3.4 (R1, CC, R4, R2) require fast switching, phase-coherent switching between frequencies, and relative phase stability. This is accomplished by two DDS-based frequency sources: a versatile frequency generator¹² (VFG) and a continuously running single-frequency function generator¹³ are driving the AOMs of each beam pair. An rf switch¹⁴ network, shown in Figure A.2, connects the rf sources to the appropriate AOMs¹⁵, such that R2 and R4 are always driven at 110 MHz, whereas the frequency for R1 or CC can be modified according to the desired interaction. The VFG allows for shaped pulses, i.e. amplitude-modulated rf pulses, while the function generator is switched in a rectangular fashion. A separate double pass AOM setup driving 729 nm pulses (not shown in Figure A.3) is also driven by the VFG, to allow for shaped and chirped shelving pulses (see Fig. 2.5). Each rf output is connected to a water-cooled amplifier¹⁶ after being tuned by attenuators¹⁷ to reach the nominal power of 2 or 3 W for each AOM. Near the end of the work for this thesis, an advanced four-channel HDAWG¹⁸ was partially integrated in the setup to provide shaped pulses to all AOMs. Eventually, the four channels of the HDAWG may be used to supply all AOMS directly, without requiring switches. Using low-latency communication, the HDAWG may also be used to implement in-sequence feedback for error correction.

The optical setup is shown in Fig. A.3. The design is based on a previous version, discussed in [Not17, Kau17a], with several fundamental changes. The previous version focused the beams down to $\sim 100 \mu\text{m}$ in the AOMs for fast switching times, and attempted to approach equal path lengths to minimize interferometric effects. This version uses collimated beams to maximize AOM efficiency, and minimizes path lengths for optimal fiber coupling stability. The $1/e^2$ beam diameter is $\sim 1.2 \text{ mm}$. The $\lambda/2$ waveplate before each PBS determines the fraction of power that is diverted to the respective AOM. The effective intensity of each beam on the ion is equalized by measuring the Stark shift induced phase accumulation during a Ramsey measurement

¹² VFG-150, Toptica Photonics AG

¹³ Rohde & Schwarz SML01

¹⁴ Mini-Circuits ZYSW-2-50DR

¹⁵ I-M095-3C10BB-3-GH27, I-M110-2C10BB-3-GH27, I-M110-3C10BB-3-GH27, each manufactured by Gooch & Housego

¹⁶ Mini-Circuits ZHL-5W-1

¹⁷ Mini-Circuits ZX73-2500+

¹⁸ HDAWG, Zurich Instruments AG

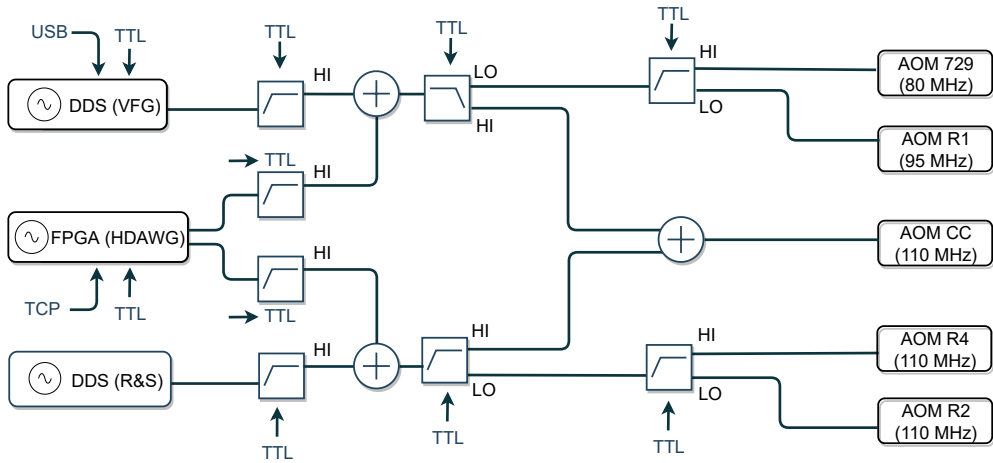


Figure A.2: AOM drive rf switch network. For all experiments in this thesis, the rf signals for each Raman beam pair are supplied by a preprogrammed VFG and a continuously running DDS at 110 MHz. The TTLs are reconfigured within measurement sequences to guide the rf signals to the desired AOMs for each pulse. The VFG provides shaped and frequency-modulated pulses which only need to be triggered by a TTL, while the DDS pulses are switched in a rectangular fashion by an rf switch. The recently integrated HDAWG may provide shaped pulses to both beams and thereby reduce spectator mode excitation for the light-shift gate (Sec. 2.2).

on a $4S_{1/2} \leftrightarrow 3D_{5/2}$ transition [Pos10]. The AOMs are passively cooled by heatsinks to reduce warmup effects. For more stability, the duty cycle could be increased to 100%, and switching could be performed by changing the rf frequency to far from the specified AOM center frequency. After the AOMs, the +1 diffraction order light is coupled into fibers¹⁹ and guided to the μ -metal enclosure. A total decrease in power transfer efficiency around the AOM center frequency, up to the photodiode in the μ -metal enclosure, of 0.91(4) per MHz has been measured. AOM diffraction efficiencies are typically $>85\%$ with this beam diameter. Switching times are ~ 600 ns.

¹⁹ PMC-E-400Si-2.3-NA014-3-APC.EC/OPC, Schäfter + Kirchhoff GmbH

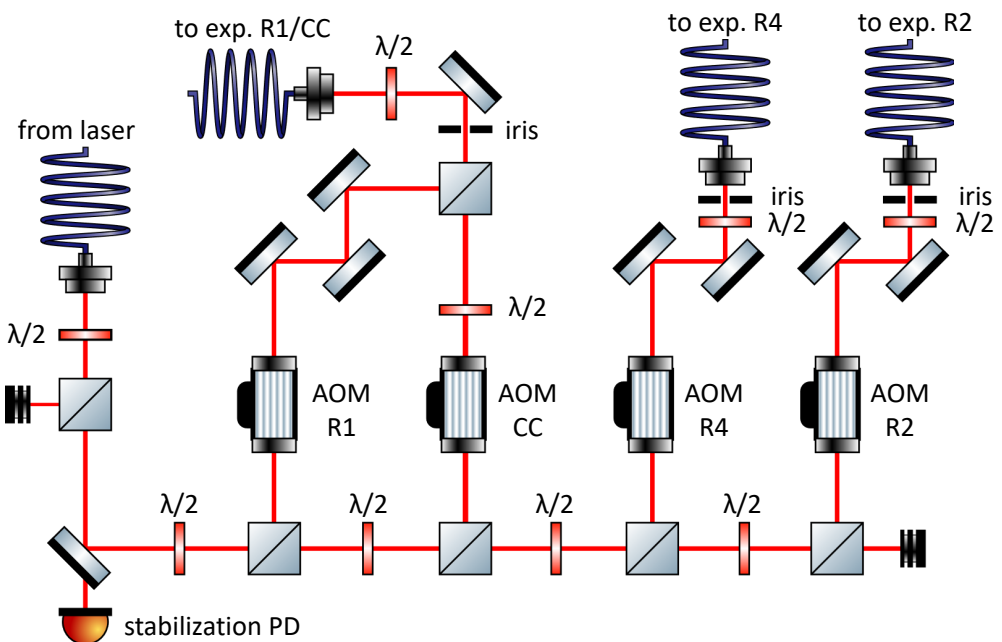


Figure A.3: Raman beam distribution. The light is first filtered by a PBS. 0.1% is transmitted by the first mirror and used for intensity stabilization (Sec. A.1). The rest of the light is distributed over four AOMs to control the phase, frequency, and intensity of each Raman beam (Fig. 3.11) individually. This setup was optimized for stability through minimal path length, and high AOM efficiency through collimated beams.

Appendix B

729 high finesse locking setup

The 729 nm laser is generated by a prototype TA Pro¹, which contains an intra-cavity EOM with a bandwidth of 50 MHz for fast locking. To avoid servo bumps, and to make the optical path as short as possible, light from the laser probe output is used for locking. The probe output is coming from a beam pick-off between the diode output and the tapered amplifier input. The Fabry-Pérot locking cavity² is made from ultra-low expansion (ULE) material, which is temperature-stabilized to the zero-expansion point to minimize drift. The cavity has a finesse of 140 000 [Mac12]. Due to the large free spectral range of about 1.5 GHz, an AOM³ is used to shift the laser frequency by 409 MHz, to the nearest cavity resonance. The cavity and surrounding optics, shown in Fig. B.1a, are mounted on a vibration-isolation stage⁴. As part of the Pound-Drever-Hall (PDH) locking technique [Bla01], a self-made EOM modulates the light at 35.38 MHz. The cavity-reflected light is sent to a fast photodiode⁵ and used to generate an error signal, while the cavity transmission is observed on a regular photodiode⁶ and a webcam⁷ to monitor the lock status. The locking electronics, shown in Fig. B.1b, are chosen to generate an optimal PDH error signal for the Fast Analog Linewidth Control (FALC) module⁸. This module contains two circuit branches, a fast branch is acting on the intra-cavity EOM, and a low-speed integrating amplifier is compensating for slow drifts by acting on the piezo voltage. For this complete setup, the resulting laser linewidth is estimated at \sim 500 Hz, and the typical slow drift due to cavity temperature fluctuations is 1.43 kHz/day.

¹ Toptica Photonics AG

² ATF 6020 notched cavity, Stable Laser Systems

³ MT405-B20A0.2-800, AA Opto Electronic

⁴ Micro 40, Accurion GmbH

⁵ DC-125 MHz Low Noise Photoreceiver, Model 1801 New Focus

⁶ Thorlabs PDA8A/M

⁷ VC2PMA, Conrad GmbH

⁸ FALC 110, Toptica Photonics AG

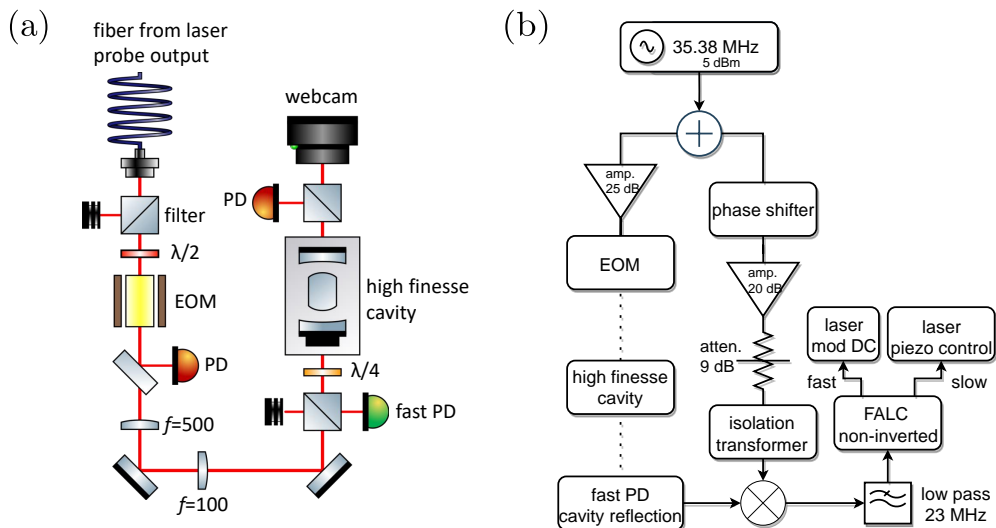


Figure B.1: High finesse locking setup. (a) Optical setup around the cavity. The probe output is used to minimize the optical path length. An EOM induced sidebands at 35.38 MHz. The beam diameter is optimized for the cavity. The cavity reflection is captured on a fast PD. The other PDs and webcam are for monitoring intensity and lock status. (b) Locking electronics, optimized for the Toptica FALC module. The signal from a local oscillator is sent to the EOM to produce sidebands, as well as to a mixer, where it is mixed with the cavity reflection to generate a Pound-Drever-Hall error signal. The FALC module locks the laser via a fast circuit branch, and corrects for slow drifts via a slow circuit branch.

Bibliography

[Aar04] S. Aaronson and D. Gottesman, *Improved simulation of stabilizer circuits*, Physical Review A **70** (2004) (cit. on p. 33).

[Ací18] A. Acín, I. Bloch, H. Buhrman, T. Calarco, C. Eichler, J. Eisert, D. Esteve, N. Gisin, S. J. Glaser, F. Jelezko, S. Kuhr, M. Lewenstein, M. F. Riedel, P. O. Schmidt, R. Thew, A. Wallraff, I. Walmsley, and F. K. Wilhelm, *The quantum technologies roadmap: a European community view*, New Journal of Physics **20**, 080201 (2018) (cit. on p. 2).

[Aha08] D. Aharonov and M. Ben-Or, *Fault-Tolerant Quantum Computation with Constant Error Rate*, SIAM Journal on Computing **38**, 1207 (2008) (cit. on p. 2).

[All04] A. E. Allahverdyan, R. Balian, and T. M. Nieuwenhuizen, *Maximal work extraction from finite quantum systems*, Europhysics Letters (EPL) **67**, 565 (2004) (cit. on p. 4).

[Ari76] E. Arimondo and G. Orriols, *Nonabsorbing atomic coherences by coherent two-photon transitions in a three-level optical pumping*, Lettere Al Nuovo Cimento Series 2 **17**, 333 (1976) (cit. on p. 14).

[Bal14] C. J. Ballance, *High-Fidelity Quantum Logic in Ca+*, Ph.D. thesis, University of Oxford (2014) (cit. on pp. 8, 23, 24, 25).

[Bal16] H. Ball, T. M. Stace, S. T. Flammia, and M. J. Biercuk, *Effect of noise correlations on randomized benchmarking*, Physical Review A **93** (2016) (cit. on p. 33).

[Bal20] C. H. Baldwin, B. J. Bjork, J. P. Gaebler, D. Hayes, and D. Stack, *Subspace benchmarking high-fidelity entangling operations with trapped ions*, Physical Review Research **2** (2020) (cit. on p. 33).

[Ber12a] A. Bermudez, J. Almeida, K. Ott, H. Kaufmann, S. Ulm, U. Poschinger, F. Schmidt-Kaler, A. Retzker, and M. B Plenio, *Quantum magnetism of spin-ladder compounds with trapped-ion crystals*, New Journal of Physics **14**, 093042 (2012) (cit. on p. 11).

[Ber12b] A. Bermudez, P. O. Schmidt, M. B. Plenio, and A. Retzker, *Robust trapped-ion quantum logic gates by continuous dynamical decoupling*, Physical Review A **85** (2012) (cit. on p. 20).

[Ber17] A. Bermudez, X. Xu, R. Nigmatullin, J. O’Gorman, V. Negnevitsky, P. SCHINDLER, T. MONZ, U. G. Poschinger, C. Hempel, J. Home, F. Schmidt-Kaler, M. Biercuk, R. Blatt, S. Benjamin, and M. Müller, *Assessing the Progress of Trapped-Ion Processors Towards Fault-Tolerant Quantum Computation*, Physical Review X **7** (2017) (cit. on p. 37).

[Bin18] F. Binder, L. A. e. Correa, C. Gogolin, J. Anders, and G. Adesso (Eds.), *Thermodynamics in the quantum regime: Fundamental aspects and new directions / Felix Binder, Luis A. Correa, Christian Gogolin, Janet Anders, Gerardo Adesso, editors*, Fundamental Theories of Physics, Springer, Cham, Switzerland, 2018 (cit. on p. 4).

[Bla01] E. D. Black, *An introduction to Pound–Drever–Hall laser frequency stabilization*, American Journal of Physics **69**, 79 (2001) (cit. on pp. 58, 103).

[Bra05] S. Bravyi and A. Kitaev, *Universal quantum computation with ideal Clifford gates and noisy ancillas*, Physical Review A **71** (2005) (cit. on p. 33).

[Buf20] L. Buffoni and M. Campisi, *Thermodynamics of a quantum annealer*, Quantum Science and Technology **5**, 035013 (2020) (cit. on p. 4).

[Cam11] M. Campisi, P. Hänggi, and P. Talkner, *Colloquium : Quantum fluctuation relations: Foundations and applications*, Reviews of Modern Physics **83**, 771 (2011) (cit. on p. 4).

[Che20] H.-P. Cheng, E. Deumens, J. K. Freericks, C. Li, and B. A. Sanders, *Application of Quantum Computing to Biochemical Systems: A Look to the Future*, Frontiers in chemistry **8**, 587143 (2020) (cit. on p. 2).

[Cir95] Cirac and Zoller, *Quantum Computations with Cold Trapped Ions*, Physical review letters **74**, 4091 (1995) (cit. on pp. 2, 20).

[Cla65] R. Clausius, *Ueber verschiedene für die Anwendung bequeme Formen der Hauptgleichungen der mechanischen Wärmetheorie*, Annalen der Physik und Chemie **201**, 353 (1865) (cit. on pp. 4, 66).

[Con21] A. A. Conta, *Software Framework for Automated Optimization of Operational Blocks of a Trapped-Ion-Based Quantum Computer*, Bachelor thesis, University of Mainz (2021) (cit. on p. 16).

[Cot17] N. Cottet, S. Jezouin, L. Bretheau, P. Campagne-Ibarcq, Q. Ficheux, J. Anders, A. Auffèves, R. Azouit, P. Rouchon, and B. Huard, *Observing a quantum Maxwell demon at work*, Proceedings of the National Academy of Sciences of the United States of America **114**, 7561 (2017) (cit. on p. 4).

[Dan21] R. Dann and R. Kosloff, *Open system dynamics from thermodynamic compatibility*, Physical Review Research **3** (2021) (cit. on pp. 65, 67).

[Dav76] E. B. Davies, *Quantum theory of open systems*, Academic Press, London, 1976 (cit. on pp. 65, 67).

[Deh68] H. G. Dehmelt, *Radiofrequency Spectroscopy of Stored Ions I: Storage*, in: *Advances in Atomic and Molecular Physics Volume 3*, vol. 3 of *Advances in Atomic and Molecular Physics*, 53–72, Elsevier, 1968 (cit. on p. 10).

[Deu85] D. Deutsch, *Quantum theory, the Church–Turing principle and the universal quantum computer*, Proceedings of the Royal Society of London. A. Mathematical and Physical Sciences **400**, 97 (1985) (cit. on p. 1).

[Deu89] D. Deutsch, *Quantum computational networks*, Proceedings of the Royal Society of London. A. Mathematical and Physical Sciences **425**, 73 (1989) (cit. on p. 1).

[Deu92] D. Deutsch, *Rapid solution of problems by quantum computation*, Proceedings of the Royal Society of London. A. Mathematical and Physical Sciences **439**, 553 (1992) (cit. on p. 1).

[Dil14] M. Dillmann, *Stabilisierung der radialen Säkularfrequenzen gefangener Ionen in einer segmentierten Paul-Falle*, Diploma thesis, University of Mainz (2014) (cit. on pp. 42, 43).

[DiV00] D. P. DiVincenzo, *The Physical Implementation of Quantum Computation*, Fortschritte der Physik **48**, 771 (2000) (cit. on p. 2).

[Dow03] J. P. Dowling and G. J. Milburn, *Quantum technology: the second quantum revolution*, Philosophical transactions. Series A, Mathematical, physical, and engineering sciences **361**, 1655 (2003) (cit. on p. 2).

[Eke94] A. Ekert, *Quantum Computation*, in: *AIP Conference Proceedings 14*, vol. 323, 450–466, AIP, 1994 (cit. on p. 1).

[Eke96] A. Ekert and R. Jozsa, *Quantum computation and Shor's factoring algorithm*, Reviews of Modern Physics **68**, 733 (1996) (cit. on p. 2).

[Emm75] B. Emmoth, M. Braun, J. Bromander, and I. Martinson, *Lifetimes of Excited Levels in Ca I-Ca III*, Physica Scripta **12**, 75 (1975) (cit. on p. 8).

[Erh19] A. Erhard, J. J. Wallman, L. Postler, M. Meth, R. Stricker, E. A. Martinez, P. Schindler, T. Monz, J. Emerson, and R. Blatt, *Characterizing large-scale quantum computers via cycle benchmarking*, Nature communications **10**, 5347 (2019) (cit. on p. 33).

[Fey60] R. P. Feynman, *There's Plenty of Room at the Bottom*, Engineering and Science **23**, 22 (1960) (cit. on p. 1).

[Fey63] R. Feynman and F. Vernon, *The theory of a general quantum system interacting with a linear dissipative system*, Annals of Physics **24**, 118 (1963) (cit. on p. 65).

[Fey82] R. P. Feynman, *Simulating physics with computers*, International Journal of Theoretical Physics **21**, 467 (1982) (cit. on pp. 1, 3).

[Fey86] R. P. Feynman, *Quantum mechanical computers*, Foundations of Physics **16**, 507 (1986) (cit. on p. 1).

[Gev96] E. Geva and R. Kosloff, *The quantum heat engine and heat pump: An irreversible thermodynamic analysis of the three-level amplifier*, The Journal of Chemical Physics **104**, 7681 (1996) (cit. on p. 4).

[Gil22] S. S. Gill, A. Kumar, H. Singh, M. Singh, K. Kaur, M. Usman, and R. Buyya, *Quantum computing: A taxonomy, systematic review and future directions*, Software: Practice and Experience **52**, 66 (2022) (cit. on p. 2).

[Goo16] J. F. Goodwin, G. Stutter, R. C. Thompson, and D. M. Segal, *Resolved-Sideband Laser Cooling in a Penning Trap*, Physical Review Letters **116**, 143002 (2016) (cit. on p. 88).

[Got98] D. Gottesman, *The Heisenberg representation of quantum computers*, Conference (1998) (cit. on p. 33).

[Gou15] G. Gour, M. P. Müller, V. Narasimhachar, R. W. Spekkens, and N. Yunger Halpern, *The resource theory of informational nonequilibrium in thermodynamics*, Physics Reports **583**, 1 (2015) (cit. on p. 4).

[GR03] J. J. García-Ripoll, P. Zoller, and J. I. Cirac, *Speed optimized two-qubit gates with laser coherent control techniques for ion trap quantum computing*, Physical review letters **91**, 157901 (2003) (cit. on p. 20).

[Gre] D. Greenbaum, *Introduction to Quantum Gate Set Tomography* (cit. on p. 3).

- [Gri13] D. J. Griffiths, *Revolutions in twentieth-century physics*, Cambridge University Press, Cambridge, UK, 2013 (cit. on p. 1).
- [Gro96] L. K. Grover, *A fast quantum mechanical algorithm for database search*, in: G. L. Miller (Ed.), *Proceedings of the twenty-eighth annual ACM symposium on the theory of computing*, 212–219, ACM Press, New York, New York, USA, 1996 (cit. on p. 1).
- [Har96] S. Haroche and J.-M. Raimond, *Quantum Computing: Dream or Nightmare?*, Physics Today **49**, 51 (1996) (cit. on p. 2).
- [Har13] T. P. Harty, *High-fidelity microwave-driven quantum logic in intermediate-field 43Ca+*, Ph.D. thesis, University of Oxford (2013) (cit. on p. 14).
- [Het15] M. Hettrich, T. Ruster, H. Kaufmann, C. F. ROOS, C. T. Schmiegelow, F. Schmidt-Kaler, and U. G. Poschinger, *Measurement of Dipole Matrix Elements with a Single Trapped Ion*, Physical Review Letters **115**, 143003 (2015) (cit. on pp. 8, 9).
- [Hil22a] J. Hilder, *Fault-tolerant quantum error correction with trapped-ion quantum bits*, Phd, University of Mainz (2022) (cit. on pp. 44, 63, 80, 88).
- [Hil22b] J. Hilder, D. Pijn, O. Onishchenko, A. Stahl, M. Orth, B. Lekitsch, A. Rodriguez-Blanco, M. Müller, F. Schmidt-Kaler, and U. G. Poschinger, *Fault-Tolerant Parity Readout on a Shuttling-Based Trapped-Ion Quantum Computer*, Physical Review X **12** (2022) (cit. on pp. 3, 51).
- [Hyn06] R. J. Hyndman and A. B. Koehler, *Another look at measures of forecast accuracy*, International Journal of Forecasting **22**, 679 (2006) (cit. on p. 78).
- [Jae18] L. Jaeger, *The Second Quantum Revolution: From Entanglement to Quantum Computing and Other Super-Technologies / Lars Jaeger*, Springer, Cham, Switzerland, 2018 (cit. on p. 2).
- [Jam98] D. James, *Quantum dynamics of cold trapped ions with application to quantum computation*, Applied Physics B **66**, 181 (1998) (cit. on p. 13).
- [Jin93] Jin and Church, *Precision lifetimes for the Ca+ 4p 2P levels: Experiment challenges theory at the 1% level*, Physical Review Letters **70**, 3213 (1993) (cit. on pp. 8, 15, 16).
- [Jon00] D. Jonathan, M. B. Plenio, and P. L. Knight, *Fast quantum gates for cold trapped ions*, Physical Review A **62** (2000) (cit. on p. 20).
- [Kau14] H. Kaufmann, T. Ruster, C. T. Schmiegelow, F. Schmidt-Kaler, and U. G. Poschinger, *Dynamics and control of fast ion crystal splitting in segmented Paul traps*, New Journal of Physics **16**, 073012 (2014) (cit. on p. 76).
- [Kau17a] H. Kaufmann, *A Scalable Quantum Processor*, Phd, University of Mainz (2017) (cit. on pp. 39, 40, 42, 43, 46, 57, 99).
- [Kau17b] H. Kaufmann, T. Ruster, C. T. Schmiegelow, M. A. Luda, V. Kaushal, J. Schulz, D. von Lindenfels, F. Schmidt-Kaler, and U. G. Poschinger, *Fast ion swapping for quantum-information processing*, Physical Review A **95** (2017) (cit. on pp. 31, 45, 75, 76, 88).
- [Kau17c] H. Kaufmann, T. Ruster, C. T. Schmiegelow, M. A. Luda, V. Kaushal, J. Schulz, D. von Lindenfels, F. Schmidt-Kaler, and U. G. Poschinger, *Scalable Creation of Long-Lived Multipartite Entanglement*, Physical Review Letters **119**, 150503 (2017) (cit. on pp. 31, 46, 51).

[Kau19] V. Kaushal, *A shuttling-based trapped-ion quantum processing node*, Phd, University of Mainz (2019) (cit. on pp. 39, 45, 46, 47, 48, 61).

[Kau20] V. Kaushal, B. Lekitsch, A. Stahl, J. Hilder, D. Pijn, C. Schmiegelow, A. Bermudez, M. Müller, F. Schmidt-Kaler, and U. Poschinger, *Shuttling-based trapped-ion quantum information processing*, AVS Quantum Science **2**, 014101 (2020) (cit. on pp. 45, 61).

[Kes12] A. Kesser, *Aufbau einer Mikro-Ionenfalle mit langer Qubit-Kohärenzzeit*, Diploma thesis, University of Mainz (2012) (cit. on pp. 42, 46, 51).

[Key02] M. Keyl, *Fundamentals of quantum information theory*, Physics Reports **369**, 431 (2002) (cit. on pp. 65, 67).

[Kha20] S. Khandelwal, N. Palazzo, N. Brunner, and G. Haack, *Critical heat current for operating an entanglement engine*, New Journal of Physics **22**, 073039 (2020) (cit. on p. 95).

[Kie02] D. Kielpinski, C. Monroe, and D. J. Wineland, *Architecture for a large-scale ion-trap quantum computer*, Nature **417**, 709 (2002) (cit. on p. 44).

[Kla19] J. Klatzow, J. N. Becker, P. M. Ledingham, C. Weinzel, K. T. Kaczmarek, D. J. Saunders, J. Nunn, I. A. Walmsley, R. Uzdin, and E. Poem, *Experimental Demonstration of Quantum Effects in the Operation of Microscopic Heat Engines*, Physical Review Letters **122**, 110601 (2019) (cit. on p. 4).

[Kni05] E. Knill, *Quantum computing with realistically noisy devices*, Nature **434**, 39 (2005) (cit. on p. 33).

[Kni08] E. Knill, D. Leibfried, R. Reichle, J. Britton, R. B. Blakestad, J. D. Jost, C. Langer, R. Ozeri, S. Seidelin, and D. J. Wineland, *Randomized benchmarking of quantum gates*, Physical Review A **77** (2008) (cit. on p. 32).

[Kos14] R. Kosloff and A. Levy, *Quantum heat engines and refrigerators: continuous devices*, Annual review of physical chemistry **65**, 365 (2014) (cit. on p. 4).

[Kra99] H. Kragh, *Quantum generations: A history of physics in the twentieth century / Helge Kragh*, Princeton paperbacks, Princeton University Press, Princeton, N.J. and Chichester, 1999, 5th ed. (cit. on p. 1).

[Kre05] A. Kreuter, C. Becher, G. P. T. Lancaster, A. B. Mundt, C. Russo, H. Häffner, C. ROOS, W. Hänsel, F. Schmidt-Kaler, R. Blatt, and M. S. Safronova, *Experimental and theoretical study of the 3dD2 -level lifetimes of Ca+40*, Physical Review A **71** (2005) (cit. on pp. 8, 9).

[Lan21] G. T. Landi and M. Paternostro, *Irreversible entropy production: From classical to quantum*, Reviews of Modern Physics **93** (2021) (cit. on p. 4).

[Lee05] P. J. Lee, K.-A. Brickman, L. Deslauriers, P. C. Haljan, L.-M. Duan, and C. Monroe, *Phase control of trapped ion quantum gates*, Journal of Optics B: Quantum and Semiclassical Optics **7**, S371 (2005) (cit. on p. 21).

[Lei00] D. Leibfried, *Experiments towards quantum information with trapped Calcium ions*, in: *AIP Conference Proceedings*, 130–142, AIP, 4-9 June 2000 (cit. on p. 14).

[Lei03a] D. Leibfried, R. Blatt, C. Monroe, and D. Wineland, *Quantum dynamics of single trapped ions*, Reviews of Modern Physics **75**, 281 (2003) (cit. on pp. 7, 12, 14, 18, 23).

[Lei03b] D. Leibfried, B. DeMarco, V. Meyer, D. Lucas, M. Barrett, J. Britton, W. M. Itano, B. Jelenković, C. Langer, T. Rosenband, and D. J. Wineland, *Experimental demonstration of a robust, high-fidelity geometric two ion-qubit phase gate*, Nature **422**, 412 (2003) (cit. on p. 20).

[Lin19] D. von Lindenfels, O. Gräß, C. T. Schmiegelow, V. Kaushal, J. Schulz, M. T. Mitchison, J. Goold, F. Schmidt-Kaler, and U. G. Poschinger, *Spin Heat Engine Coupled to a Harmonic-Oscillator Flywheel*, Physical Review Letters **123**, 080602 (2019) (cit. on pp. 4, 94).

[Los19] M. Lostaglio, *An introductory review of the resource theory approach to thermodynamics*, Reports on progress in physics. Physical Society (Great Britain) **82**, 114001 (2019) (cit. on p. 4).

[Lvo09] A. I. Lvovsky and M. G. Raymer, *Continuous-variable optical quantum-state tomography*, Reviews of Modern Physics **81**, 299 (2009) (cit. on pp. 5, 31).

[Mac12] T. Macha, *Frequenzstabilisierung eines Titan-Saphir-Lasers und Verbesserung von Qubits mit Ca+-Ionen*, Diplom, University of Mainz (2012) (cit. on pp. 60, 103).

[Mal01] V. S. Malinovsky and J. L. Krause, *General theory of population transfer by adiabatic rapid passage with intense, chirped laser pulses*, The European Physical Journal D **14**, 147 (2001) (cit. on p. 19).

[Man80] Y. I. Manin, *Quantum mechanical computers* (1980) (cit. on p. 1).

[Man99] Y. I. Manin (Ed.), *Classical computing, quantum computing, and Shor's factoring algorithm*, 1999 (cit. on p. 1).

[Mar94] Marzoli, Cirac, Blatt, and Zoller, *Laser cooling of trapped three-level ions: Designing two-level systems for sideband cooling*, Physical Review A **49**, 2771 (1994) (cit. on p. 14).

[Mas19] G. Maslennikov, S. Ding, R. Hablützel, J. Gan, A. Roulet, S. Nimmrichter, J. Dai, V. Scarani, and D. Matsukevich, *Quantum absorption refrigerator with trapped ions*, Nature communications **10**, 202 (2019) (cit. on p. 4).

[Men09] C. B. Mendl and M. M. Wolf, *Unitary Quantum Channels – Convex Structure and Revivals of Birkhoff's Theorem*, Communications in Mathematical Physics **289**, 1057 (2009) (cit. on p. 67).

[Moh08] M. Mohseni, A. T. Rezakhani, and D. A. Lidar, *Quantum-process tomography: Resource analysis of different strategies*, Physical Review A **77** (2008) (cit. on p. 5).

[Mon95] Monroe, Meekhof, King, Jefferts, Itano, Wineland, and Gould, *Resolved-sideband Raman cooling of a bound atom to the 3D zero-point energy*, Physical review letters **75**, 4011 (1995) (cit. on p. 18).

[Mon16] A. Montanaro, *Quantum algorithms: an overview*, npj Quantum Information **2** (2016) (cit. on p. 2).

[Nag86] Nagourney, Sandberg, and Dehmelt, *Shelved optical electron amplifier: Observation of quantum jumps*, Physical Review Letters **56**, 2797 (1986) (cit. on p. 19).

[Nel65] J. A. Nelder and R. Mead, *A Simplex Method for Function Minimization*, The Computer Journal **7**, 308 (1965) (cit. on p. 16).

[Nic17] J. Nicodemus, *Automated Positioning Control for Trapped-Ion Quantum Registers*, M. sc. thesis, University of Mainz (2017) (cit. on pp. 47, 48).

[Nie10] M. A. Nielsen and I. L. Chuang, *Quantum computation and quantum information*, Cambridge University Press, Cambridge, 2010, 10th ed. (cit. on pp. 2, 17, 75).

[Nig14] D. Nigg, M. Müller, E. A. Martinez, P. SCHINDLER, M. Hennrich, T. MONZ, M. A. Martin-Delgado, and R. Blatt, *Quantum computations on a topologically encoded qubit*, *Science* **345**, 302 (2014) (cit. on p. 2).

[Not17] J. Nothhelfer, *Optikaufbau zum Treiben stimulierter Ramanübergänge*, B.sc. thesis, University of Mainz (2017) (cit. on p. 99).

[Ort21] M. Orth, *Advanced Ion Shuttling Operations for Scalable Quantum Computing*, Master thesis, University of Mainz (2021) (cit. on pp. 45, 54).

[Pan] T. Pandit, A. M. Green, C. H. Alderete, N. M. Linke, and R. Uzdin, *Bounds on the survival probability in periodically driven quantum systems* (cit. on p. 93).

[Pau53] W. Paul and H. Steinwedel, *Notizen: Ein neues Massenspektrometer ohne Magnetfeld*, *Zeitschrift für Naturforschung A* **8**, 448 (1953) (cit. on p. 10).

[Per02] A. Peres, *Quantum Theory: Concepts and Methods*, vol. 57 of *Springer eBook Collection*, Springer Netherlands, Dordrecht, 2002, 1st ed. (cit. on p. 66).

[Pij22] D. Pijn, O. Onishchenko, J. Hilder, U. G. Poschinger, F. Schmidt-Kaler, and R. Uzdin, *Detecting Heat Leaks with Trapped Ion Qubits*, *Physical Review Letters* **128** (2022) (cit. on p. 6).

[Pos10] U. G. Poschinger, *Quantum Optics Experiments in a Microstructured Ion Trap*, Dissertation, University of Mainz (2010) (cit. on pp. 13, 14, 18, 19, 29, 40, 100).

[Pus78] W. Pusz and S. L. Woronowicz, *Passive states and KMS states for general quantum systems*, *Communications in Mathematical Physics* **58**, 273 (1978) (cit. on pp. 67, 69).

[RAM28] C. V. RAMAN and K. S. KRISHNAN, *The Negative Absorption of Radiation*, *Nature* **122**, 12 (1928) (cit. on p. 9).

[Rau07] R. Raussendorf and J. Harrington, *Fault-tolerant quantum computation with high threshold in two dimensions*, *Physical Review Letters* **98**, 190504 (2007) (cit. on pp. 2, 37).

[Res] S. Resch and U. R. Karpuzcu, *Benchmarking Quantum Computers and the Impact of Quantum Noise* (cit. on p. 3).

[ROO04] C. F. ROOS, G. P. T. Lancaster, M. RIEBE, H. Häffner, W. Hänsel, S. Gulde, C. Becher, J. Eschner, F. Schmidt-Kaler, and R. Blatt, *Bell states of atoms with ultralong lifetimes and their tomographic state analysis*, *Physical Review Letters* **92**, 220402 (2004) (cit. on pp. 5, 31).

[Roo08a] C. F. Roos, *Ion trap quantum gates with amplitude-modulated laser beams*, *New Journal of Physics* **10**, 013002 (2008) (cit. on pp. 20, 21).

[ROO08b] C. F. ROOS, M. CHWALLA, T. MONZ, P. SCHINDLER, K. KIM, M. RIEBE, and R. Blatt, *Quantum Information Processing and Ramsey Spectroscopy with Trapped Ions*, in: L. Hollberg, J. C. Bergquist, and M. A. Kasevich (Eds.), *ICOLS 2007*, 53–62, WORLD SCIENTIFIC, New Jersey and London, 2008 (cit. on pp. 24, 29, 42, 80).

[Roß16] J. Roßnagel, S. T. Dawkins, K. N. Tolazzi, O. Abah, E. Lutz, F. Schmidt-Kaler, and K. Singer, *A single-atom heat engine*, Science **352**, 325 (2016) (cit. on p. 4).

[Rov21] C. Rovelli, *Helgoland: Making sense of the quantum revolution*, Riverhead Books, New York, 2021, first u.s. hardcover ed. (cit. on p. 2).

[Rus14] T. Ruster, C. Warschburger, H. Kaufmann, C. T. Schmiegelow, A. Walther, M. Hettrich, A. Pfister, V. Kaushal, F. Schmidt-Kaler, and U. G. Poschinger, *Experimental realization of fast ion separation in segmented Paul traps*, Physical Review A **90** (2014) (cit. on p. 44).

[Rus16] T. Ruster, C. T. Schmiegelow, H. Kaufmann, C. Warschburger, F. Schmidt-Kaler, and U. G. Poschinger, *A long-lived Zeeman trapped-ion qubit*, Applied Physics B **122** (2016) (cit. on pp. 29, 47).

[Rus17a] T. Ruster, *Entanglement-based magnetometry in a scalable ion-trap quantum processor*, Phd, University of Mainz (2017) (cit. on pp. 14, 39, 47, 48, 56, 57, 59, 60).

[Rus17b] T. Ruster, H. Kaufmann, M. A. Luda, V. Kaushal, C. T. Schmiegelow, F. Schmidt-Kaler, and U. G. Poschinger, *Entanglement-Based dc Magnetometry with Separated Ions*, Physical Review X **7** (2017) (cit. on pp. 47, 48, 50).

[Šaš03] M. Šašura and A. M. Steane, *Fast quantum logic by selective displacement of hot trapped ions*, Physical Review A **67** (2003) (cit. on p. 20).

[Sch00] D. V. Schroeder, *An introduction to thermal physics*, Addison Wesley Longman, San Francisco and Harlow, 2000 (cit. on p. 66).

[Sch06] S. Schulz, U. Poschinger, K. Singer, and F. Schmidt-Kaler, *Optimization of segmented linear Paul traps and transport of stored particles*, Fortschritte der Physik **54**, 648 (2006) (cit. on p. 10).

[Sch16a] W. P. Schleich, K. S. Ranade, C. Anton, M. Arndt, M. Aspelmeyer, M. Bayer, G. Berg, T. Calarco, H. Fuchs, E. Giacobino, M. Grassl, P. Hänggi, W. M. Heckl, I.-V. Hertel, S. Huelga, F. Jelezko, B. Keimer, J. P. Kotthaus, G. Leuchs, N. Lütkenhaus, U. Maurer, T. Pfau, M. B. Plenio, E. M. Rasel, O. Renn, C. Silberhorn, J. Schiedmayer, D. Schmitt-Landsiedel, K. Schönhammer, A. Ustinov, P. Walther, H. Weinfurter, E. Welzl, R. Wiesendanger, S. Wolf, A. Zeilinger, and P. Zoller, *Quantum technology: from research to application*, Applied Physics B **122** (2016) (cit. on pp. 1, 2).

[Sch16b] C. T. Schmiegelow, H. Kaufmann, T. Ruster, J. Schulz, V. Kaushal, M. Hettrich, F. Schmidt-Kaler, and U. G. Poschinger, *Phase-Stable Free-Space Optical Lattices for Trapped Ions*, Physical Review Letters **116**, 033002 (2016) (cit. on p. 94).

[Sho94] P. W. Shor, *Algorithms for quantum computation: discrete logarithms and factoring*, in: S. Goldwasser (Ed.), *Foundations of computer science*, 124–134, IEEE Press, Piscataway, 1994 (cit. on p. 1).

[Sho95] Shor, *Scheme for reducing decoherence in quantum computer memory*, Physical Review A **52**, R2493 (1995) (cit. on p. 2).

[Sho00] P. W. Shor (Ed.), *Introduction to Quantum Algorithms*, 2000 (cit. on p. 1).

[SK00] F. Schmidt-Kaler, *Experimente zur Quanten-Informationsverarbeitung*, Habilitation, University of Innsbruck (2000) (cit. on p. 1).

[Sko21] U. Skosana and M. Tame, *Demonstration of Shor's factoring algorithm for N Formula: see text 21 on IBM quantum processors*, Scientific reports **11**, 16599 (2021) (cit. on p. 2).

[Sol21] A. Solfanelli, A. Santini, and M. Campisi, *Experimental Verification of Fluctuation Relations with a Quantum Computer*, PRX Quantum **2** (2021) (cit. on p. 4).

[Sør00] A. Sørensen and K. Mølmer, *Entanglement and quantum computation with ions in thermal motion*, Physical Review A **62** (2000) (cit. on p. 20).

[Spe07] T. Speck and U. Seifert, *The Jarzynski relation, fluctuation theorems, and stochastic thermodynamics for non-Markovian processes*, Journal of Statistical Mechanics: Theory and Experiment **2007**, L09002 (2007) (cit. on p. 4).

[Ste86] S. Stenholm, *The semiclassical theory of laser cooling*, Reviews of Modern Physics **58**, 699 (1986) (cit. on p. 13).

[Ste96] A. M. Steane, *Multiple-particle interference and quantum error correction*, Proceedings of the Royal Society of London. A. Mathematical and Physical Sciences **452**, 2551 (1996) (cit. on p. 2).

[Str21] P. Strasberg, M. G. Díaz, and A. Riera-Campeny, *Clausius inequality for finite baths reveals universal efficiency improvements*, Physical review. E **104**, L022103 (2021) (cit. on pp. 4, 66).

[Til] J. Tilly, H. Chen, S. Cao, D. Picozzi, K. Setia, Y. Li, E. Grant, L. Wossnig, I. Rungger, G. H. Booth, and J. Tennyson, *The Variational Quantum Eigensolver: a review of methods and best practices* (cit. on p. 2).

[Uzd] R. Uzdin, *Methods for measuring noise, purity changes, and entanglement entropy in quantum devices and systems* (cit. on p. 93).

[Uzd18a] R. Uzdin, *The Second Law and Beyond in Microscopic Quantum Setups*, in: F. Binder, L. A. e. Correa, C. Gogolin, J. Anders, and G. Adesso (Eds.), *Thermodynamics in the quantum regime*, vol. 195 of *Fundamental Theories of Physics*, 681–712, Springer, Cham, Switzerland, 2018 (cit. on pp. 4, 66).

[Uzd18b] R. Uzdin and S. Rahav, *Global passivity in microscopic thermodynamics*, Physical Review X **8** (2018) (cit. on pp. 4, 65, 66, 69, 70, 92).

[Uzd20] R. Uzdin, *Thermodynamic approaches to diagnostics* (23-27 November 2020) (cit. on p. 94).

[Uzd21] R. Uzdin and S. Rahav, *Passivity Deformation Approach for the Thermodynamics of Isolated Quantum Setups*, PRX Quantum **2** (2021) (cit. on pp. 4, 65, 92).

[VA18] S. E. Venegas-Andraca, W. Cruz-Santos, C. McGeoch, and M. Lanzagorta, *A cross-disciplinary introduction to quantum annealing-based algorithms*, Contemporary Physics **59**, 174 (2018) (cit. on p. 2).

[van08] M. den van Nest, *Classical simulation of quantum computation, the Gottesman-Knill theorem, and slightly beyond*, arXiv (2008) (cit. on p. 33).

[van20] N. van Horne, D. Yum, T. Dutta, P. Hänggi, J. Gong, D. Poletti, and M. Mukherjee, *Single-atom energy-conversion device with a quantum load*, npj Quantum Information **6** (2020) (cit. on p. 4).

[Vog89] Vogel and Risken, *Determination of quasiprobability distributions in terms of probability distributions for the rotated quadrature phase*, Physical review. A, General physics **40**, 2847 (1989) (cit. on pp. 5, 31).

[Wal12] A. Walther, F. Ziesel, T. Ruster, S. T. Dawkins, K. Ott, M. Hettrich, K. Singer, F. Schmidt-Kaler, and U. Poschinger, *Controlling fast transport of cold trapped ions*, Physical Review Letters **109**, 080501 (2012) (cit. on p. 44).

[War13] U. Warring, C. Ospelkaus, Y. Colombe, R. Jördens, D. Leibfried, and D. J. Wineland, *Individual-ion addressing with microwave field gradients*, Physical Review Letters **110**, 173002 (2013) (cit. on p. 8).

[War15] C. Warschburger, *Aufbau und Charakterisierung einer magnetisch abgeschirmten segmentierten Mikroionenfalle mit langer Qubit-Kohärenzzeit*, Phd, University of Mainz (2015) (cit. on pp. 47, 48, 51).

[Wei76] R. Weinstock, *On a fallacious proof of Earnshaw's theorem*, American Journal of Physics **44**, 392 (1976) (cit. on p. 10).

[Wei04] Y. S. Weinstein, T. F. Havel, J. Emerson, N. Boulant, M. Saraceno, S. Lloyd, and D. G. Cory, *Quantum process tomography of the quantum Fourier transform*, The Journal of Chemical Physics **121**, 6117 (2004) (cit. on p. 31).

[Win79] D. J. Wineland and W. M. Itano, *Laser cooling of atoms*, Physical review. A, General physics **20**, 1521 (1979) (cit. on p. 15).

[Win98] D. J. Wineland, C. Monroe, W. M. Itano, D. Leibfried, B. E. King, and D. M. Meekhof, *Experimental Issues in Coherent Quantum-State Manipulation of Trapped Atomic Ions*, Journal of research of the National Institute of Standards and Technology **103**, 259 (1998) (cit. on pp. 23, 27).

List of Publications

- **Detecting Heat Leaks with Trapped Ion Qubits**

D. Pijn, O. Onishchenko, J. Hilder, U. Poschinger, F. Schmidt-Kaler, R. Uzdin,
Phys. Rev. Lett. **128**, 110601 (2022)

- **Fault-Tolerant Parity Readout on a Shuttling-Based Trapped-Ion Quantum Computer**

J. Hilder, D. Pijn, O. Onishchenko, A. Stahl, M. Orth, B. Lekitsch, A. Rodriguez-Blanco, M. Müller, F. Schmidt-Kaler, U. Poschinger,
Phys. Rev. X **12**, 011032 (2022)

- **Shuttling-Based Trapped-Ion Quantum Information Processing**

V. Kaushal, B. Lekitsch, A. Stahl, J. Hilder, D. Pijn, C. Schmiegelow, A. Bermudez,
M. Müller, F. Schmidt-Kaler, U. Poschinger,
AVS Quantum Sci. **2**, 014101 (2020)

- **Magnetic-film atom chip with 10 μm period lattices of microtraps for quantum information science with Rydberg atoms**

V.Y.F. Leung, D.R.M. Pijn, H. Schlatter, L. Torralbo-Campo, A.L. La Rooij,
G.B. Mulder, J. Naber, M.L. Soudijn, A. Tauschinsky, C. Abarbanel, B. Hadad,
E. Golan, R. Folman, and R.J.C. Spreeuw,
Review of Scientific Instruments **85**, 053102 (2014)

Daniël R.M. Pijn

Curriculum Vitae

Personal Information

Date of birth 15.08.1988

Place of birth Amsterdam

Nationality Dutch

Marital status Single

Education

2016-present **Ph.D. in Physics**, *Johannes Gutenberg Universität, Mainz*

2011-2014 **Master of Science**, *University of Amsterdam*

Advanced Matter and Energy Physics

2007-2010 **Bachelor of Science**, *University of Amsterdam*

Physics and Astronomy

Master thesis

Title *Loading a 2D Microtrap Lattice on a Magnetic Atom Chip*

Supervisors Dr. R.J.C. Spreeuw and Dr. K. Dohmalová

Bachelor thesis

Title *Quantum Gate Fidelities in Atomic Ensembles*

Supervisors Dr. R.J.C. Spreeuw and Prof. Dr. H.B. van Linden van den Heuvell